UNIVERSIDADE ESTADUAL DE CAMPINAS
Faculdade de Engenharia Mecânica

ISABELLA CAROLINE PEREIRA RODRIGUES

Desenvolvimento de *scaffold*s farmacológicos e osteocondutivos processados por manufatura aditiva e rotofiação

CAMPINAS
2024

ISABELLA CAROLINE PEREIRA RODRIGUES

Desenvolvimento de *scaffold*s farmacológicos e osteocondutivos processados por manufatura aditiva e rotofiação

Tese apresentada à Faculdade de Engenharia Mecânica da Universidade Estadual de Campinas como parte dos requisitos exigidos para obtenção do título de Doutora em Engenharia Mecânica, na Área de Materiais e Processos de Fabricação.

Orientador: Prof. Dr. Éder Sócrates Najar Lopes
Coorientador: Profa. Dra. Laís Pellizzer Gabriel

ESTE TRABALHO CORRESPONDE À VERSÃO FINAL DA TESE DEFENDIDA PELA ALUNA ISABELLA CAROLINE PEREIRA RODRIGUES, E ORIENTADA PELO PROF. DR. ÉDER SÓCRATES NAJAR LOPES

CAMPINAS
2024

Ficha catalográfica
Universidade Estadual de Campinas
Biblioteca da Área de Engenharia e Arquitetura
Rose Meire da Silva - CRB 8/5974

R618r

Rodrigues, Isabella Caroline Pereira, 1995-
Desenvolvimento de scaffolds farmacológicos e osteocondutivos processados por manufatura aditiva e rotofiação / Isabella Caroline Pereira Rodrigues. – Campinas, SP : [s.n.], 2024.

Orientador: Éder Sócrates Najar Lopes.
Coorientador: Laís Pellizzer Gabriel.
Tese (doutorado) – Universidade Estadual de Campinas, Faculdade de Engenharia Mecânica.

1. Antibióticos. 2. Engenharia Tecidual. 3. Liberação controlada de fármacos. 4. Impressão tridimensional. 5. Membranas poliméricas. I. Lopes, Éder Sócrates Najar, 1982-. II. Gabriel, Laís Pellizzer, 1987-. III. Universidade Estadual de Campinas. Faculdade de Engenharia Mecânica. IV. Título.

Informações Complementares

Título em outro idioma: Development of pharmacological and osteoconductive scaffolds processed by additive manufacturing and rotary jet spinning
Palavras-chave em inglês:
Antibiotics
Regenerative Medicine/Tissue Engineering
Drugs - Controlled release
Three-dimensional printing
Membranes (Technology) - Materials
Área de concentração: Materiais e Processos de Fabricação
Titulação: Doutora em Engenharia Mecânica
Banca examinadora:
Éder Sócrates Najar Lopes [Orientador]
Amedea Barozzi Seabra
Anderson de Oliveira Lobo
Cecília Amélia de Carvalho Zavaglia
Marcos Akira D'Avila
Data de defesa: 08-03-2024
Programa de Pós-Graduação: Engenharia Mecânica

Identificação e informações acadêmicas do(a) aluno(a)
- ORCID do autor: https://orcid.org/0000-0003-3674-2387
- Currículo Lattes do autor: http://lattes.cnpq.br/4678021702773064

UNIVERSIDADE ESTADUAL DE CAMPINAS
FACULDADE DE ENGENHARIA MECÂNICA

TESE DE DOUTORADO ACADÊMICO

Desenvolvimento de *scaffold*s farmacológicos e osteocondutivos processados por manufatura aditiva e rotofiação

Autor: Isabella Caroline Pereira Rodrigues

Orientador: Prof. Dr. Éder Sócrates Najar Lopes
Coorientador: Profa. Dra. Laís Pellizzer Gabriel

A Banca Examinadora composta pelos membros abaixo aprovou esta Tese:

Prof. Dr. Éder Sócrates Najar Lopes (Presidente)
Faculdade de Engenharia Mecânica/ Universidade Estadual de Campinas

Profa. Dra. Amedea Barozzi Seabra
Centro de Ciências Naturais e Humanas/ Universidade Federal do ABC

Prof. Dr. Anderson De Oliveira Lobo
Campus Universitário Ministro Petrônio Portella/ Universidade Federal do Piauí

Profa. Dra. Cecília Amélia de Carvalho Zavaglia
Faculdade de Engenharia Mecânica/ Universidade Estadual de Campinas

Prof. Dr. Marcos Akira D'Avila
Faculdade de Engenharia Mecânica/ Universidade Estadual de Campinas

A Ata de Qualificação com as respectivas assinaturas dos membros encontra-se no SIGA/Sistema de Fluxo de Tese e na Secretaria do Programa da Unidade.

Campinas, 08 de março de 2024.

Dedicatória

Dedico essa tese de doutorado à minha família que sempre acreditou nos meus sonhos, celebrou minhas conquistas e me apoiou nos momentos difíceis.

Agradecimentos

Ao longo deste trabalho, diversas pessoas, instituições e agências de fomento ofereceram apoio. Por isso, gostaria de agradecer:

À Deus, por ser minha luz e força, por me guiar para que eu possa trazer um pouco de Sua luz comigo.

Aos meus pais, Vinícius e Débora, que me ensinaram a lutar com ética e garra, a sempre buscar ser uma melhor versão de mim e que acolheram meus sonhos e angústias.

Aos meus irmãos, Guilherme e Alexandre, por todo carinho, alegria e parceria de sempre.

Ao meu noivo, Alessandro Bigoni, pelo amor, companherismo e apoio. Pelas discussões sobre o mundo, por acreditar em mim e me fazer querer ser melhor na vida e na ciência.

Ao Prof. Éder Lopes e à Profa. Laís Gabriel pela orientação, confiança e por desde o início acreditarem no meu potencial, me dando as ferramentas e apoio necessário para que eu pudesse me desenvolver como pesquisadora e profissional.

Aos meus tios, Alessandra e Rodrigo, que foram exemplos e muito importantes ao longo da minha trajetória na pesquisa e como pessoa.

À outras pessoas tão queridas da minha família, como minhas avós Luzia e Jamila, meus tios, entre eles Cynthia e Mikio e primos, por todo carinho.

Aos meus grandes amigos, entre eles Anne, Renan e Karina, que ouviram meus desabafos, celebraram comigo e sempre se fizeram tão presentes, independentemente da distância.

Aos amigos e grandes pesquisadores que a Fulbright me permitiu conhecer, Bárbara, Victor, André e família, James, Nathália e família, Jéssica entre outros que tornaram esse período ainda mais enriquecedor.

Aos meus colegas e amigos pesquisadores da UNICAMP, Karina Voigt, Camila Sartori, Mônica Granusso, Ingrid Casalle, Gustavo Granjeia, Mateus Franco, Mateus Pozzibon, Guilherme Queiroz, Jéssica Ferreira, Bruno, Eduardo Fonseca, André Gabriel e Prof. Augusto Luchessi, por todo conhecimento compartilhado, ajuda nos experimentos, discussões e artigos desenvolvidos ao longo desse período.

Aos professores e amigos que me inspiraram e apoiaram nessa profissão, Marcelo Matsudo, Guilherme Rodriguez, Juliana Fedoce, Susan Duarte, Dirceu da Silva e tantos outros.

Aos meus alunos e orientados, pela confiança e oportunidade de aprender e ensinar.

A Fulbright pela oportunidade de expandir meus horizontes, me conectar e trazer mais conhecimento para o meu país.

To my advisor at Harvard Medical School, Prof. Yu Shrike Zhang, for welcoming me into his lab, making sure that I had what I needed for the projects, and for all the guidance.

To my colleagues at Shrike's lab, Camila, Thiago, Luis Orrantia, Xiao, Luis Ferreira, Sushila, Liam, Carlos, Federico, Sonia, and Regina, among others, who are so amazing and humble, and taught me so much about bioprinting, cells, and science.

To the friends who made me feel at home while I was in a different country, Annie, Katie, and Elyse, and for our scientific discussions with a lot of tea.

To the kind hearts I met all over the world during this journey, Monika, Mikayla, Alex, Don, Mel, and Raffi, and so many others that I was lucky enough to cross paths with.

Pesquisa apoiada pelos Laboratórios Abertos do Centro de Tecnologia da Informação Renato Archer (CTI), Unidade de Pesquisa do MCTI, pelo Laboratório Central de Tecnologias de Alto Desempenho (LaCTAD - UNICAMP), Instituto Nacional de Fotônica Aplicada à Biologia Celular (INFABIC- UNICAMP), Centro Pluridisciplinar de Pesquisas Químicas, Biológicas e Agrícolas (CPQBA – UNICAMP) e Laboratório de Biotecnologia InPhyto.

Também gostaria de agradecer a Dra. Fabiana Garboggini e Dra. Marta Duarte da Divisão de Recursos Microbianos (DRM – CPQBA) por disponibilizarem a infraestrutura e bactérias necessárias para o estudo.

Ao Sr. Luis e Márcia Taipina por todo apoio na realização das atividades de pesquisa.

Aos pesquisadores do CTI que apoiaram esse trabalho, Michele Odnicki, Laureana Fontolan, Pedro Noritomi e Marcelo Oliveira.

O presente trabalho foi realizado com apoio da Fundação de Amparo à Pesquisa do Estado de São Paulo (FAPESP), processo #2020/14679-9, do Conselho Nacional de Desenvolvimento Científico e Tecnológico (CNPq), processo #140997/2020-2 e da Fulbright Brasil.

Resumo

As cirurgias no sistema musculoesquelético têm um impacto significativo no sistema de saúde, exigindo frequentemente o uso de implantes para reabilitação. Entretanto os implantes utilizados atualmente apresentam limitações que podem levar a baixa osseointegração e contaminação, conhecida como osteomielite. Implantes combinados com scaffolds farmacológicos e osteocondutivos surgem como alternativas promissoras para minimizar as falhas dos implantes existentes. O uso de ligas de titânio, como Ti6Al4V, é comum em implantes devido à sua resistência mecânica, mas modificações estruturais são necessárias para reduzir sua rigidez e evitar a reabsorção óssea. Aditivos, como hidroxiapatita (HA) e colágeno (COL), podem ser utilizados para melhorar a osteocondução e consequente osseointegração, e antibióticos, como a rifampicina (RIF), para prevenir a osteomielite. O polímero biorreabsorvível poli (ácido lático-co-ácido glicólico) (PLGA) é amplamente utilizado como matriz para aditivos e fármacos para produção de scaffolds. As técnicas de manufatura aditiva, incluindo fusão em leito de pó e (bio)impressão 3D, tem grande potencial na produção de implantes e scaffolds, permitindo customização e adequando suas propriedades mecânicas e estruturais. A rotofiação também é uma técnica promissora e permite a produção de scaffolds poliméricos fibrosas que mimetizam a matriz extracelular. Este estudo demonstra o potencial da combinação dessas técnicas e materiais para promover a osseointegração e a atividade antibacteriana, apresentando novos scaffolds e implantes com grande aplicabilidade na regeneração óssea. Para isso, scaffolds e implantes compósitos baseados em PLGA-HA, PLGA-COL-HA, PLGA-HA-RIF e Ti6Al4V foram desenvolvidos e caracterizados. Os implantes produzidos por meio de manufatura aditiva e os scaffolds fabricados por rotofiação apresentaram características desejáveis, como estabilidade dos materiais envolvidos, morfologia homogênea, distribuição uniforme de aditivos, propriedade osteocondutiva, liberação controlada de antibiótico e biocompatibilidade. Além disso, os scaffolds produzidos por (bio)impressão 3D utilizando coextrusão multimaterial demonstraram propriedades mecânicas aprimoradas comparada a outros materiais (bio)impressos e capacidade de promover a viabilidade, proliferação e diferenciação de células-tronco mesenquimais para facilitar a regeneração óssea. Esses resultados oferecem uma visão otimista para o futuro do tratamento de lesões no aparelho locomotor, indicando que os implantes desenvolvidos neste estudo têm o potencial de superar as limitações dos implantes atuais, melhorando assim os resultados clínicos e a qualidade de vida dos pacientes. No entanto, é importante ressaltar a necessidade de estudos

adicionais para otimizar as condições de processamento e validar a eficácia da regeneração óssea in vivo, garantindo assim a tradução bem-sucedida desses avanços para a prática clínica. Com isso, este trabalho contribui significativamente para o avanço da engenharia de tecidos ósseos e oferece uma base sólida para pesquisas futuras nessa área crucial da medicina regenerativa.

Palavras Chave: Antibiótico; Engenharia Tecidual; Impressão tridimensional; Liberação controlada de fármacos; Membranas Poliméricas.

Abstract

Skeletal system surgeries have a significant impact on the healthcare system in Brazil and globally. Orthopedic implants are usually essential for patient rehabilitation. However, current implants have limitations that can lead to low osseointegration and contamination, known as osteomyelitis. Implants combined with pharmacological and osteoconductive scaffolds emerge as promising alternatives to minimize the failures of existing implants. The use of titanium alloys, such as Ti6Al4V, is common in implants due to their mechanical strength, but structural modifications are necessary to reduce their stiffness and avoid bone resorption. Additives, such as hydroxyapatite (HA) and collagen (COL), can be used to improve osteoconduction and subsequent osseointegration, and antibiotics, such as rifampicin (RIF), to prevent osteomyelitis. The biodegradable polymer poly(lactic-co-glycolic acid) (PLGA) is widely used as a matrix for additives and drugs for scaffold production. Additive manufacturing techniques, including powder bed fusion and 3D (bio)printing, have great potential in producing implants and scaffolds, allowing customization and tailoring of their mechanical and structural properties. Rotary jet spinning is also a promising technique and enables the production of fibrous polymeric scaffolds that mimic the extracellular matrix. This study demonstrates the potential of combining these techniques and materials to promote osseointegration and antibacterial activity, presenting new scaffolds and implants with great applicability in bone regeneration. For this purpose, composite scaffolds and implants based on PLGA-HA, PLGA-COL-HA, PLGA-HA-RIF, and Ti6Al4V were developed and characterized. Implants produced through additive manufacturing and scaffolds manufactured by rotary jet spinning showed desirable characteristics, such as stability of the involved materials, homogeneous morphology, uniform distribution of additives, osteoconductive property, controlled antibiotic release, and biocompatibility. Furthermore, scaffolds produced by 3D (bio)printing using multimaterial coextrusion demonstrated enhanced mechanical properties compared to other (bio)printed materials and the ability to promote the viability, proliferation, and differentiation of mesenchymal stem cells to facilitate bone regeneration. These results offer an optimistic view for the future of locomotor system injury treatment, indicating that the implants developed in this study have the potential to overcome the limitations of current implants, thus improving clinical outcomes and patients' quality of life. However, it is important to emphasize the need for additional studies to optimize processing conditions and validate the effectiveness of in vivo bone regeneration, thus ensuring the successful translation of these advancements into clinical

practice. Therefore, this work significantly contributes to advancing bone tissue engineering and provides a solid foundation for future research in this crucial area of regenerative medicine.

Keywords: Antibiotics; Controlled Release; Membranes; Three-dimensional printing; Tissue Engineering.

Sumário

1 INTRODUÇÃO 13
2 OBJETIVOS 15
3 REVISÃO DA LITERATURA 16
3.1 Ossos e Implantes: Entre solucionar e aumentar o problema 16
3.2 Propriedades Necessárias aos Novos Implantes 18
3.3 Materiais e Processos de Fabricação dos Implantes 20
4 ANÁLISE BIBLIOMÉTRICA 31
5 ANÁLISE EXPERIMENTAL 33
5.1. Preparo e Análise de Viscosidade da solução polimérica e Rotofiação dos *scaffolds* 33
5.2. Preparo das tintas e biotintas e (bio)impressão 33
5.3. Caracterização reológica das tintas e biotinta 34
5.4. Modelagem e fabricação das estruturas metálicas 34
5.5. Caracterização de propriedades morfológicas, químicas, térmicas e estruturais 35
5.6. Avaliação da hidrofilicidade e degradação *in vitro* 36
5.7. Avaliação da eficiência de encapsulamento e liberação de fármaco do *scaffold* 37
5.8. Ensaios de atividade antibacteriana 37
5.9. Ensaios Mecânicos de Compressão 37
5.10 Ensaio de osteocondução 38
5.11. Análise de viabilidade, proliferação, morfologia e diferenciação celular 39
5.12. Análise Estatística 41
6 RESULTADOS: ARTIGOS PUBLICADOS E SUBMETIDOS 42
6.1. Manuscrito do Artigo 1 44
6.2. Manuscrito do Artigo 2 60
6.3. Manuscrito do Artigo 3 81
7 DISCUSSÃO 110
8 CONCLUSÕES 114
9 SUGESTÕES DE TRABALHOS FUTUROS 115
REFERÊNCIAS 116
APÊNDICE A 133
APÊNDICE B 135

1 INTRODUÇÃO

Lesões no aparelho locomotor são comuns e normalmente provêm de acidentes de alto impacto ou doenças, incluindo danos no joelho, quadril e coluna vertebral. Doenças na coluna, por exemplo, têm afetado mais pessoas ao longo dos anos, comprometendo a qualidade de vida dos pacientes e podendo levar à incapacitação (FATOYE; GEBRYE; ODEYEMI, 2019). Implantes como próteses e enxertos ósseos são necessários em casos de lesões e outras doenças relacionadas aos ossos, como tumores, osteoartrite e osteoporose. Nos últimos cinco anos (2019-2023), mais de 1,5 milhão de próteses, órteses e outros materiais especiais relacionados ao ato cirúrgico, com um valor equivalente a mais de 900 milhões de reais, foram aprovados para utilização pelo Sistema Único de Saúde no Brasil (DATASUS, 2023).

O desenvolvimento de implantes inovadores para aumentar a qualidade de vida e sobrevida de pessoas sujeitas a utilização desses materiais é fundamental. Técnicas de engenharia de tecidos são promissoras para o desenvolvimento de implantes, uma vez que focam na substituição, regeneração ou manutenção de tecidos ou órgãos danificados (LANGER; VACANTI, 1993). Os implantes desenvolvidos por essas técnicas, conhecidos como *scaffolds,* são estruturas temporárias (biorreabsorvíveis) e porosas que podem conter células, fatores de crescimento ou outros aditivos. Diferentes técnicas de fabricação e materiais metálicos, poliméricos e cerâmicos são utilizados na produção de implantes e *scaffolds* para aplicações ósseas, trazendo distintas funcionalidades. Entretanto, a alta quantidade de cirurgias de revisão necessária para substituição do implante revela que ainda há muito a ser desenvolvido para a obtenção de um implante adequado.

A necessidade de cirurgias de revisão está principalmente relacionada à falta de osseointegração e compatibilidade mecânica (ZHANG; CHEN, 2019), e à ocorrência de osteomielite (KURTZ et al., 2008) nos implantes ósseos. Portanto, o desenvolvimento de novos implantes ósseos que forneçam a resistência mecânica necessária, promovam a osteocondução ideal e previnam infecções locais por microrganismos é uma alternativa promissora para mitigar o impacto na saúde e na economia das falhas de implantes atuais. Entretanto, apesar do foco de alguns estudos nesta temática (JAHANMARD et al., 2020; RYU et al., 2019), ainda há muito a ser explorado em técnicas de processamento, combinação de materiais e análises para um implante ou *scaffold* ideal.

Esta tese aborda esses desafios por meio de três projetos inovadores (**Figura 1**). O primeiro projeto envolveu a produção e caracterização de membranas osteocondutivas de poli (ácido lático-co-ácido glicólico) (PLGA) contendo nanopartículas bioativas de hidroxiapatita (HA) pelo potente método de rotofiação. Este projeto apresenta uma combinação inédita de técnica e materiais, resultando na fabricação eficiente de membranas fibrosas que promovem osteocondução. Os outros dois projetos da tese se destacam por sua abordagem multifuncional, expandindo o campo da osseointegração. O segundo projeto visou o desenvolvimento de implantes compósitos inovadores que oferecessem não apenas compatibilidade mecânica com o tecido ósseo, através da modelagem de estruturas porosas e complexas de Ti6Al4V por manufatura aditiva, mas também osseointegração superior e prevenção local de infecções bacterianas, através de membranas osteocondutivas rotofiadas com rifampicina.

Por fim, o terceiro projeto aborda a fabricação de *scaffolds* compósitos (bio)impressos com HA para regeneração óssea. Esses *scaffolds* foram projetados para serem capazes de suportar o crescimento, proliferação e diferenciação de células-tronco mesenquimais (MSCs), oferecendo um ambiente favorável para a osseointegração eficiente e duradoura. Com essa abordagem integrada e multifacetada, esta tese não só contribui para o avanço tecnológico na área de implantes, *scaffolds* e osseointegração, mas também propõe soluções práticas para os desafios clínicos existentes.

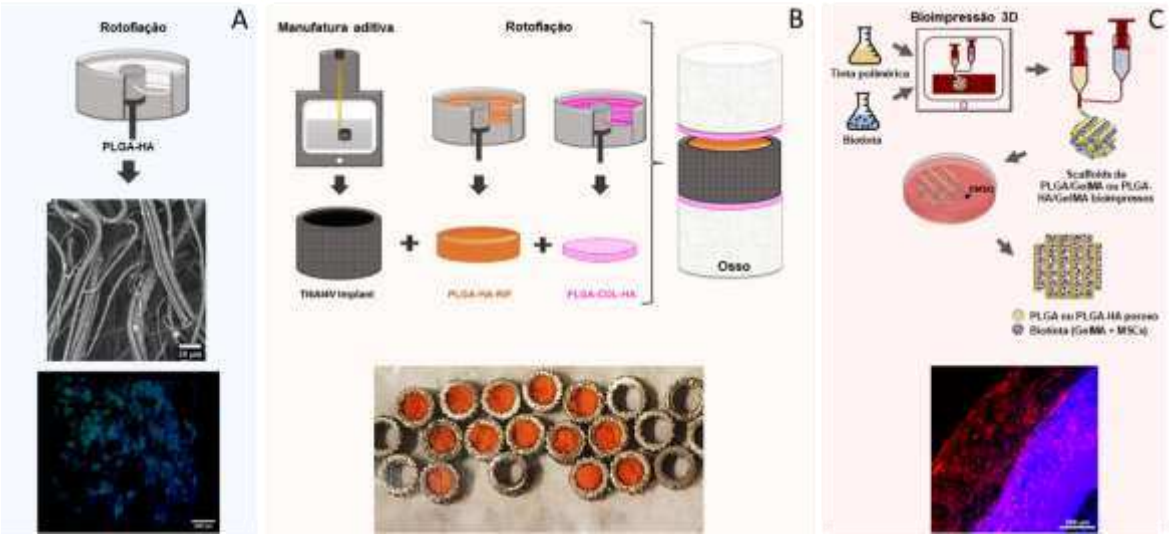

Figura 1. Projetos desenvolvidos na tese. A) Produção e caracterização de membranas osteocondutivas produzidas por rotofiação. B) Desenvolvimento de novos implantes que permitam osseointegração, compatibilidade mecânica e prevenção local de bactérias; C) Fabricação de scaffolds compósitos (bio)impressos para regeneração óssea, com capacidade de suportar o crescimento, proliferação e diferenciação de MSCs.

2 OBJETIVOS

Este estudo visa a produção de novos implantes, baseados em manufatura aditiva, (bio)impressão 3D e membranas fibrosas produzidas por rotofiação de forma a obter *scaffold*s ósseos com propriedades de osteocondução e prevenção local de infecção bacteriana, para aplicações ósseas. Os objetivos específicos deste estudo são:

- Desenvolver a solução polimérica com a concentração necessária para a rotofiação dos *scaffolds* contendo nanopartículas*;*
- Definir os parâmetros de processo da rotofiação para obtenção dos scaffolds;
- Avaliar se os *scaffolds* contêm os diferentes polímeros e aditivos adicionados;
- Projetar e definir os parâmetros para produção da estrutura porosa de Ti6Al4V por MA/EBM com diferentes tamanhos de poros;
- Avaliar se os *scaffolds* e implantes apresentam bioatividade relacionada a osteocondução, biocompatibilidade, adesão e proliferação celular e atividade antibacteriana;
- Analisar as propriedades estruturais, mecânicas e morfológicas da estrutura de Ti6Al4V para avaliar sua aplicação óssea;
- Desenvolver uma técnica que permita a (bio)impressão 3D de biotinta contendo células-tronco mesenquimais (MSCs) co-extrudada simultaneamente com polímero contendo nanopartículas;
- Avaliar as propriedades microestruturais e mecânicas dos *scaffolds* bioimpressos para garantir funcionalidade em aplicações ósseas;
- Analisar a atividade celular de MSCs no que tange sua viabilidade, proliferação, morfologia e diferenciação para promover mecanismos de osseointegração.

3 REVISÃO DA LITERATURA

3.1 Ossos e Implantes: Entre solucionar e aumentar o problema

Os ossos são órgãos que constituem o sistema esquelético, formados de tecido conjuntivo especializado, com uma matriz composta por elementos inorgânicos (cálcio, magnésio, potássio, fosfatos, entre outros) e orgânicos (como colágenos e glicoproteínas), em uma proporção em massa de 60% e 30%, respectivamente, e o restante equivalente a água (FENG, 2009; WALSH; OHNO; GUZELSU, 1994). As principais células presentes no osso são os osteoblastos, osteócitos e osteoclastos. Os osteoblastos se diferenciam em osteócitos e produzem material orgânico como proteínas da matriz extracelular. Os osteócitos formam o tecido ósseo e os osteoclastos são responsáveis pela absorção e remodelação do osso (AGARWAL; GARCÍA, 2015; REDDI, 1981). O osso é formado por duas estruturas principais, o tecido compacto (ou denso) e o trabeculado (ou esponjoso), que equivalem a 80% e 20% de um osso saudável, respectivamente (JAHAN; TABRIZIAN, 2016). A camada de tecido compacto é externa e de tecido trabeculado é interna ao osso. Além disso, o osso é irrigado por vasos sanguíneos, apresenta uma medula no seu interior, onde podem ser produzidas células-tronco, e possui uma membrana externa chamada periósteo (SAWANT e SHEGOKAR, 2016).

A formação do osso no organismo ocorre principalmente pelos processos de osteogênese e ossificação, que consistem na produção das células e na mineralização do tecido ósseo, respectivamente (JAHAN e TABRIZIAN, 2016). Após sua formação, o osso passa por dois mecanismos principais de desenvolvimento durante toda vida, a modelação e a remodelação óssea (DITTMER e FIRTH, 2017). A modelação óssea está associada ao crescimento e sua função principal é gerar um aumento na massa óssea e alterações no formato do osso. Já a remodelação óssea ocorre ao longo da vida com a função de substituir tecido ósseo antigo ou danificado por um novo tecido ósseo (ALLEN e BURR, 2014). Em ambos os mecanismos, os osteoclastos e osteoblastos são os responsáveis por coordenar a reabsorção e formação do tecido ósseo, respectivamente. Na remodelação óssea, as duas células devem trabalhar em equilíbrio, de forma que o tecido reabsorvido seja totalmente substituído, caso contrário pode levar ao enfraquecimento do osso (STEFFI *et al.*, 2018). Esse enfraquecimento causado pelo desbalanço na reabsorção óssea é o principal causador de doenças como a osteoporose e de falha ou subsidência de implantes. Além de fatores

genéticos e hormonais, sabe-se que estímulo mecânico pode influenciar nesses mecanismos (DITTMER e FIRTH, 2017).

Considerando a estrutura e fisiologia do osso, as primeiras estruturas utilizadas para reabilitar a função óssea em muitos procedimentos cirúrgicos, como fusão intervertebral, foram o próprio osso na forma de enxertos ósseos, principalmente autógenos (do próprio paciente) (JAKOI; IORIO; CAHILL, 2015). Entretanto, esses tipos de enxertos têm limitação de volume a ser doado e envolvem mais de um procedimento cirúrgico e muitas complicações associadas, enquanto enxertos alógenos (de outros doadores) ou xenógenos (de outras espécies) podem causar infecções e respostas imunes (WANG; YEUNG, 2017). Dessa forma, o desenvolvimento de implantes se tornou necessário para superar tais desvantagens.

Entretanto, alguns problemas ósseos relacionados com implantes ainda são muito frequentes como a baixa osseointegração e a infecção. A osseointegração se refere a união eficiente entre o osso e implante e está associada a três mecanismos principais: osteogênese, osteoindução e osteocondução. O mecanismo da osteogênese é a síntese de osso novo por elementos específicos no implante, como células incorporadas ou compostos que estimulam as células hospedeiras a sintetizar osso novo (D'SOUZA et al., 2019). A osteoindução envolve o recrutamento de células-tronco mesenquimais (MSCs) para se diferenciar em outras células ósseas, como os osteoblastos (D'SOUZA et al., 2019). Finalmente, o mecanismo de osteocondução está associado à angiogênese e à condução de células para dentro do implante para o crescimento ósseo (D'SOUZA et al., 2019). A osseointegração insuficiente do implante com o osso é um problema considerável que pode levar à movimentação do implante, falha e necessidade de cirurgias de revisão (**Figura 2**).

As infecções no osso, conhecidas como osteomielite, também são problemas graves e recorrentes nos procedimentos cirúrgicos com implantes (MASTERS et al., 2019). Nos últimos 5 anos (2019-2023), quase 5 mil internações foram registradas por osteomielite, envolvendo um gasto de mais de 6 milhões de reais (DATASUS, 2023). A principal infecção óssea é comumente causada por bactérias do gênero *Staphylococcus* (gram positivas) (MASTERS et al., 2019). Estas bactérias são capazes de se proliferar facilmente na superfície do implante gerando inflamação local. Para a prevenção e tratamento da osteomielite, recorre-se primeiramente à administração de fármacos (antibióticos), como a rifampicina (RIF) e vancomicina (ARAGÓN et al., 2019). Entretanto, como esta administração ocorre principalmente por via oral, a dosagem tende a ser muito alta e com

baixa eficácia (HASAN et al., 2018). Por esse motivo, a remoção do tecido contaminado e as cirurgias de revisão, ou até mesmo a amputação, se tornam muitas vezes necessárias (KURTZ et al., 2008) ou morte do paciente em mais de 5% dos casos (ALBUHAIRN; HIND; HUTCHINSON, 2008). A osteomielite representa, portanto, um grande impacto econômico na saúde, sendo estimado um gasto de 16,2 bilhões de dólares apenas nos Estados Unidos no ano de 2020 (KURTZ et al., 2012).

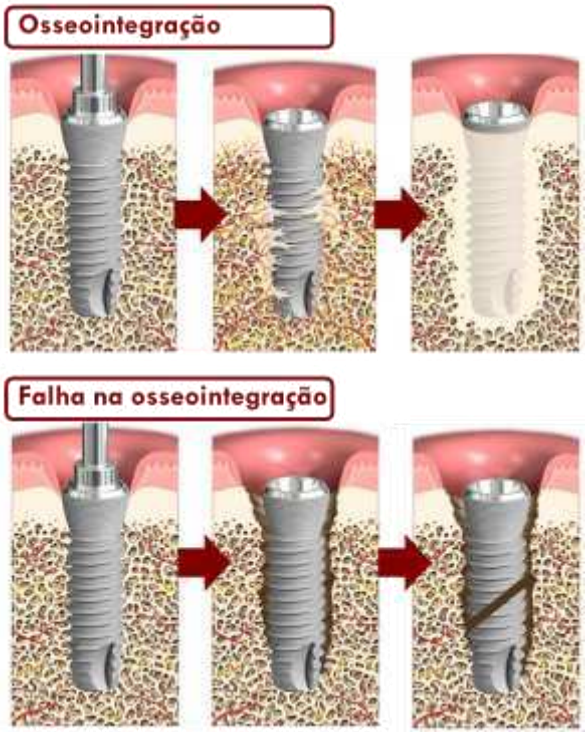

Figura 2. Sucesso e falha na osseointegração.
Fonte: Modificada de ALBREKTSSON et al., 2017

3.2 Propriedades Necessárias aos Novos Implantes

Considerando a estrutura do osso, o funcionamento do tecido ósseo e os principais problemas causados por implantes, é de suma importância que o implantes ósseos sejam desenvolvidos com propriedades melhoradas. As principais propriedades a serem consideradas são: a biocompatibilidade dos materiais e aditivos, as propriedades mecânicas do implante e a bioatividade.

O conceito de biocompatibilidade para implantes ósseos pode ser definido como sua habilidade de interagir adequadamente com o tecido adjacente e o organismo sem causar reação negativa, como resposta inflamatória (CVRČEK; HORÁKOVÁ, 2019). A biocompatibilidade está relacionada com a bioatividade, funcionalidade e estabilidade dos materiais (CVRČEK; HORÁKOVÁ, 2019). Os materiais e aditivos utilizados para o desenvolvimento dos *scaffolds* devem ser biocompatíveis ou, ao menos, bioinertes (que não interagem com o tecido/organismo) para garantir que não haja rejeição do implante (WARBURTON et al., 2020). Ensaios *in vitro* que avaliem a citotoxicidade, *in vivo* para avaliar a interação sistêmica com o organismo e clínicos são necessários para efetivamente avaliar a biocompatibilidade

A influência do estímulo mecânico na adaptação e remodelação óssea foi abordado previamente e é principalmente descrita na Lei de Wolff, na qual correlacionou-se a baixa solicitação mecânica com o aumento na reabsorção do osso (MCNEILL INGHAM et al., 2017). Dessa maneira, sabe-se que implantes precisam resistir ao esforço mecânico exigido a sua aplicação. Por outro lado, propriedades mecânicas, como rigidez do implante, muito superiores às do osso (0,05 a 30 GPa) (WU et al., 2013) podem centralizar o estímulo mecânico, efeito chamado "*stress shielding*", causando a remodelação óssea, que leva à reabsorção, enfraquecimento do osso e consequente falha do implante (MONDAL; GHOSH, 2019). Dependendo do local onde o osso se encontra, possui diferentes estruturas e funções e é sujeito a diferentes estímulos mecânicos. As vértebras da coluna, por exemplo, são formadas por um núcleo maior de osso trabecular com uma "parede" externa mais fina de osso compacto e têm a função de sustentação (RAWLS; FISHER, 2018). Dessa maneira, grande parte dos estudos de propriedades biomecânicas das vértebras, devem considerar a sua estrutura, movimentação e propriedades, como rigidez e resistência mais próximos do osso trabecular, para desenvolver implantes (CESAR et al., 2020). Portanto, características mecânicas de implantes próximas às do osso em que estão sendo aplicados são muito importantes no fornecimento de suporte estrutural e na fisiologia do osso.

Além da biocompatibilidade e características mecânicas, a bioatividade é essencial para implantes. A bioatividade está relacionada com o estímulo de resposta biológica pelo organismo, favorecendo os mecanismos de osseointegração, por exemplo. Portanto, algumas estratégias para aumentar a bioatividade dos implantes são a adição de células, como MSCs, que promovem osteogênese e osteoindução (KURODA et al., 2011) e a adição de materiais inspirados nos componentes orgânicos e inorgânicos dos ossos, normalmente como

recobrimento superficial, para promover a osteocondução (BUSER et al., 2016). A alta porosidade e poros interconectados também são utilizados para facilitar a adesão celular, crescimento ósseo e vascularização através do implante, propiciando o mecanismo osteocondutivo do implante (GHAYOR; WEBER, 2018). Tamanhos de poros também podem afetar a regeneração óssea e estudos mostram que o tamanho de poros ideal para estas aplicações seria com diâmetros entre 200 e 500 μm (PENK et al., 2013; THAVORNYUTIKARN; CHANTARAPANICH; CHEN, 2014).

3.3 Materiais e Processos de Fabricação dos Implantes

Como abordado anteriormente, os implantes apresentam limitações e diversas oportunidades de melhoria em suas propriedades que devem ser exploradas para atingir a regeneração óssea ideal e aumentar a qualidade de vida dos pacientes. Essas melhorias podem ser alcançadas através da utilização de novos materiais e processos de fabricação e/ou modificação.

Polímeros, cerâmicas e metais têm sido usados para criar implantes e *scaffolds* (ABRAHAM; VENKATESAN, 2023). Materiais biorreabsorvíveis em cada grupo se destacam, pois são absorvidos pelo organismo após atenderem às necessidades temporárias da aplicação, prevenindo complicações de longo prazo. Além disso, muitos aditivos e enxertos diferentes podem ser usados com todos os materiais estruturais para melhorar suas propriedades. Neste contexto, os principais materiais e aditivos estudados nos últimos anos serão abordados a seguir.

3.3.1. Metais

Biomateriais metálicos, principalmente de ligas de titânio, cobalto ou aço inoxidável, são os mais utilizados para aplicações com suporte de carga, sendo biocompatíveis e capazes de fornecer resistência mecânica. Ligas de cobalto e aço foram as primeiras a serem utilizadas, entre 1920 e 1940 (GIBON et al., 2017). As ligas de cobalto-cromo são utilizadas em implantes de articulações, sendo bioinertes, resistentes a corrosão e desgaste e apresentando rigidez e alta dureza (GOHARIAN; ABDULLAH, 2017), todavia, têm baixa

osseointegração, quando comparadas às outras ligas (BABIS; MAVROGENIS, 2014) e verificou-se que resíduos do desgaste desses implantes podem levar à inflamação no organismo (SAMELKO et al., 2016).

Já as ligas cirúrgicas de aço inoxidável são muito utilizadas em placas e outros implantes ósseos. O aço inoxidável 316L (ASTM F138) é o mais utilizado para aplicações biomédicas, dentre as ligas de aço, e consiste em uma liga contendo ferro (Fe), cromo (Cr), níquel (Ni), molibdênio (Mo), entre outros metais, com pouca adição de carbono, levando à formação da microestrutura da austenita (DUX, 2019). As ligas austeníticas de aço inoxidável não são magnéticas e apresentam propriedades interessantes como a resistência a corrosão e boa ductilidade (LI et al., 2020a). Todavia, o módulo de Young e a dureza do aço inoxidável 316L são incompatíveis com o osso, podendo gerar fratura, reabsorção óssea e redução na taxa de regeneração (GANESH; RAMAKRISHNA; GHISTA, 2005). Além disso, apesar da resistência dessa liga, alguns processos de corrosão, como corrosão por Pite (punctiforme) e corrosão intersticial, podem ocorrer, levando a falhas na fixação do implante (LI et al., 2020a). A longo prazo verificou-se que ocorre a liberação de íons metálicos, como cromo e níquel, que se acumulam no tecido, podendo ser alergênicos, tóxicos ou carcinogênicos (KANERVA; FÖRSTRÖM, 2001). Algumas alternativas têm sido estudadas para evitar a utilização de níquel como a sua substituição por manganês e por alta concentração de nitrogênio para estabilização da liga austenítica (TALHA; BEHERA; SINHA, 2013).

As ligas de titânio (Ti) são muito utilizadas em implantes no geral, devido às suas excelentes propriedades de biocompatibilidade, resistência a corrosão e módulo de elasticidade mais baixo do que de outras ligas metálicas (~110 GPa) (CHEN; THOUAS, 2015). Além disso, as ligas de titânio são capazes de formar um filme de óxido de titânio quando em contato com o ambiente oxidativo do corpo, o que protege o implante de corrosão e melhora a sua biocompatibilidade (CASALETTO et al., 2001). As ligas de titânio podem ser classificadas de acordo com sua microestrutura, em α, quase-α, α+β e β, sendo que a fase α corresponde à estrutura cristalina hexagonal compacta e a fase β à estrutura cúbica de corpo centrado (ZHANG; CHEN, 2019). A primeira geração de ligas de titânio começou a ser utilizada por volta de 1940, principalmente com titânio puro comercial (α) e ligas de Ti6Al4V (α+β) (HUANG et al., 2020).

O titânio puro comercial (ASTM F1341) tem aplicações mais restritas considerando a baixa resistência mecânica (LI et al., 2020b). Com a estabilização da fase β à temperatura

ambiente nas ligas de Ti, por meio da adição de estabilizadores da fase β como o vanádio, é possível melhorar propriedades como a resistência mecânica e a processabilidade das ligas (LI et al., 2020b). As ligas de Titânio-6Alumínio-4Vanádio (Ti6Al4V) (ASTM F136) são versáteis e muito utilizadas na indústria aeroespacial (SAMUEL; MISHRA; MISHRA, 2018). Entretanto, também foram verificadas como ótimas alternativas para implantes biomédicos, sendo biocompatíveis, com capacidade de osseointegração e apresentando maior resistência mecânica, comparadas ao Ti puro (ZHANG; CHEN, 2019).

A osseointegração de ligas de Ti são importantes vantagens desses biomateriais. Nemoto et al. (2014) mostraram que implantes de Ti6Al4V preenchidas com enxerto autólogo local apresentaram taxa de fusão intervertebral de 100% em 24 meses em estudos clínicos e radiológicos, o que foi estatisticamente superior aos implantes poliméricos de poli(éter-éter-cetona) (PEEK) nas mesmas condições (NEMOTO et al., 2014). Além disso, o Ti6Al4V também apresentou melhor adesão, diferenciação de osteoblastos e maior atividade de fosfatase alcalina (ALP) e níveis de proteína morfogenética óssea (BMP), quando comparado ao PEEK *in vitro* (OLIVARES-NAVARRETE et al., 2012). Por outro lado, algumas desvantagens das ligas de Ti são a rigidez, que pode estar associada a uma maior possibilidade de subsidência (CHEN et al., 2013; NEMOTO et al., 2014), e a possibilidade de que vanádio e alumínio possam estar relacionados a reações alérgicas e Alzheimer, respectivamente (KAUR; GHADIRINEJAD; OSKOUEI, 2019).

Não obstante, as ligas de Ti6Al4V são bem estabelecidas e muito utilizadas como implantes ósseos até hoje. Utilizando os cages interertebrais como exemplo, já existem muitas opções comerciais, como a VLIFT™ (Stryker, EUA) e a ENDOSKELETON™ TT (Medtronic, EUA). Entretanto, melhorias no processamento desse material, como modificações na porosidade, no desenho do implante e na superfície, com alteração na rugosidadde e adição de revestimentos, têm sido estudados para evitar a liberação de íons metálicos no organismo, reduzir a rigidez do implante e aumentar a osseointegração e adesão celular (DUX, 2019; RAO et al., 2014; WU et al., 2013). Tais melhorias ainda fazem da liga Ti6Al4V uma das alternativas mais promissoras.

O tântalo (Ta) também tem sido usado na produção de implantes com bons resultados clínicos de médio e longo prazo (FERNÁNDEZ-FAIREN; ALVARADO; TORRES, 2019). Embora o Ta puro apresente um módulo de Young de 186GPa, este material é utilizado em sua forma porosa para aplicações em implantes, conhecido como "metal trabecular". O Ta poroso tem menor rigidez (3GPa) (WARBURTON et al., 2020) e alta porosidade (80%), se

assemelhando ao osso trabecular, e apresenta boa biocompatibilidade, osteocompatibilidade e osseointegração (LEBHAR et al., 2020; LU et al., 2019). No entanto, o alto custo do tântalo é um fator limitante para sua aplicação (WARBURTON et al., 2020). Além disso, a suscetibilidade magnética do tântalo, ligas de titânio e outros metais pode criar artefatos de imagem que dificultam a visualização (ELLIOTT et al., 2016; RAO et al., 2014). Novas ligas que possam superar esse problema têm sido estudadas, mas ainda estão em fases experimentais (KODAMA et al., 2017).

Metais biorreabsorvíveis para aplicações na coluna vertebral focam principalmente em ligas de magnésio (Mg). As ligas de Mg são biocompatíveis, radiolúcidas, osteocondutoras (STAIGER et al., 2006), apresentam módulo de Young menor (≈ 45GPa) e podem se degradar completamente liberando íons de Mg que são naturalmente encontrados nos ossos (AGARWAL et al., 2016). Poucos estudos experimentais foram realizados com ligas de Mg, como Mg-Zn (XU et al., 2018) e ligas de magnésio AZ31 (DAENTZER et al., 2013, 2014; ZHANG et al., 2018a). No entanto, as altas taxas de corrosão das ligas de magnésio podem levar ao acúmulo de Mg, causando falha (ZHANG et al., 2018a). No entanto, mais estudos com outros revestimentos de polímeros podem ser conduzidos para superar esse problema. Ligas à base de zinco, manganês e ferro também são metais biorreabsorvíveis interessantes para aplicações ortopédicas (AGARWAL et al., 2016).

3.3.2. Polímeros

Biomateriais poliméricos, tanto os permanentes quanto os biorreabsorvíveis, têm sido explorados para aplicações ósseas devido à sua biocompatibilidade e versatilidade de estruturas e propriedades. Entretanto, poucos são capazes de fornecer o suporte mecânico necessário e normalmente são empregados no tratamento de pequenos ossos da mão, do pé ou da face. O poli(éter-éter-cetona) (PEEK) é um dos polímeros permanentes mais utilizados para implantes, por serem radiolucentes, biocompatíveis, bioinertes e apresentarem rigidez próxima ao módulo de Young do osso (3,6 GPa) (KERSTEN et al., 2015). Todavia, estudos mostraram que, enquanto o Ti favorece a osseointegração, o PEEK pode causar o desenvolvimento de tecido fibroso, que é prejudicial para o implante (OLIVARES-NAVARRETE et al., 2015). Desse modo, alternativas com polímeros biorreabsorvíveis contendo diferentes aditivos e atuando como preenchimentos, combinados com o titânio e

suas ligas como material estrutural, podem ser exploradas para trazer melhor funcionalidade ao implante.

Polímeros biorreabsorvíveis são os materiais mais usados como *scaffolds* para promover regeneração tecidual na forma de enxertos, revestimentos ou hidrogéis para biotintas, devido a sua biocompatibilidade, processabilidade e biorreabsorção. *Scaffolds* poliméricos biorreabsorvíveis podem ser processados com diferentes polímeros, técnicas, aditivos e taxas de degradação. Os polímeros biorreabsorvíveis aplicados como *scaffolds* podem ser polímeros naturais ou sintéticos.

Os polímeros naturais mais utilizados são as proteínas, com destaque para o colágeno. O colágeno (COL) é a proteína mais abundante que constitui a matriz orgânica dos ossos e tem sido muito estudada e comercializada para aplicações no osso (WANG; YEUNG, 2017; YANG et al., 2016), assim como a gelatina, derivada da desnaturação do colágeno (ECHAVE et al., 2019). A boa interação com as células e a bioatividade, são características importantes destas proteínas (SORUSHANOVA et al., 2019). Ozawa et al. (2018) comparou a aplicação de esponjas absorvíveis de colágeno com compósitos de colágeno e HA *in vivo* utilizando ratos. Ambos apresentaram bons resultados de formação de osso, com melhor regeneração obtida pelos compósitos de colágeno/HA (OZAWA et al., 2018).

Alguns exemplos de polímeros utilizados para regeneração óssea são os poliácidos lácticos (PLAs), poliuretanos (PU) e policaprolactonas (PCLs) (KNUTSEN et al., 2015). Os PLAs são poliésteres biodegradáveis que podem ser facilmente metabolizados e assumir diferentes taxas de degradação e propriedades físicas e mecânicas, de acordo com sua composição química (WUISMAN; SMIT, 2006). Alguns exemplos de PLAs são o ácido poli-L-láctico (PLLA) (KIM et al., 2017) e o poli (ácido lático-co-ácido glicólico) (PLGA), copolímero entre o PLA e o ácido poliglicólico (PGA). O PLGA é um polímero amorfo, biocompatível, biodegradável, que permite a adesão celular e com excelentes propriedades mecânicas, aprovado pela *Food and Drug Administration* (FDA) para aplicações médicas (GENTILE et al., 2014; LIN et al., 2019). Além disso, o PLGA apresenta rápida taxa de degradação, quando comparado a outros polímeros sintéticos, sendo completamente absorvido em um a seis meses, dependendo da razão de monômeros (ANSARY; AWANG; RAHMAN, 2014). Polímeros biorreabsorvíveis como o PLGA também podem facilmente incorporar aditivos (ZAMANI et al., 2020) como partículas osteocondutoras ou fármacos durante seu processamento.

3.3.3. Cerâmicos

Alguns materiais cerâmicos também foram estudados para o desenvolvimento de implantes estruturais. Nitretos de silício (Si3N4) são cerâmicas estáveis com alta resistência à compressão, osteocondutivas (KERSTEN et al., 2014), resistentes à atividade bacteriana e corrosão (BOCK et al., 2015; WEBSTER et al., 2012), radiolúcidas, hidrofílicas e com carga negativa (suportando a adesão celular) (ARTS; WOLFS; CORBIN, 2013). Embora mais estudos sejam necessários, ensaios *in vivo* e clínicos utilizando nitretos de silício preenchidos com enxertos mostraram resultados comparáveis ao PEEK (ARTS; WOLFS; CORBIN, 2017, 2013; KERSTEN et al., 2019, 2014). Modificações em nitretos de silício com aditivos também foram propostas para melhorar suas propriedades, fornecendo até mecanismos biodegradáveis (BOCK et al., 2015; FU et al., 2018). Outras cerâmicas também têm sido estudadas para aplicações ósseas, como alumina (MOSTOFI et al., 2018), vidros bioativos (LEE et al., 2020), apatita-wollastonita (BOZKURT et al., 2018), alumina (ABRAHAM; VENKATESAN, 2023) e zirconia (SIVASANKAR; CHINTA; SREENIVASA RAO, 2024).

Entretanto, as propriedades mecânicas dos materiais cerâmicos dificultam sua aplicação estrutural. Dessa maneira, a principal aplicação de cerâmicas em implantes ósseos é como aditivos, recobrimentos e enxertos para promoverem maior osteocondução. Fosfatos de cálcio, como hidroxiapatita (HA) e beta-trifosfato de cálcio (β-TCP) são os principais materiais inorgânicos osteocondutivos inspirados nos minerais dos ossos e utilizados como aditivos ou recobrimentos (CHAU et al., 2014; ZADEGAN et al., 2017). HAs ($Ca_{10}(PO_4)_6(OH)_2$) são cerâmicas biorreabsorvíveis com boas propriedades mecânicas e extensivamente usadas para aplicações ósseas devido aos seus bons resultados de osseointegração e biocompatibilidade (ZADEGAN et al., 2017).

3.3.4. Outros aditivos

Os implantes podem ser preenchidos ou revestidos por aditivos ou enxertos para melhor osseointegração. Os enxertos autólogos são interessantes, pois são os únicos materiais que apresentam todos os mecanismos de osseointegração, e não apresentam tantas complicações quanto os autólogos estruturais (MOBBS; CHUNG; RAO, 2013). Esses autólogos podem ser obtidos por coleta local durante o procedimento cirurgico (MOBBS;

CHUNG; RAO, 2013). Outra possibilidade, coletada do local cirúrgico do paciente, são as aspirações de medula óssea (BMAs), que contêm células tronco-mesenquimais (MSCs) e são osteogênicas e osteoindutivas (KURODA et al., 2011). Diferentes maneiras de incorporar as MSCs nos implantes também devem ser avaliadas para melhorar a osteogênese. Enxertos alógenos e xenógenos também foram tratados quimicamente para produzir versões comercializadas de enxertos com mecanismos de osteoindução e osteocondução (D'SOUZA et al., 2019; FISCHER et al., 2013). Os xenólogos são principalmente descelularizados e utilizados como Matriz Óssea Desmineralizada (DBMs) (BRACEY et al., 2018).

Os *scaffolds* ou revestimentos sintéticos também são promissores para a osseointegração de implantes e são principalmente baseados em polímeros biorreabsorvíveis contendo aditivos osteocondutivos, fármacos ou composto ansitmicrobianos. Os principais aditivos osteocondutivos, como abordado anteriormente, são inspirados pelos compostos inorgânicos e orgânicos mais presentes nos ossos (BUSER et al., 2016), como a HA (ZADEGAN et al., 2017) e o colágeno (WANG; YEUNG, 2017; YANG et al., 2016), respectivamente. Fatores de crescimento, como o fator de crescimento transformador-beta (TGF-β) e as proteínas morfogenéticas ósseas (BMPs) (CHEN; DENG; LI, 2012; VO; KASPER; MIKOS, 2012) também podem ser utilizados. As BMPs aprovadas para a osseointegração óssea são a BMP-2 e a BMP-7, que são fatores de crescimento osteogênicos e osteoindutivos e podem ser produzidos em versões humanas recombinantes (LIU et al., 2020b). A BMP-2 pode promover a diferenciação celular (CHEN; DENG; LI, 2012), enquanto a BMP-7 está relacionada à vascularização (BOON et al., 2011). Entretanto, esses fatores de crescimento possuem um preço muito elevado, limitando suas aplicações.

Partículas antimicrobianas, como quitosana e nanopartículas de prata ou zinco, (RODRIGUES et al., 2021a) e fármacos são outros aditivos interessantes para evitar infecções pós-operatórias (DELANEY et al., 2019), um dos maiores problemas relacionados a cirurgias com implantes. Fármacos são alternativas interessantes, uma vez que têm seu mecanismo de ação e eficácia bem definidos e aprovados. Entretanto, é necessário investigar como fazer sua aplicação efetiva em implantes ou *scaffolds* para liberação local. Portanto, alguns estudos têm focado na liberação de fármacos dos implantes como uma solução possível. A RIF é um exemplo de fármaco que pode ser adicionado ao *scaffold* para liberação local. Gilchrist et al. (2013) produziram membranas eletrofiadas de PLGA e ácido fusídico contendo diferentes concentrações de RIF. Neste estudo verificaram que com 5% m/m de

RIF ocorria uma liberação local controlada do fármaco e eficiente contra a adesão de bactérias do gênero *Staphylococcus* em implantes de Ti (GILCHRIST et al., 2013).

3.3.5. Processos de Fabricação

A estrutura de implantes ósseos, principalmente metálicos, pode ser fabricada utilizando diferentes técnicas de manufatura tradicionais, como metalurgia do pó e usinagem (KELLY et al., 2018). Entretanto, essas técnicas apresentam controle macro e microestrutural limitado. Técnicas de manufatura aditiva (MA) têm sido extensivamente estudadas para o desenvolvimento de implantes que apresentem melhor desempenho. A MA consiste na fabricação de objetos tridimensionais (3D) com a adição de camadas de material. Apesar de ser considerada uma técnica com custo mais elevado para produção em larga escala comparado a técnicas tradicionais (PEREIRA; KENNEDY; POTGIETER, 2019), a MA permite a construção de estruturas porosas, que podem ser customizadas e complexas (CHEN et al., 2019). Alguns exemplos de técnicas de MA muito utilizadas para a fabricação de estruturas metálicas são a Sinterização Seletiva a Laser (SLS) (KNUTSEN et al., 2015; MCGILVRAY et al., 2018), Fusão Seletiva a Laser (SLM ou PBF-LB) (CHEN et al., 2019) e a Fusão por Feixe de Elétrons (EBM ou PBF-EB) (LI et al., 2020b; TAKAHASHI et al., 2019). As técnicas de SLS, SLM e EBM são similares, uma vez que produzem sólidos 3D metálicos a partir da fusão parcial (SLS) ou total (SLM e EBM) de pós, utilizando laser (SLS e SLM) ou feixe de elétrons (EBM). O processo EBM é uma técnica de MA muito importante para o processamento de uma variedade de ligas metálicas e que possibilita maior produtividade e distribuição do campo térmico uniforme, que mitiga problemas com tensão residual e trincas (BIKAS; STAVROPOULOS; CHRYSSOLOURIS, 2016).

A fabricação das estruturas porosas através das técnicas de MA é muito importante para reduzir a rigidez do implante ósseo e melhorar sua osseointegração. Wu et al. (2013) produziram implantes de Ti6Al4V com alta porosidade e poros interconectados usando EBM (**Figura 3**). A rigidez do implante encontrada foi próxima ao módulo de Young do osso trabecular (~2,5 GPa). O desempenho *in vivo* dos implantes porosos foi avaliado e apresentou maior estabilidade mecânica e osseointegração quando comparadas aos implantes de PEEK preenchidos com enxertos autógenos (WU et al., 2013). Com relação ao tamanho de poros, alguns estudos com diferentes técnicas de MA buscaram comparar

algumas possibilidades para aplicações ósseas (Tabela 1), considerando que as células mais utilizadas para esses estudos são os osteoblastos que medem em torno de 20 a 50 μm (QIU; CUI; WANG, 2019).

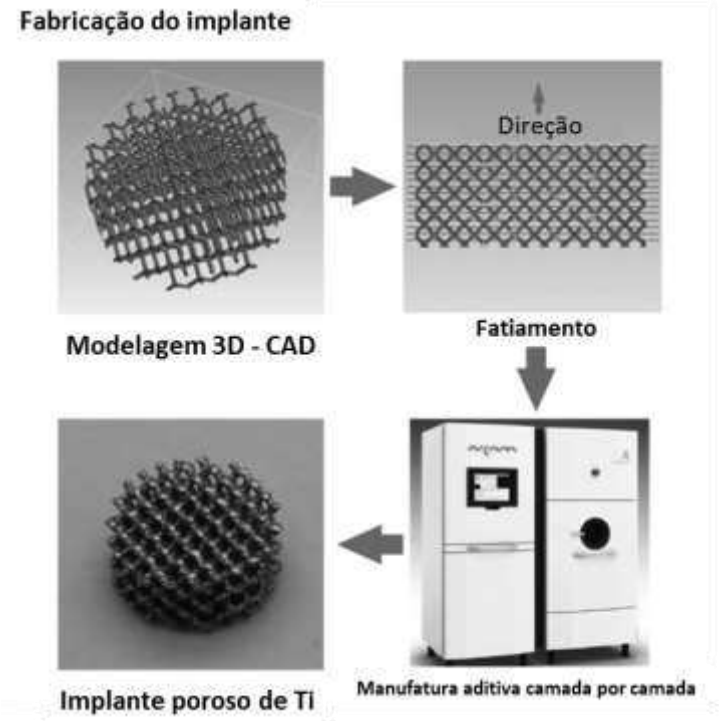

Figura 3. Processo de manufatura aditiva de liga de Ti.
Fonte: Modificada de WU et al., 2013

A MA também têm sido aplicada para a fabricação de *scaffolds* poliméricos, principalmente através de técnicas de (bio)impressão 3D. A (bio)impressão 3D, permite a fabricação de estruturas com alta complexidade, a partir de modelos 3D projetados em computador, utilizando biotintas (polímeros, principalmente hidrogéis) contendo células de interesse, para a funcionalidade necessária ao tecido (SHAHREZAIE et al., 2024). Além disso, as técnicas de processamento de membranas fibrosas têm se destacado para a fabricação de *scaffolds* poliméricos ao longo dos anos. Membranas fibrosas apresentam similaridade com a matrix extracelular, com grande área superficial, porosidade e permitem o transporte de nutrientes para a viabilidade e proliferação celular, promovendo a regeneração tecidual (DEFRATES et al., 2018). Algumas técnicas utilizadas são a eletrofiação, o *blow spinning,* a rotofiação e a fiação por fusão (MU et al., 2024). A eletrofiação produz fibras através da aplicação de uma diferença de potencial elétrico na solução polimérica (SHAHRIAR et al., 2019). Entretanto, o uso de altas tensões, risco à segurança, baixa produtividade, sensibilidade da solução à condutividade (ZHANG et al.,

2018b) e a possibilidade de desnaturação de proteínas no processo devido ao uso de altas tensões (ZEUGOLIS et al., 2008) são algumas desvantagens da eletrofiação.

Tabela 1. Técnicas e tamanho de poros na produção de implantes de titânio

Material	Técnica de MA	Tamanho de Poros	Referência
Titânio puro	SLM	300, 600 e 900 μm	(TANIGUCHI et al., 2016)
Titânio puro	SLM	200 e 500 μm	(WYSOCKI et al., 2016)
Ti6Al4V/ BMP-2	EBM	300, 600, 900 μm	(NUNE et al., 2016)
Ti6Al4V	SLM	200, 350, 500 μm	(YANG et al., 2017)
Ti6Al4V	EBM	200, 400, 600 μm	(NUNE et al., 2017)
Ti6Al4V	SLM	>300 μm	(DUMAS; TERRIAULT; BRAILOVSKI, 2017)
Ti6Al4V	SLM	600 μm	(RAN et al., 2018)
Ti6Al4V	SLM	>500 μm	(ZHANG et al., 2019)
Ti6Al4V	SLM	200 a 500 μm	(ALABORT; BARBA; REED, 2019)
Ti6Al4V	EBM	500 μm	(GAI et al., 2020)
Ti6Al4V	SLM	≥450 μm	(LIU et al., 2020a)
Ti6Al4V	SLM	600 μm	(BERGER et al., 2020)

Considerando tais limitações, a rotofiação foi desenvolvida e se destaca pela alta produtividade de fibras em escala micro e nanométrica (LI et al., 2018). A rotofiação é uma técnica relativamente simples que utiliza a força centrífuga de um reservatório com orifícios girando em alta velocidade para a extrusão da solução polimérica e formação de fibras (MINDRU et al., 2013) (**Figura 4**). A morfologia das fibras obtidas utilizando a rotofiação é influenciada por diferentes parâmetros como a viscosidade da solução e a velocidade de rotação do equipamento (LU et al., 2013).

Figura 4. Representação do equipamento de rotofiação utilizado para fabricação de membranas fibrosas. Modificada de RODRIGUES et al., 2020a.

A possibilidade de produção de membranas fibrosas em larga escala, com diferentes materiais e baixo custo são algumas vantagens que tornam esta técnica atrativa para fabricação de *scaffolds* (ROGALSKI; BASTIAANSEN; PEIJS, 2017). Comparada a eletrofiação, a rotofiação pode permitir a produção de fibras com uma taxa 500 vezes maior do que a eletrofiação (RODRIGUES et al., 2020b). A rotofiação tem sido especialmente estudada em trabalhos recentes para produzir *scaffolds* para regeneração óssea com diferentes tipos de polímeros contendo fatores de crescimento (RAMPICHOVÁ et al., 2017), partículas antimicrobianas (PADILLA-GAINZA et al., 2020) e materiais osteocondutivos (ANDRADE et al., 2019; LOORDHUSWAMY; THINAKARAN; VENKATESHWAPURAM RANGASWAMY, 2020; VASCONCELLOS et al., 2020). Vasconcellos et al. (2020) mostraram que membranas fibrosas de PCL contendo 20% m/m de HA podem ser produzidas por rotofiação com bons resultados *in vivo*, promovendo a regeneração óssea sem resposta inflamatória (VASCONCELLOS et al., 2020).

Entretanto, até o momento, não foram realizados estudos sobre a produção de membranas fibrosas de PLGA contendo HA, que são materiais altamente desejáveis para promover a osteocondução, utilizando a técnica de rotofiação. Além disso, a aplicação da rotofiação para combinar esses materiais com antibióticos para uso local ainda não foi explorada. Essa área de pesquisa representa uma oportunidade valiosa no campo da engenharia de tecidos ósseos, com potencial para produção em larga escala.

4 ANÁLISE BIBLIOMÉTRICA

As tendências no desenvolvimento de implantes e *scaffolds* podem ser melhor visualizadas por meio de análise bibliométrica. Para a visualização bibliométrica, documentos do banco de dados SciVerse Scopus foram coletados em 15 de maio de 2023. Os termos "implant OR *scaffold*" foram combinados com "osseointegration" para recuperar os dados. Os tipos de documentos foram limitados a "artigos" publicados em revistas em inglês de 2018 a 2022, recuperando 4173 documentos. O mapa de rede foi criado usando o software VOSViewer (Universidade de Leiden, Leiden, Holanda) e foi baseado na co-ocorrência de palavras-chave extraídas dos dados bibliográficos, com pelo menos cinquenta ocorrências. O software extraiu um total de 213 palavras-chave que foram filtradas manualmente em 100 termos relevantes para o desenvolvimento de implantes (Apêndice A).

O mapa de rede representa as ocorrências de palavras-chave com círculos e co-ocorrências com cores (**Figura 5**). O mapa de rede obtido mostra as principais tendências para implantes nos últimos 5 anos. O cluster laranja está relacionado aos efeitos dos materiais em células e estudos *in vitro*, com termos como "osteogenesis", "cell proliferation" e "mesenchymal stem cell". O cluster azul envolve propriedades importantes, como "biocompatibility", "antibacterial activity" e "bioactivity", e materiais relacionados a essas propriedades, como “hydroxyapatite”, “collagen” e “polymer”. Por fim, o cluster roxo está mais relacionado às aplicações clínicas e *in vivo* dos implantes, como "osseointegration", "prosthesis complication", "dental implants", "mechanical stress", entre outros.

Considerando o estado da arte em implantes e *scaffolds,* obtidos através dessa análise, foi possível avaliar as principais tendências atuais para osseointegração. As ligas de titânio se destacam como materiais, seguido de hidroxiapatita e polímeros. Algumas das propriedades mais evidentes na visualização são biocompatibilidade, bioatividade, hidrofilicidade, biomecânica, propriedades de superfície e atividade antibacteriana. A manufatura aditiva (impressão 3D) também destaca-se como uma importante técnica nos últimos 5 anos. Não obstante, este projeto investigou a integração das tendências mencionadas, que anteriormente eram abordadas de forma independente, além de combiná-las com métodos inovadores de processamento, como rotofiação e (bio)impressão 3D. Assim, o projeto assume uma relevância significativa no contexto da osseointegração de implantes e *scaffolds*, contribuindo para o avanço do estado da arte e para o desenvolvimento de produtos inovadores para aplicações médicas.

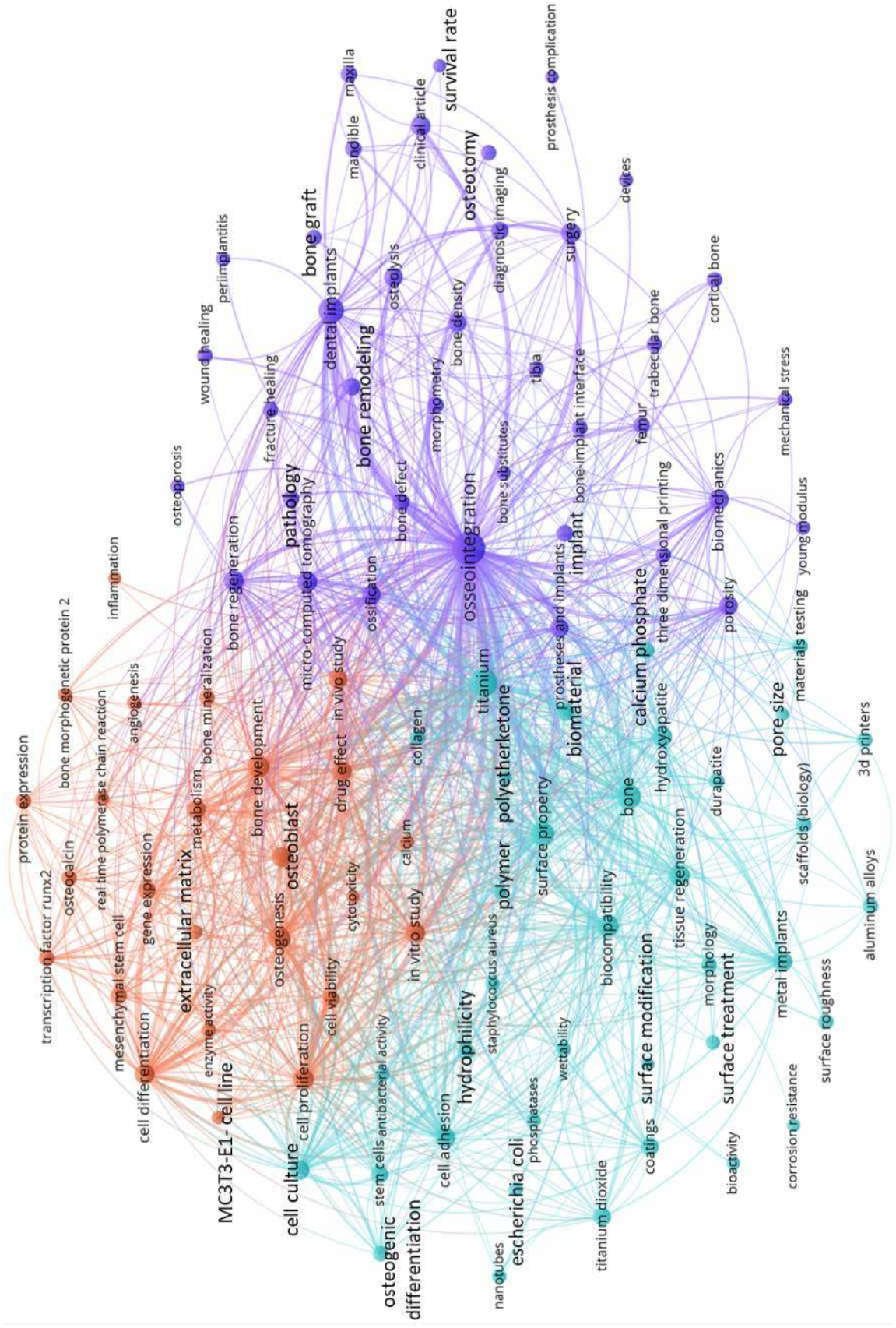

Figura 5. Mapa de visualização de rede de ocorrência de palavras-chave no desenvolvimento de implantes obtido pelo software VosViewer.

5 ANÁLISE EXPERIMENTAL

5.1. Preparo e Análise de Viscosidade da solução polimérica e Rotofiação dos *scaffolds*

As soluções poliméricas foram preparadas solubilizando PLGA (RESOMER® LG 824S, Evonik Brasil LTDA.) em clorofórmio ou hexafluorisopropanol (HFIP; #105228) e adicionando uma concentração em massa relativa do polímero de 10% e 20% m/m de HA (#677418, com tamanho de partícula <200 nm), 5% m/m de RIF (#R3501) e 1:3 de COL (colágeno bovino tipo I; #C9879), adquiridos na Sigma-Aldrich Brasil LTDA. As concentrações de HA e RIF foram definidas com base em outros estudos considerando, principalmente, a processabilidade em métodos de extrusão e bioatividade (HUANG et al., 2015; RUCKH; OLDINSKI, 2012; SENATOV et al., 2016). A viscosidade das soluções foi medida para diferentes concentrações de polímero usando um viscosímetro Brookfield LVDV1 com um spindle cônico SC4-34 e adaptador UL. O cisalhamento oscilatório foi de 60 rpm, e a temperatura foi de 25 ^{o}C.

Os *scaffolds* foram fabricados como membranas a uma velocidade de 6000 a 12000 rpm utilizando o equipamento de rotofiação presente no Laboratório de Ciência e Tecnologia de Polímeros (LPol) da Universidade Estadual de Campinas (UNICAMP). O equipamento de rotofiação consiste em um reservatório com quatro orifícios de 1mm de diâmetro, centralizado a uma distância de 17 cm do coletor (RODRIGUES et al., 2020a).

5.2. Preparo das tintas e biotintas e (bio)impressão

O GelMA foi sintetizado dissolvendo gelatina em PBS e posteriormente adicionando anidrido metacrílico para reagir com a gelatina, conforme protocolo estabelecido (LOESSNER et al., 2016). As moléculas de anidrido metacrílico não reagido foram removidas por diálise, e a solução final foi liofilizada e armazenada a -20 ºC até o uso posterior. Antes da bioimpressão, o GelMA liofilizado foi dissolvido em PBS, misturado com 0,3% v/v de fotoiniciador LAP e microfiltrado para esterilização para preparar o hidrogel. As células previamente cultivadas foram tripsinizadas, ressuspendidas em soro fetal bovino (FBS; #10437) contendo 1% v/v de Antibiótico-Antimicótico (#15240062), ambos da ThermoFisher Scientific, e misturadas com GelMA a uma concentração de 5×10^{6} células mL^{-1} para obter a biotinta.

Para as tintas poliméricas, o PLGA foi dissolvido em DMSO a uma concentração de 10% w/v, e a solução foi continuamente misturada a 90 ºC até ficar homogênea para preparar a tinta de PLGA. Para a tinta de PLGA-HA, 10% w/w de HA foram homogeneizados na solução. Após isso, a seringa foi preenchida com a tinta de PLGA ou PLGA-HA, mantida a 50 ºC e extrudado a 15 psi, de acordo com os códigos-G projetados usando o software Repetier-Host (uma única camada de grades quadradas de 15 mm com nove poros quadrados de aproximadamente 4 mm cada) a 3 mm s^{-1}. Os *scaffold*s foram impressos usando uma bioimpressora de extrusão Allevi 2 (3D Systems, Rock Hill, SC, EUA).

Para coextrusão, a outra seringa na bioimpressora foi preenchida com a biotinta de GelMA, preparada a 37 ºC com um passo de resfriamento a 4 ºC por 5 minutos, e extrudado a 30 psi, simultaneamente com a tinta à base de PLGA. Os *scaffolds* (bio)impressos finais foram expostos à luz ultravioleta (UV) (13,0 W cm−2 por 30 s) para serem foto-reticulados para as porções de GelMA. Posteriormente, os *scaffolds* (bio)impressos foram lavados com DPBS e meio MSC para troca de solvente/não solvente, e incubados com meio MSC por 1, 3, 7 e 14 dias. . A biotinta de GelMA também foi extrudada sozinha, formando *scaffolds* de GelMA puro que foram incubados para comparação com os *scaffold*s coextrudados.

5.3. Caracterização reológica das tintas e biotinta

A viscosidade aparente e a viscoelasticidade dependente da temperatura das tintas à base de PLGA foram medidas em um reômetro DHR-3 (TA Instruments) com geometria de placa de 40 mm de diâmetro (placa Peltier de aço). A altura foi ajustada para 1 mm para as amostras. As viscosidades aparentes das soluções de tinta foram medidas de 0,1 a 100 s^{-1} usando uma varredura de fluxo em estado estacionário a uma temperatura constante. Varreduras de temperatura oscilatórias foram realizadas de 60 a 30 °C para o PLGA e de 15 a 37 °C para o GelMA a uma taxa de rampa de 2–3 °C min^{-1} a uma deformação de cisalhamento de 1% e uma frequência de 1 Hz.

5.4. Modelagem e fabricação das estruturas metálicas

Os modelos de estrutura metálica para este estudo foram projetados a partir de células unitárias cúbicas centradas no corpo (CCC) utilizando o software nTopology (nTopology Inc., NY, EUA). Estruturas tubulares com dimensões de 6 mm de diâmetro externo, 3 mm de diâmetro interno e 9 mm ou 3 mm de comprimento, e diferentes tamanhos de poros (300,

450 e 600 µm) foram fabricadas. As estruturas de manufatura aditiva (AM) foram produzidas utilizando a tecnologia de fusão de leito de pó por feixe de elétrons (PBF-EB) com o modelo Q10 da Arcam EBM (Arcam EBM, GE Additive Company). Um pó de liga de Ti6Al4V (Spectra H Ti6Al4V Grade 5, fornecido pela Ge Additive Company) foi utilizado para produzir as estruturas. A plataforma foi pré-aquecida a 495 °C em uma atmosfera de trabalho de 1x10-3 mbar de hélio e alto vácuo, uma velocidade de varredura de 4530 mm/s com um deslocamento de foco de 36 mA e uma espessura de camada de 50 µm foram empregadas no processo. O pó metálico utilizado apresentou partículas de 45 a 106 µm (MOURA et al., 2020).

5.5. Caracterização de propriedades morfológicas, químicas, térmicas e estruturais

A caracterização morfológica dos *scaffold*s foi realizada por microscopia eletrônica de varredura (MEV). Primeiramente, as amostras foram metalizadas com ouro utilizando o metalizador Quorum SC7620 antes da análise por MEV. Posteriormente, um microscópio modelo ZEISS EVO® MA 15 com tensão de operação de 10 kV foi utilizado para observar as amostras. O diâmetro de 50 fibras dos *scaffold*s produzidos foram medidas utilizando o software ImageJ para obter os histogramas. A morfologia das partículas de nHA e RIF foi analisada utilizando Microscopia Eletrônica de Transmissão (TEM). As micrografias foram obtidas com o Microscópio Eletrônico de Transmissão JEOL JEM-1400 (Tóquio, Japão), operando com uma voltagem de aceleração de 120 kV.

A composição química dos *scaffolds* foi caracterizada por espectroscopia de infra-vermelho (FTIR) utilizando um espectrômetro de infra-vermelho modelo PerkinElmer Spectrum 100 de reflectância total atenuada (ATR). O espectro foi obtido utilizando um comprimento de onda de 650 a 4000 cm^{-1}, com 16 varreduras e 4 cm^{-1} de resolução. A análise foi realizada no Centro de Tecnologia da Informação “Renato Archer” (CTI). A caracterização térmica do *scaffold* foi realizada por termogravimetria (TGA) em um equipamento 2950 thermogravimetric analyzer (TA Instruments, USA) presente na Central Analítica do Instituto de Química da UNICAMP. Para a caracterização utilizou-se aproximadamente 5 mg de amostras, atmosfera inerte de argônio com fluxo de 60 mL/min e temperatura de 25 ^{o}C até 600 ^{o}C com taxa de aquecimento de 10 ^{o}C/min. A avaliação microestrutural dos *scaffold*s foi realizada por difração de raios-X (DRX) em um

difratômetro modelo X'Pert (Panalytical) presente no laboratório multiusuário da engenharia na Faculdade de Ciências Aplicadas (FCA) da UNICAMP. A difração de raios-X foi realizada com radiação de Cu-Kα, tensão de 40 kV e corrente de 30 mA, com intervalo angular de 5º a 80º e passo angular de 0,016º.

As microestruturas dos *scaffolds* impressos foram avaliadas usando um microscópio de fluorescência (Axio observer, Carl Zeiss, Oberkochen, Alemanha). Rodamina B, um corante fluorescente (#83689; Sigma-Aldrich), foi adicionada aos polímeros. As microestruturas foram analisadas, e 40 tamanhos de poros foram medidos usando o software ImageJ para plotar os histogramas. Os valores de porosidade foram avaliados usando densidade aparente e densidade global. A densidade aparente foi determinada medindo a massa e o volume dos *scaffold*s impressos após secagem a vácuo. A densidade global foi determinada medindo a massa e o volume dos *scaffolds* após injeção em um molde com volume conhecido.

Já para os implantes de Ti6Al4V, a densidade e porosidade das estruturas de Ti6Al4V foram avaliadas usando um picnômetro de gás hélio (Micromeritics AccuPyc 1330) após limpeza ultrassônica com etanol e secagem. Além disso, imagens de MEV foram analisadas, e as dimensões de 5 poros das estruturas de Ti6Al4V foram medidas usando o ImageJ. Para os testes, foram utilizados quatro corpos de prova tubulares para cada tamanho de poro, todos com altura de 9 mm, diâmetro externo de 6 mm e diâmetro interno de 3 mm.

5.6. Avaliação da hidrofilicidade e degradação *in vitro*

A hidrofilicidade do *scaffold* foi avaliada através do ensaio de ângulo de contato, conforme a ASTM D7334. O equipamento Dataphysics modelo OCA15 presente no CTI foi utilizado para as medições de ângulo de contato estático, no qual uma gota de água deionizada foi adicionada à superfície dos *scaffold*. O experimento foi realizado usando quatro replicatas para cada *scaffold* e os ângulos entre a gota e a superfície do *scaffold* foram obtidos utilizando o software ImageJ. A degradação hidrolítica dos *scaffolds* foi avaliada *in vitro* de acordo com a norma ASTM F1635-11. Os *scaffolds* foram inicialmente pesados e imersos em PBS com pH de 7,4 e mantidos a uma temperatura de 37 °C. Após intervalos de tempo específicos, as amostras foram retiradas da solução, secadas a vácuo e pesadas novamente para avaliar as alterações de peso ao longo do tempo.

5.7. Avaliação da eficiência de encapsulamento e liberação de fármaco do *scaffold*

A análise de encapsulamento e liberação de RIF foi conduzida utilizando espectroscopia ultravioleta-visível (UV-Vis) a um comprimento de onda de 483 nm com o equipamento FilterMax F5 Multimode. Primeiramente, a eficiência de encapsulamento, no caso de incorporação da RIF ao polímero, foi determinada dissolvendo-se os *scaffolds* de PLGA-HA-RIF em 5 mL de clorofórmio por meio de agitação ultrassônica e subsequente centrifugação por 5 minutos. Os *scaffolds* pesando aproximadamente 10 mg foram incubados em 10 mL de PBS (pH 7,4) a 37 °C e 100 rpm. A liberação foi medida de 0 a 720 horas, com 4 mL da solução retirados em intervalos de tempo específicos para análise espectrométrica. O volume retirado foi substituído por um volume equivalente de PBS fresco. Os experimentos foram realizados com quatro replicatas. A liberação foi avaliada empregando diversos modelos cinéticos, incluindo ordem zer, primeira ordem, Higuchi, Hixson-Crowell, Korsmeyer-Peppas e Weibull.

5.8. Ensaios de atividade antibacteriana

A atividade antibacteriana foi avaliada por meio do teste de difusão em disco de acordo com a norma M02-A8 da ANVISA. Para o ensaio, bactérias gram-positivas (*Staphylococcus aureus*, ATCC 6538) e gram-negativas (*Escherichia coli*, cepa K-12) foram inoculadas em meio LB até atingir uma turbidez óptica de 0,5 e, em seguida, incubadas em placas de ágar. Os *scaffold*s e implantes de Ti6Al4V contendo 7 μg de PLGA-HA-RIF foram adicionados às placas de ágar para avaliar a zona de inibição. Os diâmetros dos halos foram medidos usando o ImageJ. Os *scaffold*s de PLGA-HA e as estruturas de Ti6Al4V foram usados como controle para comparar com os implantes de Ti6Al4V contendo *scaffold*s de PLGA-HA-RIF e PLGA-HA-RIF. Os ensaios foram realizados no Centro Pluridisciplinar de Pesquisas Químicas, Biológicas e Agrícolas (CPQBA)

5.9. Ensaios Mecânicos de Compressão

As propriedades mecânicas das estruturas de Ti6Al4V foram avaliadas por meio de testes de compressão de acordo com a ASTM E9-19. Os testes de compressão foram realizados usando uma máquina de ensaio universal (WDW-100E) com uma célula de carga

de 100kN e uma velocidade de 1mm/min. A rigidez foi calculada como a inclinação da porção linear das curvas tensão-deformação obtidas.

As propriedades de tração dos *scaffold*s poliméricos impressos foram medidas usando uma máquina de ensaio mecânico (Instron série 6800, Norwood, MA, EUA) com uma célula de carga de 100 N. Para isso, os insumos de PLGA e PLGA-HA foram moldados em moldes retangulares de PDMS de 30×10 mm^2. As amostras foram submetidas a um processo de troca de solvente em água por 15 minutos, 24, 48, 96, 168 e 336 horas para as análises. Após secagem superficial, as amostras foram fixadas nas garras e submetidas a um teste de tração (ASTM D638-14), onde o comprimento de medição (~15 mm), espessura (~0,5 mm) e largura (~10 mm) foram determinados, e a taxa de deformação foi fixada em 5 mm/min. As resistências e deformações na ruptura, e os módulos foram determinados calculando as inclinações da porção elástica linear das curvas tensão-deformação.

O teste de cisalhamento foi realizado em um sistema de teste mecânico (célula de carga de 100 N, Instron 3342). Amostras retangulares em bicamada (16 mm por 15 mm por 1,5 mm, comprimento por largura por espessura) foram preparadas adicionando o GelMA sobre a tinta de PLGA. Após fotoendurecimento e imersão em PBS, as amostras foram fixadas entre duas lâminas de vidro com supercola. Os dois lados dos vidros foram fixados nos dispositivos inferior e superior para alongamento a 10 mm/min. A tensão de cisalhamento foi calculada pela força medida dividida pela área de sobreposição (ou área da amostra).

Além disso, as propriedades compressivas dos *scaffold*s bioimpressos foram examinadas de acordo com a ASTM D695-15. Para isso, os mesmos volumes de tinta polimérica e biotinta de GelMA foram adicionados, um sobre o outro, em um molde cúbico de PDMS de 10×10×10 mm^3. Os testes de compressão foram realizados a uma taxa fixa de 0,5 mm/min. A resistência à compressão e deformação foram determinadas no momento da falha ou na compressão total. O módulo de elasticidade compressivo foi calculado como a inclinação da região linear das curvas tensão-deformação.

5.10 Ensaio de osteocondução

A osteocondução foi avaliada através da formação *in vitro* de apatita no implante utilizando fluido corpóreo simulado (SBF), conforme a norma específica da ABNT NBR ISO 23317:2017. Para o experimento, amostras do *scaffold* foram cortadas em quadrados

com 15 mm de lado e imersas em 40 mL de solução SBF a uma temperatura de 37 ºC. Após quatro semanas, as amostras foram retiradas, enxaguadas com água destilada e secadas. A apatita foi detectada na superfície dos *scaffolds* utilizando MEV e DRX. Além disso, Espectroscopia de Raios-X por Energia Dispersiva (EDS) foi utilizada para análise da composição elementar dos implantes após a formação de apatita.

5.11. Análise de viabilidade, proliferação, morfologia e diferenciação celular

5.11.1. Pré-Osteoblastos MC3T3

A viabilidade dos *scaffold*s foi analisada por meio de ensaio de brometo de 3(4,5-dimetiltiazol-2-il)-2,5-difeniltetrazólio (MTT), utilizando células pré-osteoblastos (MC3T3-E1). As células foram cultivadas em meio mínimo essencial alfa (α-MEM) suplementado com soro fetal bovino, penicilina e estreptomicina a 37 ºC e 5% CO_2. A atividade metabólica das células foi medida por absorbância a 570 nm após 24, 48 e 72h em contato com as membranas e comparadas com o controle (células na placa de 96 poços). Já para a análise de morfologia e adesão celular, as células foram cultivadas na superfície dos *scaffold*s por 72 h e fixadas com 3,7% (v/v) de formaldeído por 5 min. Após lavagem com PBS, 50 μg mL^{-1} de faloidina foram adicionados a temperatura ambiente. Lavou-se novamente com PBS e adicionou-se 0.1 μg mL^{-1} de DAPI por 15 min a 37 ºC. A microscopia confocal foi realizada com um microscópio Leica TCS SP5 II no Laboratório Central de Tecnologias de Alto Desempenho (LAcTAD) e no Instituto Nacional de Fotônica Aplicada à Biologia Celular (INFABIC). Os ensaios com as células foram realizados no Laboratório de Biotecnologia da FCA-UNICAMP.

5.11.2. Células-Tronco Mesenquimais

A viabilidade das células nos *scaffold*s (bio)impressos foi avaliada em 1, 3, 7 e 14 dias usando o ensaio Live/Dead. O kit contendo calceína-AM (C3100MP), para colorir células vivas, e etídio homodímero-1 (E1169), para colorir células mortas, foi adquirido na ThermoFisher Scientific, e os experimentos foram conduzidos seguindo o protocolo do fabricante. As imagens foram capturadas usando o microscópio de fluorescência. O número de células vivas e mortas em 6 imagens aleatórias para cada *scaffold* foi contado usando o software ImageJ com o plugin Analyze particles.

O ensaio de [3-(4,5-dimetiltiazol-2-il)-5-(3-carboximetoxifenil)-2-(4-sulfonfenil)-2H-tetrazolium] (MTS) foi usado para medir a absorbância do formazan para quantificação da proliferação celular em 1, 3, 7 e 14 dias nos *scaffold*s (bio)impressos. A solução de MTS foi preparada utilizando o meio MSC e o reagente MTS (#G1111) da Promega Corporation (Madison, WI, EUA) na proporção de 3:1 v/v. Após a remoção do meio, 1 mL da solução de MTS foi adicionado a cada poço. Após incubação por 3 horas a 37 ºC, o sobrenadante foi lido por um espectrofotômetro (SpectraMax M3, Molecular Devices, San Jose, CA, EUA) a 490 nm para quantificação. Seis amostras foram medidas para cada tipo de *scaffold* (bio)impresso em cada ponto de tempo.

Para coloração de F-actina e núcleos, as amostras foram fixadas em 1, 3, 7 e 14 dias de proliferação, e após 1, 2 e 4 semanas de diferenciação, com uma solução de formalina a 10% p/v (#F5554; Sigma-Aldrich) por 15 minutos à temperatura ambiente. Em seguida, as amostras foram lavadas com DPBS e bloqueadas com uma solução de albumina sérica bovina (BSA) a 5% v/v (#A3983; Sigma-Aldrich) em DPBS à temperatura ambiente por 1 hora. Após o bloqueio, a solução de BSA foi removida, e uma solução de Alexa Fluor 594-faloidina (#A12381; ThermoFisher Scientific) em DPBS na proporção de 1:400 v/v foi adicionada às amostras e deixada durante a noite a 4 ºC. A solução de faloidina foi removida, e as amostras foram lavadas com DPBS; em seguida, as amostras foram incubadas com solução de 4',6-diamidino-2-fenilindol (DAPI; #D1306, ThermoFisher Scientific) em DPBS diluída a 1:5000 v/v por 15 minutos, lavadas e analisadas usando o microscópio de fluorescência. Para avaliar a dispersão celular, as áreas de 20 células foram medidas nas imagens utilizando o ImageJ.

Após 14 dias de cultivo, os *scaffolds* contendo MSCs foram cultivados no meio de diferenciação (Human MSC Osteogenic Differentiation Medium BulletKit™, #PT-3002) da Lonza Bioscience por 1, 2 e 4 semanas. Para o ensaio de imunofluorescência, as amostras foram fixadas nas semanas 1, 2 e 4 com solução de formalina a 10% p/v (Sigma-Aldrich) por 15 minutos à temperatura ambiente. Em seguida, as amostras foram lavadas com PBS e solução de lavagem 1% v/v BSA/PBS. Após a lavagem, as amostras foram incubadas em um tampão de bloqueio contendo 5% v/v de solução de BSA/PBS e 0,2% v/v de Triton X-100 (#T8787; Sigma-Aldrich) em PBS à temperatura ambiente por 2 horas. As amostras foram então incubadas com duas soluções de anticorpos primários, anticorpo anti-RUNX2 de camundongo (#ab76956; Abcam) em solução de PBS diluída a 1:200 v/v e anticorpo anti-OCN de coelho (#ab198228; Abcam) em solução de PBS diluída a 1:200 v/v a 4 ºC durante

a noite. Após isso, as amostras foram lavadas com a solução de lavagem e tratadas com anticorpos secundários correspondentes, anticorpo Alexa Fluor Plus 488 de cabra anti-IgG de camundongo H&L (#ab150113; Abcam) em solução de PBS diluída a 1:200 v/v e anticorpo Alexa Fluor Plus 555 de cabra anti-IgG de coelho H&L (#ab150080; Abcam) em solução de DPBS diluída a 1:200 v/v à temperatura ambiente por 2 horas. Em seguida, os espécimes foram lavados com PBS e incubados com DAPI em solução de PBS diluída a 1:1000 v/v à temperatura ambiente por 15 minutos. Por fim, as amostras foram lavadas e analisadas usando um microscópio de fluorescência.

5.12. Análise Estatística

Os experimentos tiveram resultados expressos como média ± desvio padrão. O teste t de Student ou de análise de variância *One-way* (ANOVA) foram utilizados para comparação das amostras. As análises estatísticas foram realizadas utilizando o *software* IBM SPSS Statistics 22.0.

6 RESULTADOS: ARTIGOS PUBLICADOS E SUBMETIDOS

Nesta seção os resultados e discussões estão apresentados na forma de manuscritos de artigos científicos independentes, no idioma exigido pelos veículos de divulgação onde foram ou serão publicados. O primeiro manuscrito submetido, intitulado “Osteoconductive composite membranes produced by rotary jet spinning of bioresorbable PLGA present pioactivity for bone regeneration”, apresenta o potencial da rotofiação para produção de membranas baseadas em PLGA e HA(NPs) para promover regeneração óssea. Nesse estudo, os parâmetros de processo foram avaliados para obtenção das membranas, que foram caracterizadas por suas propriedades morfológicas, químicas, térmicas e estruturais. Além disso, a bioatividade, viabilidade celular e adesão nas membranas de PLGA-HA(NPs) foram analisadas e comparadas com as membranas de PLGA, mostrando resultados promissores para engenharia tecidual óssea.

O segundo manuscrito submetido “Implants promoting osteoconduction and local antibacterial activity for effective osseointegration and osteomyelitis prevention” propõe o desenvolvimento de novos implantes que permitam osseointegração, compatibilidade mecânica e prevenção local de bactérias. Dessa maneira, este estudo mostra uma nova combinação de técnicas de processamento, materiais e análises com potencial para regeneração óssea. Para isso, implantes porosos de Ti6Al4V produzidos por MA foram combinados com membranas rotofiadas de PLGA-HA-RIF e PLGA-COL-HA para obter implantes ósseos com resistência mecânica e rigidez compatíveis com o osso para aplicações de suporte de carga, propriedades osteocondutoras e prevenção de infecção bacteriana. A partir desse estudo, a patente “Processo de Produção de Enxerto Ósseo e Enxerto Ósseo Assim Obtido” foi depositada no Instituto Nacional da Propriedade Industrial (INPI) no dia 30 de janeiro de 2024 com o número BR102024001943-1.

Por fim, o terceiro manuscrito intitulado "Multimaterial coextrusion (Bio)printing of composite polymer biomaterial ink and hydrogel bioink for tissue fabrication" apresenta pela primeira vez uma estratégia combinatória de (bio)impressão 3D para permitir a coextrusão multimaterial de polímero-nanopartícula e biotinta para aplicações ósseas. Para demonstrar a versatilidade e singularidade da estratégia, foram realizados experimentos de coextrusão envolvendo PLGA puro e PLGA-HA impressos simultaneamente com GelMA contendo células-tronco mesenquimais humanas (MSCs). As propriedades morfológicas, químicas,

mecânicas e estruturais dos *scaffolds* (bio)impressos foram caracterizadas. Além disso, foram realizadas avaliações detalhadas dos *scaffolds* (bio)impressos durante o cultivo, abrangendo aspectos cruciais como propriedades mecânicas, viabilidade, proliferação e diferenciação das MSCs, mostrando seu potencial em aplicações ósseas. O artigo foi publicado na revista Composites Part B: Engineering no dia 15 de abril de 2024 (DOI: 10.1016/j.compositesb.2024.111337). A autorização da editora para adição do artigo na tese encontra-se no Apêndice B.

A discussão consolidando os artigos apresentados está descrita no próximo capítulo.

6.1. Manuscrito do Artigo 1

Osteoconductive composite membranes produced by rotary jet spinning of bioresorbable PLGA present bioactivity for bone regeneration

Isabella Caroline Pereira Rodrigues[1], Karina Danielle Pereira[2,3], Augusto D. Luchessi[2,3], Éder Sócrates Najar Lopes[1*], and Laís Pellizzer Gabriel[2]

[1] School of Mechanical Engineering, University of Campinas, Campinas, São Paulo, Brazil
[2] School of Applied Sciences, University of Campinas, Limeira, São Paulo, Brazil
[3] Institute of Biosciences, São Paulo State University, Rio Claro, São Paulo, Brazil
* Correspondence to: Éder Sócrates Najar Lopes (E-mail esnlopes@unicamp.br; Telephone: +55 (19) 3521-0017; Street address: Rua Mendeley, 200, Campinas 13083-860, SP, Brazil)

ABSTRACT

Bone defects and injuries are common and need better solutions for improved regeneration and osseointegration. Bioresorbable membranes hold great potential in bone tissue engineering due to their high surface area and versatility. In this context, polymers such as poly(lactic-co-glycolic acid) (PLGA) can be combined with osteoconductive materials like hydroxyapatite (HA) nanoparticles (NPs) to create membranes with enhanced bioactivity and bone regeneration. Rotary Jet spinning (RJS) is a powerful technique to produce these composite membranes. This study presents an innovative and efficient method to obtain PLGA-HA(NPs) membranes with continuous fibers containing homogeneous HA(NPs) distribution. The membranes demonstrated stable thermal degradation, allowing HA(NPs) quantification. In addition, the PLGA-HA(NPs) presented osteoconductivity, were not cytotoxic, and had high cell adhesion when cultured with pre-osteoblastic cells. These findings demonstrate the potential of RJS to produce PLGA-HA(NPs) membranes for easy and effective application in bone regeneration.

Keywords: Ceramics; Centrifugal Spinning; Fibers; Hydroxyapatite; Nanoparticles; Osseointegration; Scaffolds; Tissue Engineering;

INTRODUCTION

Bone tissue engineering (BTE) techniques have emerged as crucial tools in the field of regenerative medicine, particularly for promoting mechanisms like osteoconduction, which are essential for effective bone regeneration. Osteoconductive scaffolds comprise bioresorbable biomaterials that promote and guide the growth of new bone tissue into the bone defect area or implant for better osseointegration. Calcium phosphates, such as hydroxyapatite (HA) and beta-tricalcium phosphate (β-TCP), are the primary osteoconductive inorganic materials inspired by bone minerals and used as additives/coatings [1,2]. HA nanoparticles (NPs) are bioresorbable ceramics with good mechanical properties that are extensively used for bone applications due to their excellent biocompatibility and bioactivity, promoting apatite deposition [2]. However, due to their brittleness, the limited processability of HA(NPs) hinders their ability to produce bulk structural scaffolds [3].

To solve this drawback, extensive research has been conducted on composite scaffolds based on combining polymers and ceramics. Many polymers have been studied as scaffolds for BTE [4]. Poly (lactic-co-glycolic acid) (PLGA) stands out as a bioresorbable polymer with excellent biocompatibility that allows cell adhesion and proliferation. Regulatory agencies worldwide have approved biomedical implants made with PLGA for medical applications [5,6]. Due to the monomers that compose this copolymer, poly-L-lactic acid and poly(glycolic acid), it can be easily absorbed, participating in the primary metabolic cycles of the body. Thus, it presents faster absorption than other synthetic polymers [7].

Fiber processing techniques are a viable alternative for producing polymeric/ceramic-based scaffolds. Fibrous membranes are scaffolds with great similarity with the extracellular matrix, a large surface area, and porosity, able to transport nutrients for cell viability and proliferation, promoting tissue regeneration [8]. Electrospinning (ES) and rotary jet spinning (RJS) are some techniques used for composite membrane production. Many studies used ES for membrane fabrication with HA [9–11]. However, other works showed that RJS can produce 500 times more fibers than ES [12]. Moreover, RJS can produce fibrous membranes on a large scale, with different materials and low cost, making it a promising technique for scaffold development.

Therefore, this study aimed to produce new osteoconductive composite membranes based on PLGA and HA(NPs) using RJS. Although some studies have produced membranes with different polymers containing osteoconductive materials [13–17], this is the first work to explore RJS with the strong combination of HA(NPs) and PLGA, which can enhance the membrane's biological performance for bone applications. Thus, process parameters were thoroughly evaluated to obtain optimized composite membranes characterized by their morphological, chemical, thermal, and structural properties. Moreover, the bioactivity, cell viability, and adhesion on the PLGA-HA(NPs) membranes were analyzed and compared to those of the PLGA membranes, showing promising results for bone regeneration.

MATERIALS AND METHODS

Solution, viscosity analysis, and processability

The polymeric solutions were prepared by dissolving PLGA (Resomer® LG 824S, Evonik Brasil LTDA.) in chloroform, and a relative weight concentration of 10% w/w of HA(NPs) (<200 nm particle size, #677418, Sigma-Aldrich Brasil LTDA.) was added for PLGA-HA membranes. The solutions' viscosity was measured for different polymer concentrations using a Brookfield LVDV1 viscometer with an SC4-34 conic spindle and UL adapter. The oscillatory shear was 60 rpm, and the temperature was 25 ºC. The composite membranes were fabricated at 6000, 9000, and 12000 rpm using the RJS process. The RJS equipment comprises a reservoir with four 1 mm diameter orifices centralized at 17 cm from the collector [18].

Characterization of morphological, chemical, structural, and thermal properties

The morphological characterization of the composite membranes was performed by scanning electron microscopy in secondary electron mode (SEM-SE). Firstly, samples were gold-coated using a Quorum SC7620 sputter coater before SEM analysis. Subsequently, a ZEISS EVO® MA 15 microscope with an operating voltage of 10 kV was used to observe the samples. The diameter of 50 fibers from the produced composite membranes was measured using ImageJ software to obtain the histograms. Energy Dispersive X-ray Spectroscopy (EDS) was also performed for chemical analysis of elemental composition using the EDS analyzer at the SEM microscope. HA(NPs) morphology was examined using Transmission Electron Microscopy (TEM). The JEOL Transmission Electron Microscope JEM-1400 (Tokyo, Japan) was used to obtain the micrographs at an accelerating voltage of 120 kV.

Fourier-transform infrared (FTIR) spectroscopy characterized the composite membranes' chemical composition using a PerkinElmer Spectrum 100 with a total attenuated reflectance (ATR) infrared spectrometer. The spectrum was obtained using a wavelength range of 650 to 4000 cm^{-1}, with 16 scans and a resolution of 4 cm^{-1}. Unprocessed (as received) HA(NPs) and PLGA were also characterized to comparison. The crystalline features of composite membranes were analyzed by X-ray diffraction (XRD) using an X'Pert diffractometer (PanAlytical). X-ray diffraction was performed with Cu-Kα radiation, 40 kV voltage, and 30 mA current, with an angular 2θ ranging from 5º to 80º and an angular step of 0.016º.

The thermal characterization of the composite membranes was performed by thermogravimetric analysis (TGA) using a 2950 thermogravimetric analyzer (TA Instruments, USA). Approximately 5 mg of samples were used, with an inert atmosphere of argon at 60 mL/min and a temperature of 25 °C to 600 °C with a heating rate of 10 °C/min.

In vitro bioactivity assay

The bioactivity of composite membranes used as scaffolds was evaluated by *in vitro* apatite formation on the membranes' surface using simulated body fluid (SBF) at 37 °C, according to the standard ISO 23317. After four weeks, the apatite formation was detected on the scaffolds' surface using SEM and XRD, as previously described.

MTT assay of scaffolds

Mouse preosteoblast cell line (MC3T3-E1) was cultured in Alpha Minimum Essential Medium (α-MEM) with 100 U/mL penicillin, 100 μg/mL streptomycin, and 10% fetal bovine serum (FBS) (Life Technologies, Inc., Carlsbad, CA, USA) in a 5% CO_2-contained humidified atmosphere at 37°C. When the cells reached 80% confluence, they were trypsinized, neutralized with α-MEM, and counted using a Countess II automatic counter. (Thermo Fisher Scientific Inc., Waltham, MA, USA). The composite membranes were arranged in a 96-well plate sterilized with UV light overnight, seeded with cells at a density of $8x10_3$ cells per well, and incubated in 100 μL of culture medium for 24, 48, and 72 h. The viability of cells was assessed by a modified 3-(4,5-dimethylthiazol-2-yl)-2,5-diphenyltetrazolium bromide (MTT) assay. After 24, 48, and 72 h, the media were removed, and MTT (0.5 mg/mL in PBS) solution was added to cells, followed by incubation for 3 h. The growth media was aspirated, and dimethyl sulfoxide (DMSO) was added. Absorbance was measured at 570nm with a scanning spectrophotometer (F5 Microplate Reader, Molecular Probes).

The adhesion of MC3T3-E1 cells was evaluated after cultivation on top of the membranes at a concentration of 1.0×10^5 cells per well. The membranes with cells were incubated at α-MEM, 37 °C, and 5% CO_2 for 72 h. The culture medium was removed, and the membranes were washed with PBS and fixed with 3.7% (v/v) formaldehyde for 5 min. After PBS rinsing again, the membranes were treated with 50 μg/ml of phalloidin for 40 min at room temperature for cytoplasmic staining. Subsequently, they were washed and treated with 0.1 μg/ml of DAPI for 15 minutes at 37 °C for nuclear staining, followed by another round of PBS washing. Finally, fluorescence images were acquired using a confocal microscope (Leica TCS SP5 II; Wetzlar, Germany).

Statistical Analysis

The experiments had results expressed as mean ± standard deviation. In addition, the one-way analysis of variance (ANOVA) with a Bonferroni post-hoc test was used to compare the samples. The statistical analysis was performed using IBM SPSS Statistics 22.0 software. The results were considered statistically different for $p<0.05$.

RESULTS AND DISCUSSION

Processability of PLGA and PLGA-HA(NPs) membranes

The effective fiber formation for membrane production depends on many parameters, such as solution rheological properties and other process parameters (rotational speed, collector distance, and orifices diameter) [19]. The critical concentration of the solution (C*), i.e., the ratio between solute and solvent, is the first parameter that should be determined to allow solution spinnability [19,20]. The critical concentration is the minimum concentration needed to allow sufficient polymer chain entanglement for fiber formation [19]. The viscosities of different solution concentrations were measured to determine the critical concentration of PLGA and PLGA-HA(NPs) (**Figure 1**).

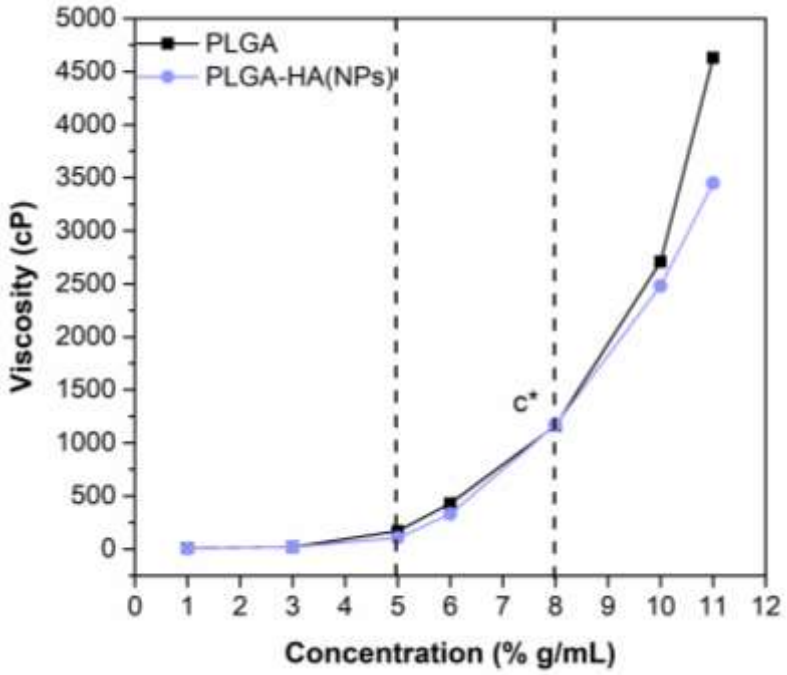

Figure 1. Apparent viscosity versus solution concentration profile for PLGA and PLGA-HA(NPs) solutions and the critical concentration (*C).

The critical concentration is the concentration in which the second change in slope of the apparent viscosity vs. solution concentration curves occurs [20]. The critical concentration obtained and used for membrane production was 8% g/mL for PLGA and PLGA-HA(NPs). Moreover, adding HA(NPs) to PLGA slightly reduced the solution viscosity compared to pure PLGA solutions. This phenomenon was observed in other studies using polylactic acid-based polymers, suggesting that the interactions between the polymer chains and the HA(NPs) surface might reduce the direct interaction of the polymer with the solvent, playing a key role in the viscosity reduction [21].

The rotational speed also directly affects fiber formation. Therefore, the morphology of the membranes was analyzed using SEM (**Figure *2***) to evaluate the effect of different rotational speeds on fiber diameter and morphology.

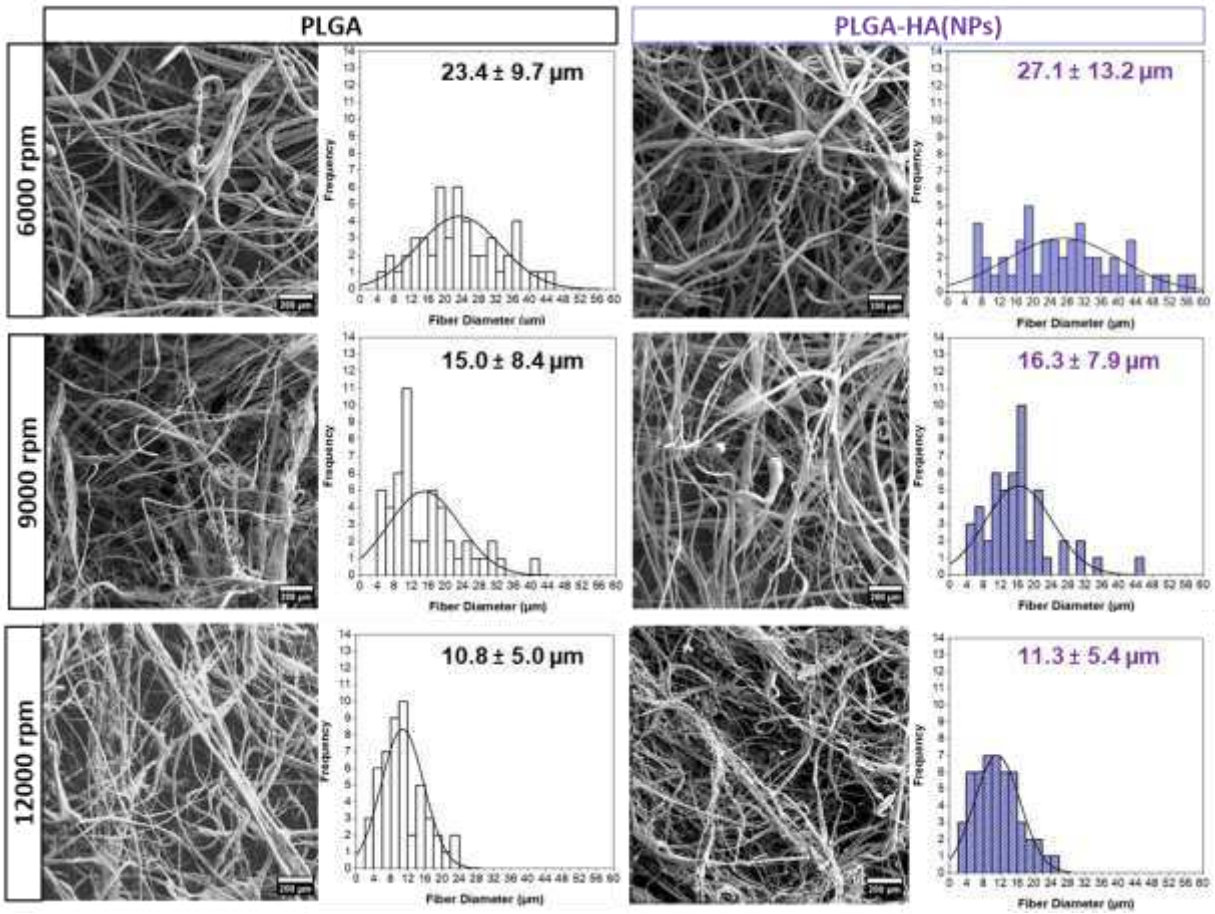

Figure 2. SEM-SE images and fiber diameter distribution of PLGA and PLGA-HA(NPs) membranes produced by RJS at 6000, 9000, and 12000 rpm.

Continuous fibers were obtained for all speeds and scaffolds, with diameters of less than 30 µm. Additionally, there was no formation of beads (spherical structures) in the fibers, which can negatively interact with cells [22]. This indicates no breakage or instability in fiber production throughout the process [23]. Solution characteristics, such as viscosity, polymer, and NP concentration, and process parameters, such as rotation speed, can influence the obtainment of continuous and homogeneous fibers and the diameter size [24]. Accordingly, the fiber diameters reduced and presented lower dispersion as the speed increased. Thus, the rotational speed was set at 12000 rpm for the composite membrane production and subsequent characterizations.

Chemical, morphological, and thermal characterization of scaffolds

After fabricating the membranes, it is essential to characterize their chemical composition to evaluate whether all the expected functional groups and chemical bonds are

present and their application for tissue engineering. Here, FTIR analysis was used to chemically characterize the membranes (Figure 3), revealing the presence of characteristic chemical bonds of PLGA in all spectra. The carbonyl group stretching (C=O) peak was observed at 1746 cm^{-1}, while the peaks ranging from 1000 to 1100 cm^{-1} were associated with the stretching of ester C-O groups of PLGA. Moreover, the bending of methyl C-H groups was represented by the peaks between 1350 and 1450 cm^{-1} [25].

In addition to PLGA, the characteristic chemical bonds of HA nanoparticles were also detected in the PLGA-HA composite membranes. The peaks in the range of 960 to 1100 cm^{-1} indicate the presence of HA's phosphate (PO_4^{3-}) group [26]. Meanwhile, the absence of peaks corresponding to chloroform confirmed the successful evaporation of the solvent during the process [27].

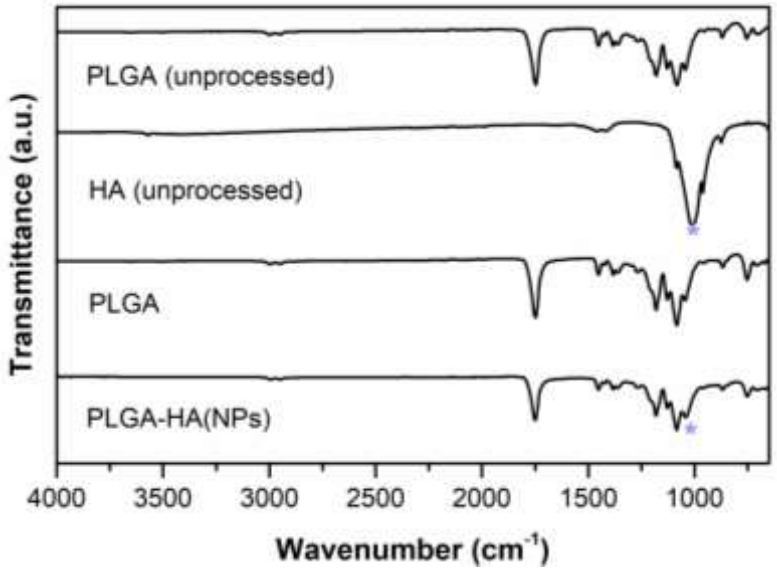

Figure 3. FTIR spectra of unprocessed PLGA and HA compared to PLGA and PLGA-HA(NPs) membranes. * Indicates the HA(NPs) peaks

Although the chemical analyses identified the presence of HA(NPs) in the PLGA-HA(NPs) membrane, it is also crucial to evaluate if the HA nanoparticles were homogenously spread throughout the membrane's fibers. In this study, we investigated the HA distribution in the fibers using EDS (Figure 4) and TEM (Figure 5).

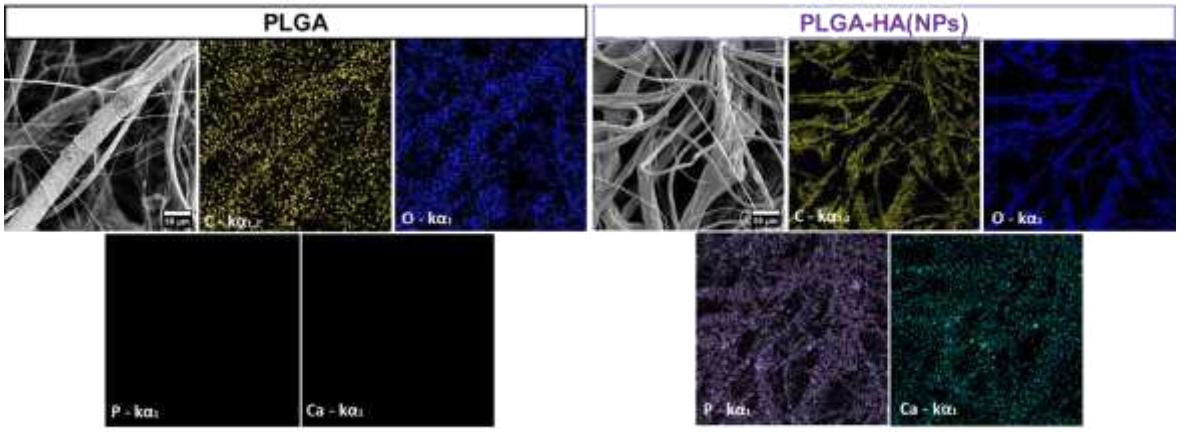

Figure 4. EDS images of PLGA and PLGA-HA(NP)s scaffolds.

EDS is a powerful analytical technique that allows the identification and visualization of elements present in the sample. Here, the results revealed the presence of carbon (C) and oxygen (O) in all membranes, which compose the chemical structure of PLGA. However, it also identified the presence of calcium (Ca) and phosphorus (P) in the PLGA-HA scaffold, which are characteristic elements of the HA(NPs) molecule ($Ca_5(OH)(PO_4)_3$). Thus, the EDS result showed that the HA (represented by its elements) was successfully added to the composite membrane.

Also, with TEM, it was possible to visualize the nanoparticle dispersion inside the fiber with the characteristic spherical HA(NPs) at less than 200 nm (Figure 5). This spread of HA(NP)s can lead to improved bioactivity throughout the fibers in the membrane.

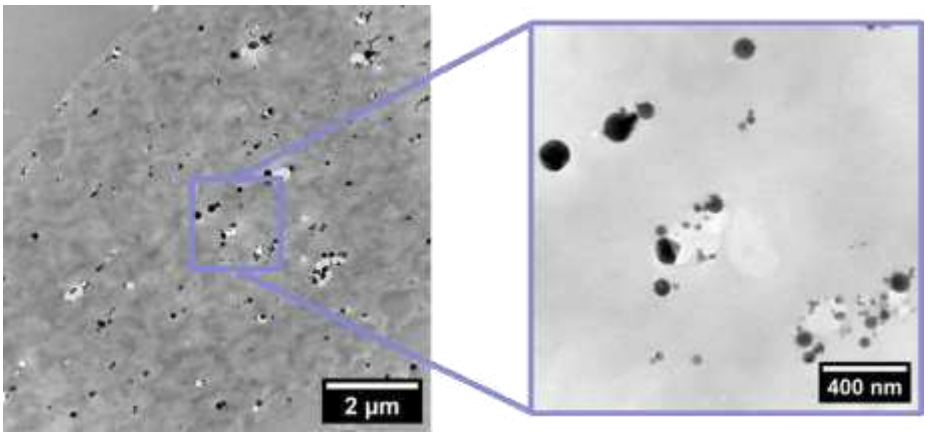

Figure 5. TEM images of a PLGA-HA(NPs) fiber showing the HA(NPs) morphology.

The thermal degradation profile of the scaffolds was evaluated using thermogravimetric analysis (Figure 6). The scaffolds presented an initial mass loss of 2 to 3% around 100 °C due to the evaporation of surface water [28]. In addition to this initial stage, the membranes exhibited a main thermal degradation stage above 300 °C, corresponding to the degradation of the polymer [29].

For the PLGA membrane, a mass loss of 95% occurred in this stage at an onset temperature (T_{onset}: extrapolated initial degradation temperature) of 321 °C, a maximum temperature (T_{max}) of 343 °C, and an end set temperature (T_{endset}: extrapolated final degradation temperature) of 353 °C. In contrast, the membrane with added HA(NPs) presented a T_{onset}= 323 °C, T_{max}= 346 °C, and T_{endset}= 354 °C. The PLGA-HA(NPs) membrane exhibited a mass loss of 88%, a lower mass loss than pure PLGA. As expected, the relative amount of residual mass was approximately the same as the concentration of HA-NPs added to the composite membranes (10% w/w) since HA degrades only at temperatures of approximately 1000 °C [29].

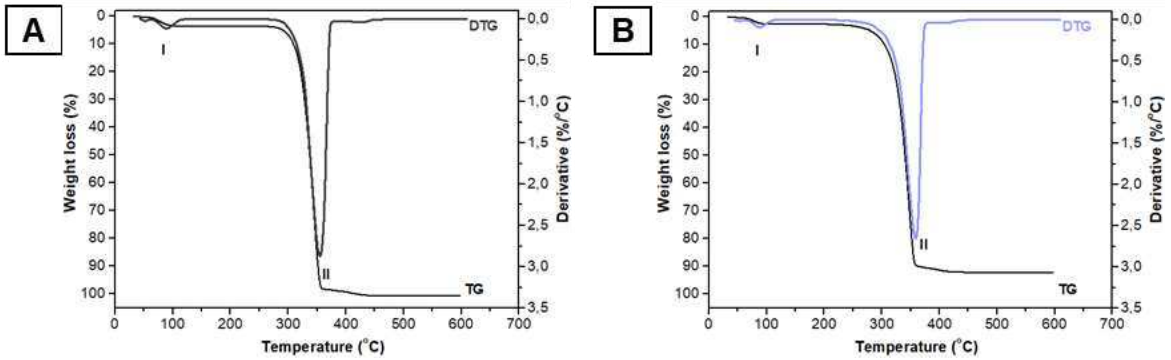

Figure 6. TGA and DTG curves of PLGA (A) and PLGA-HA(NPs) (B) scaffolds.

Bioactivity assessment

The bioactivity related to osteoconductivity of the membranes was evaluated by assessing apatite formation on their surface. Thus, the membranes were incubated in SBF, observed using SEM (Figure 7A-B), and analyzed using XRD (Figure 7C). The SEM images showed that the membrane containing HA(NPs) exhibited the deposition of spherical particles on their surface after SBF incubation, which is characteristic of apatite formation [30]. However, only a few particles were observed on the surface of PLGA membranes.

XRD analysis was used to identify the characteristic peaks of the membranes' crystalline structure, HA(NPs) presence, and apatite formation after SBF incubation (Figure 4). The broad peak characteristic of PLGA [31,32] was identified at a 2θ of approximately

17.3° in all membranes. Meanwhile, the characteristic peaks of the HA(NPs) crystalline structure were identified in the PLGA-HA(NPs) membranes with 2θ values of 10.8° (100), 25.9° (002), 31.8° (211), 32.4° (112), 32.9° (300), 34.0° (202), 39.9° (130), 46.7° (222), and 49.5° (213) [33,34]. The obtained peaks show that HA(NPs) were successfully added and maintained their hexagonal crystalline structure [35]. Moreover, the apatite peaks were better defined after SBF incubation of PLGA-HA(NPs), and no apatite was identified on PLGA membranes after incubation.

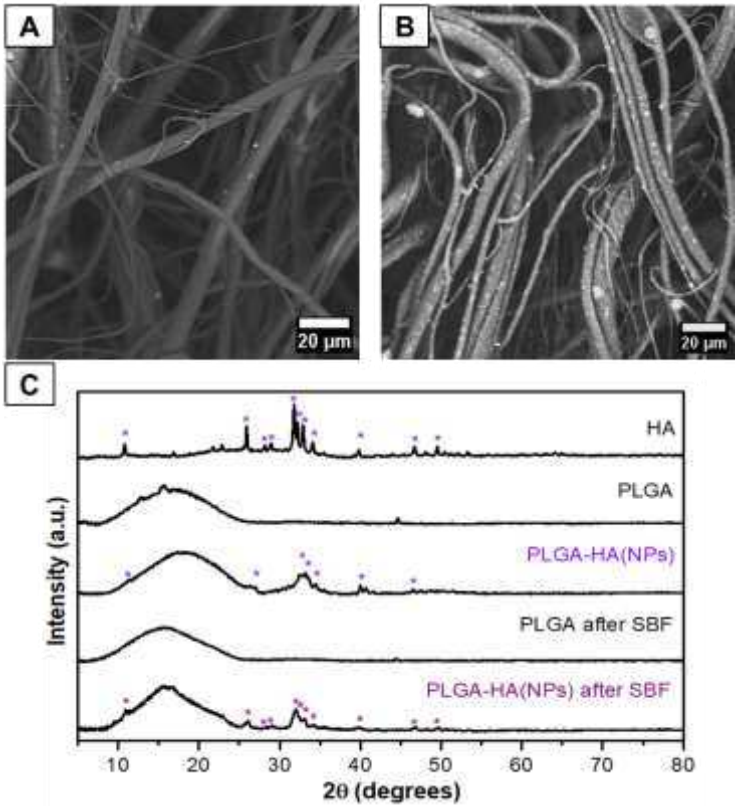

Figure 7. SEM images of (A) PLGA and (B) PLGA-HA(NPs) composite membrane and (C) XRD results before and after four weeks of incubation in SBF. * Indicates HA(NPs)/apatite peaks

The results indicate that PLGA-HA(NPs) membranes present promising bioactivity. This can be attributed to HA(NPs), which provide nucleation sites for apatite crystal formation. The apatite crystals can grow and integrate with the surrounding bone tissue. This is particularly important in treating bone defects and injuries, where the membranes must promote bone regeneration and integration with the surrounding tissue. Therefore, the higher bioactivity of PLGA-HA(NPs) suggests that these membranes have enhanced biological performance and potential bone tissue engineering applications.

Cell viability and adhesion on the PLGA and PLGA-HA(NPs) membranes

According to the results of the MTT assay (as shown in Figure 9A), the cell viability percentage of MC3T3 cells cultured with PLGA and PLGA-HA(NPs) membranes compared to control was 97.1 ± 2.0 % and 96.6 ± 2.8 %, respectively, for 24 h. Thus, there was no significant difference in the cell viability with either PLGA or PLGA-HA(NPs) membrane. However, at 48 h, there was a slight but significant decrease in cell viability in PLGA-HA(NPs) membranes (92.2 ± 4.2 %) compared to PLGA (100.1 ± 4.7 %) and the control (100 ± 4.8 %). This decrease in cell viability for the PLGA-HA(NPs) membrane could be attributed to cell differentiation promoted by HA [36], which is crucial for promoting successful tissue regeneration.

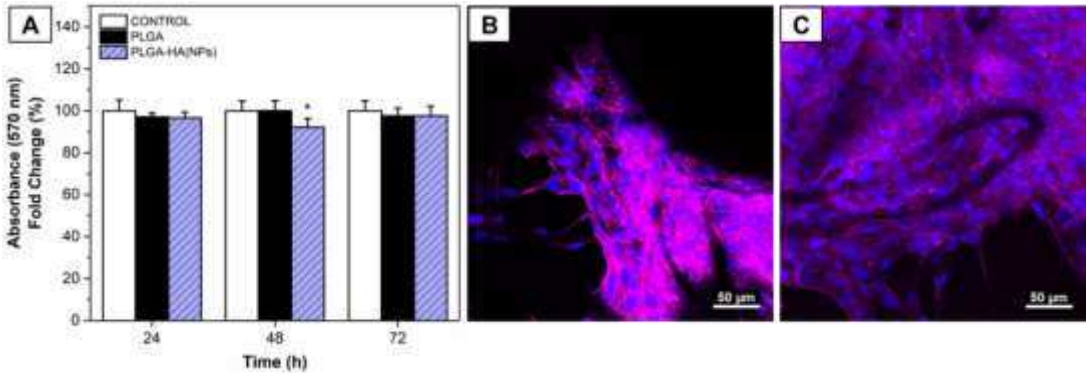

Figure 8. (A) MC3T3 pre-osteoblastic cell viability on PLGA and PLGA-HA(NPs) scaffolds in 24 h, 48 h, and 72 h. Fluorescent images of MC3T3 cells on (B) PLGA and (C) PLGA-HA(NPs) membranes at 72 h. The blue color corresponds to the nuclei and the purple color to the cytoplasm. *p<0.05

Moreover, at 72 h, the cell viability of the PLGA-HA(NPs) increased, having no significant difference (97.6 ± 4.6 %) compared to the PLGA membrane (97.6 ± 3.7 %) and control (100 ± 4.8 %). Confocal microscopy was then used to qualitatively analyze the adhesion and morphology of cells on the membranes at this time (Figure 9B-C). It was possible for both PLGA and PLGA-HA(NPs) membranes to observe cells' confluency with tissue formation. These results suggest that both membranes have great biocompatibility with pre-osteoblastic cells and provide an optimistic view of their potential for bone tissue engineering applications.

Conclusion

This study presents a new and effective method for obtaining osteoconductive PLGA-HA(NPs) composite membranes. Using rotary jet spinning to produce these membranes shows many advantages, including versatility and obtaining scaffolds with controlled fiber morphology. The critical solution concentration and the rotational speed to produce fibers were determined at 8 % g/mL and 12000 rpm, respectively. The presence of HA(NPs) was confirmed qualitatively and quantitatively by chemical, morphological, and thermal degradation analysis. Additionally, the bioactivity of PLGA-HA(NPs) was assessed after SBF incubation by SEM micrographs and XRD patterns, showing apatite formation on the membrane's surface. When cultured with pre-osteoblastic cells, the membranes showed no toxicity, and tissue formation was visualized because of the cell adhesion and proliferation on the membrane surface. The bioactivity and cytocompatibility of the PLGA-HA(NPs) membrane make it a promising alternative for bone regeneration therapy. These findings contribute to developing innovative strategies for bone tissue engineering, and the resulting membranes have the potential for use in a wide range of bone-related applications.

Acknowledgments

We would like to thank the financial support provided for this research by the São Paulo Research Foundation (FAPESP), grant #2020/07923-0; # 2020/14679-9; and the National Council for Scientific and Technological Development (CNPq), grant #140997/2020-2. This research was also supported by TI's Open Labs - Multiple Users and Shared Facilities, CTI Renato Archer, research institution.

References

[1] Chau, A. M. T.; Xu, L. L.; Wong, J. H.-Y.; Mobbs, R. J.: Current status of bone graft options for anterior interbody fusion of the cervical and lumbar spine. Neurosurgical Review, **37**, 23–37 (2014). http://doi:10.1007/s10143-013-0483-9.

[2] Zadegan, S. A.; Abedi, A.; Jazayeri, S. B.; Bonaki, H. N.; Vaccaro, A. R.; Rahimi-Movaghar, V.: Clinical application of ceramics in anterior cervical discectomy and fusion: A review and update. Global Spine Journal, **7**, 343–349 (2017). http://doi:10.1177/2192568217699201.

[3] Ratha, I.; Datta, P.; Balla, V. K.; Nandi, S. K.; Kundu, B.: Effect of doping in hydroxyapatite as coating material on biomedical implants by plasma spraying method: A review. Ceramics International, **47**, 4426–4445 (2021). http://doi:10.1016/J.CERAMINT.2020.10.112.

[4] Javid-Naderi, M. J.; Behravan, J.; Karimi-Hajishohreh, N.; Toosi, S.: Synthetic polymers as bone engineering scaffold. Polymers for Advanced Technologies, **34**, 2083–2096 (2023). http://doi:10.1002/PAT.6046.
[5] Gentile, P.; Chiono, V.; Carmagnola, I.; Hatton, P. V.: An overview of poly(lactic-co-glycolic) Acid (PLGA)-based biomaterials for bone tissue engineering. International Journal of Molecular Sciences, **15**, 3640–3659 (2014). http://doi:10.3390/ijms15033640.
[6] Mahar, R.; Chakraborty, A.; Nainwal, N.; Bahuguna, R.; Sajwan, M.; Jakhmola, V.: Application of PLGA as a Biodegradable and Biocompatible Polymer for Pulmonary Delivery of Drugs. AAPS PharmSciTech, **24**, 1–20 (2023). http://doi:10.1208/S12249-023-02502-1/TABLES/6.
[7] Ansary, R. H.; Awang, M. B.; Rahman, M. M.: Biodegradable poly(D,L-lactic-co-glycolic acid)-based micro/nanoparticles for sustained release of protein drugs - A review. Tropical Journal of Pharmaceutical Research, **13**, 1179–1190 (2014). http://doi:10.4314/tjpr.v13i7.24.
[8] DeFrates, K. G.; Moore, R.; Borgesi, J.; Lin, G. W.; Mulderig, T.; Beachley, V.; Hu, X.: Protein-Based Fiber Materials in Medicine: A Review. Nanomaterials, **8**, 26 (2018). http://doi:10.3390/nano8070457.
[9] Vasconcellos, L. M. R.; Santana-Melo, G. F.; Silva, E.; Pereira, V. F.; Araújo, J. C. R.; Silva, A. D. R.; Furtado, A. S. A.; Elias, C. de M. V.; Viana, B. C.; Marciano, F. R.; Lobo, A. O.: Electrospun Poly(butylene-adipate-co-terephthalate)/Nano-hyDroxyapatite/Graphene Nanoribbon Scaffolds Improved the In Vivo Osteogenesis of the Neoformed Bone. Journal of Functional Biomaterials 2021, Vol. 12, Page 11, **12**, 11 (2021). http://doi:10.3390/JFB12010011.
[10] Sebastian, T.; Preisker, T. R.; Gorjan, L.; Graule, T.; Aneziris, C. G.; Clemens, F. J.: Synthesis of hydroxyapatite fibers using electrospinning: A study of phase evolution based on polymer matrix. Journal of the European Ceramic Society, **40**, 2489–2496 (2020). http://doi:10.1016/J.JEURCERAMSOC.2020.01.070.
[11] Sathiyavimal, S.; Vasantharaj, S.; LewisOscar, F.; Selvaraj, R.; Brindhadevi, K.; Pugazhendhi, A.: Natural organic and inorganic–hydroxyapatite biopolymer composite for biomedical applications. Progress in Organic Coatings, **147**, 105858 (2020). http://doi:10.1016/J.PORGCOAT.2020.105858.
[12] Rodrigues, I. C. P.; Woigt, L. F.; Pereira, K. D.; Luchessi, A. D.; Lopes, É. S. N.; Webster, T. J.; Gabriel, L. P.: Low-cost hybrid scaffolds based on polyurethane and gelatin. Journal of Materials Research and Technology, **9**, 7777–7785 (2020). http://doi:https://doi.org/10.1016/j.jmrt.2020.04.049.
[13] Loordhuswamy, A.; Thinakaran, S.; Venkateshwapuram Rangaswamy, G. D.: Centrifugal spun osteoconductive ultrafine fibrous mat as a scaffold for bone regeneration. Journal of Drug Delivery Science and Technology, **60** (2020). http://doi:10.1016/j.jddst.2020.101978.
[14] Vasconcellos, L. M. R.; Elias, C. M. V; Minhoto, G. B.; Abdala, J. M. A.; Andrade, T. M.; de Araujo, J. C. R.; Gusmão, S. B. S.; Viana, B. C.; Marciano, F. R.; Lobo, A. O.: Rotary-jet spun polycaprolactone/nano-hydroxyapatite scaffolds modified by simulated body fluid influenced the flexural mode of the neoformed bone. Journal of Materials Science: Materials in Medicine, **31** (2020). http://doi:10.1007/s10856-020-06403-8.
[15] Andrade, T. M.; Mello, D. C. R.; Elias, C. M. V; Abdala, J. M. A.; Silva, E.; Vasconcellos, L. M. R.; Tim, C. R.; Marciano, F. R.; Lobo, A. O.: In vitro and in vivo evaluation of rotary-jet-spun poly(ε-caprolactone) with high loading of nano-hydroxyapatite. Journal of Materials Science: Materials in Medicine, **30** (2019). http://doi:10.1007/s10856-019-6222-1.

[16] Mendonça, L. H. P.; Lopes, É. S. N.; Rodrigues, I. C. P.; De Oliveira, M. F.; Gabriel, L. P.: Nanohydroxyapatite effects on polyesters-based membranes for bone applications. Journal of Materials Research and Technology, **20**, 3697–3704 (2022). http://doi:10.1016/J.JMRT.2022.08.066.
[17] Ghannadian, P.; Moxley, J. W.; MacHado De Paula, M. M.; Lobo, A. O.; Webster, T. J.: Micro-Nanofibrillar Polycaprolactone Scaffolds as Translatable Osteoconductive Grafts for the Treatment of Musculoskeletal Defects without Infection. ACS Applied Bio Materials, **1**, 1566–1578 (2018). http://doi:10.1021/acsabm.8b00453.
[18] Pereira Rodrigues, I. C.; Tamborlin, L.; Rodrigues, A. A.; Jardini, A. L.; Ducati Luchessi, A.; Maciel Filho, R.; Najar Lopes, É. S.; Pellizzer Gabriel, L.: Polyurethane fibrous membranes tailored by rotary jet spinning for tissue engineering applications. Journal of Applied Polymer Science, **137** (2020). http://doi:10.1002/app.48455.
[19] Rogalski, J. J.; Botto, L.; Bastiaansen, C. W. M.; Peijs, T.: A study of rheological limitations in rotary jet spinning of polymer nanofibers through modeling and experimentation. Journal of Applied Polymer Science, **137**, 48963 (2020). http://doi:10.1002/APP.48963.
[20] Pan, W.; Lin, J.: Efficient centrifugal spinning of soda lignin for the production of activated carbon nanofibers with highly porous structure. International Journal of Biological Macromolecules, **222**, 1433–1442 (2022). http://doi:10.1016/J.IJBIOMAC.2022.09.268.
[21] Padilla-Gainza, V. M.; Rodríguez-Tobías, H.; Morales, G.; Saucedo-Salazar, E.; Lozano, K.; Montaño-Machado, V.; Mantovani, D.: Centrifugally spun mats based on biopolyesters/hydroxyapatite and their potential as bone scaffolds. Journal of Applied Polymer Science, **138**, app50139 (2021). http://doi:10.1002/APP.50139.
[22] Karaman, O.; Şen, M.; Demirci, E. A.: Electrospun scaffolds for vascular tissue engineering. In *Electrospun Materials for Tissue Engineering and Biomedical Applications: Research, Design and Commercialization*; Elsevier Inc., (2017); pp. 261–287 ISBN 9780081022221 (ISBN); 9780081010228 (ISBN).
[23] Krifa, M.; Hammami, M. A.; Wu, H.: Occurrence and morphology of bead-on-string structures in centrifugal forcespun PA6 fibers. The Journal of The Textile Institute, **106**, 284–294 (2015). http://doi:10.1080/00405000.2014.917812.
[24] Ren, L.; Pandit, V.; Elkin, J.; Denman, T.; Cooper, J. A.; Kotha, S. P.: Large-scale and highly efficient synthesis of micro- and nano-fibers with controlled fiber morphology by centrifugal jet spinning for tissue regeneration. Nanoscale, **5**, 2337–2345 (2013). http://doi:10.1039/C3NR33423F.
[25] dos Santos, T. M. B. K.; Merlini, C.; Aragones, Á.; Fredel, M. C.: Manufacturing and characterization of plates for fracture fixation of bone with biocomposites of poly (lactic acid-co-glycolic acid) (PLGA) with calcium phosphates bioceramics. Materials Science and Engineering: C, **103**, 109728 (2019). http://doi:10.1016/J.MSEC.2019.05.013.
[26] Krok-Borkowicz, M.; Reczyńska, K.; Rumian, Ł.; Menaszek, E.; Orzelski, M.; Malisz, P.; Silmanowicz, P.; Dobrzyński, P.; Pamuła, E.: Surface-Modified Poly(l-lactide-co-glycolide) Scaffolds for the Treatment of Osteochondral Critical Size Defects—In Vivo Studies on Rabbits. International Journal of Molecular Sciences 2020, Vol. 21, Page 7541, **21**, 7541 (2020). http://doi:10.3390/IJMS21207541.
[27] Rodrigues, I. C. P.; Tamborlin, L.; Rodrigues, A. A.; Jardini, A. L.; Luchessi, A. D.; Maciel Filho, R.; Lopes, É. S. N.; Gabriel, L. P.: Polyurethane fibrous membranes tailored by rotary jet spinning for tissue engineering applications. Journal of Applied Polymer Science, **137**, 1–10 (2020). http://doi:10.1002/app.48455.
[28] Yu, Y.; Kong, L.; Li, L.; Li, N.; Yan, P.: Antitumor Activity of Doxorubicin-Loaded Carbon Nanotubes Incorporated Poly(Lactic-Co-Glycolic Acid) Electrospun Composite

Nanofibers. Nanoscale Research Letters, **10**, 1–9 (2015). http://doi:10.1186/S11671-015-1044-7/FIGURES/8.
[29] Wang, T.; Dorner-Reisel, A.; Müller, E.: Thermogravimetric and thermokinetic investigation of the dehydroxylation of a hydroxyapatite powder. Journal of the European Ceramic Society, **24**, 693–698 (2004). http://doi:10.1016/S0955-2219(03)00248-6.
[30] Kranthi Kiran, A. S.; Kizhakeyil, A.; Ramalingam, R.; Verma, N. K.; Lakshminarayanan, R.; Kumar, T. S. S.; Doble, M.; Ramakrishna, S.: Drug loaded electrospun polymer/ceramic composite nanofibrous coatings on titanium for implant related infections. Ceramics International, **45**, 18710–18720 (2019). http://doi:10.1016/J.CERAMINT.2019.06.097.
[31] Manjit, M.; Kumar, M.; Jha, A.; Bharti, K.; Kumar, K.; Tiwari, P.; Tilak, R.; Singh, V.; Koch, B.; Mishra, B.: Formulation and characterization of polyvinyl alcohol/chitosan composite nanofiber co-loaded with silver nanoparticle & luliconazole encapsulated poly lactic-co-glycolic acid nanoparticle for treatment of diabetic foot ulcer. International Journal of Biological Macromolecules, **258**, 128978 (2024). http://doi:10.1016/J.IJBIOMAC.2023.128978.
[32] dos Santos, V. I.; Merlini, C.; Aragones, Á.; Cesca, K.; Fredel, M. C.: Influence of calcium phosphates incorporation into poly(lactic-co-glycolic acid) electrospun membranes for guided bone regeneration. Polymer Degradation and Stability, **179**, 109253 (2020). http://doi:10.1016/J.POLYMDEGRADSTAB.2020.109253.
[33] Wei, J.; Yan, Y.; Gao, J.; Li, Y.; Wang, R.; Wang, J.; Zou, Q.; Zuo, Y.; Zhu, M.; Li, J.: 3D-printed hydroxyapatite microspheres reinforced PLGA scaffolds for bone regeneration. Biomaterials Advances, **133**, 112618 (2022). http://doi:10.1016/J.MSEC.2021.112618.
[34] Li, G.; Qin, S.; Zhang, D.; Liu, X.: Preparation of antibacterial degummed silk fiber/nano-hydroxyapatite/polylactic acid composite scaffold by degummed silk fiber loaded silver nanoparticles. Nanotechnology, **30**, 295101 (2019). http://doi:10.1088/1361-6528/AB13DF.
[35] Haider, A.; Gupta, K. C.; Kang, I. K.: PLGA/nHA hybrid nanofiber scaffold as a nanocargo carrier of insulin for accelerating bone tissue regeneration. Nanoscale Research Letters, **9**, 1–12 (2014). http://doi:10.1186/1556-276X-9-314/FIGURES/11.
[36] Shu, R.; McMullen, R.; Baumann, M. J.; McCabe, L. R.: Hydroxyapatite accelerates differentiation and suppresses growth of MC3T3-E1 osteoblasts. Journal of Biomedical Materials Research Part A, **67A**, 1196–1204 (2003). http://doi:10.1002/JBM.A.20021.

6.2. Manuscrito do Artigo 2

Implants promoting osteoconduction and local antibacterial activity for effective osseointegration and osteomyelitis prevention

Isabella Caroline Pereira Rodrigues[1], Karina Danielle Pereira[2,3], Augusto D. Luchessi[2,3], Laís Pellizzer Gabriel[1,2], Éder Sócrates Najar Lopes[1*]

[1] School of Mechanical Engineering, University of Campinas, Campinas, São Paulo, Brazil
[2] School of Applied Sciences, University of Campinas, Limeira, São Paulo, Brazil
[3] Institute of Biosciences, São Paulo State University, Rio Claro, São Paulo, Brazil
* Correspondence to: Éder Sócrates Najar Lopes (E-mail esnlopes@unicamp.br; Telephone: +55 (19) 3521-0017; Street address: Rua Mendeley, 200, Campinas 13083-860, SP, Brazil)

ABSTRACT

Bone implants have a high risk of failure due to insufficient osseointegration, incompatible mechanical properties, and the occurrence of osteomyelitis. In this study, pharmacological and osteoconductive scaffolds and metallic implants were developed using rotary jet spinning (RJS) and additive manufacturing (AM) techniques. Poly(lactic-co-glycolic acid) scaffolds with nanohydroxyapatite (nHA), were successfully produced containing collagen (COL) and rifampicin (RIF), exhibiting homogeneous fibers. Chemical, thermal, and structural analysis confirmed the presence of nHA, COL, and RIF in the scaffolds. The scaffolds showed a hydrophobic nature and consequent low degradation, except for the scaffold containing COL. The release profile of RIF followed controlled release kinetic models. The release of RIF by the scaffold and mettalic implant was sufficient to inhibit *Staphylococcus aureus*, the main cause of osteomyelitis. Ti6Al4V alloy implants were successfully produced for bone requirements using AM. Lastly, the scaffolds and implants exhibited osteoconduction and high cell proliferation, adhesion, and viability, being promising alternatives for local antibacterial activity and improved osseointegration for bone regeneration.

Keywords: Antibiotics; Bacteria; Ceramics; Centrifugal Spinning; Drug Delivery; Electron Beam Melting; Fiber; Hydroxyapatite; Membrane; Nanoparticles

INTRODUCTION

Incomplete osseointegration, bone infections known as osteomyelitis, and mechanical failure or "stress shielding" are persistent problems of implants, often leading to revision surgeries [1,2]. These problems are a global health concern as they cause a social and economic burden, requiring more surgeries and reducing quality of life [3,4].

Bone grafts, especially autogenous ones, are still the most commonly used technique to restore bone function [5]. However, these grafts have volume limitations, involve multiple surgical procedures, and can have associated complications, such as infections and immune responses [6]. Thus, new implants are being studied to overcome these disadvantages and promote better bone regeneration. Some metallic, polymeric, and ceramic biomaterials can be used to produce implants and scaffolds containing cells or other additives (e.g., antibiotics and bioactive particles) for bone applications [7].

Titanium (Ti) alloys, mainly Ti6Al4V, are widely used as structural support for bone implants due to their excellent mechanical strength and biocompatibility [1]. Although the stiffness of Ti alloys may be associated with higher subsidence [8,9], implant improvements can be achieved using additive manufacturing techniques (AM). These techniques allow porous structure fabrication through the customization of complex designs, helping to reduce implant stiffness.

Combining AM-designed Ti6Al4V implants with osteoconductive scaffolds containing bioactive additives, like hydroxyapatite (HA) and type I collagen (COL), can enhance implant osseointegration with bone. HA and COL are interesting additives as they mimic the inorganic and organic components of bone extracellular matrix, respectively. HA is a bioresorbable ceramic with biocompatibility and osseointegration results that are as good as – or even better than – autografts [10]. Moreover, HA nanoparticles (nHA) have shown improved results compared to other particle sizes because of their higher surface area and bioactivity [11]. The combination of HA with COL also shows promising results, with better bone regeneration when compared to COL sponges *in vivo* [12]. However, COL and other natural polymers present drawbacks like high cost and limited processability [13].

Synthetic polymers, such as poly(lactic-co-glycolic acid) (PLGA) and polycaprolactone, can be used to improve the mechanical properties and processability of the aforementioned additives. PLGA is commonly used for drug delivery and bone

applications, acting as a matrix for additive incorporation, because of its bioresorbability and biocompatibility [14]. Antibiotics, such as rifampicin (RIF), are some additives that can be incorporated into PLGA for antibacterial activity during bone regeneration [15]. RIF and other antibiotics are usually administered orally in very high dosages and low effectiveness to prevent osteomyelitis [16]. Therefore, local antibiotic delivery using PLGA-based systems may be more efficient, requiring lower antibiotic concentrations.

It is important to use a technique capable of processing the polymers and additives, maintaining their functionality to produce such polymeric scaffolds with osteoconductive and antibacterial properties. Rotary Jet Spinning (RJS) is a groundbreaking technique that can fulfill this need. RJS is highly scalable to produce fibrous scaffolds, without requiring high temperatures or electric fields, which can inactivate some materials, such as COL [17].

It is imperative to pursue new implants that are more effective, allowing for better osseointegration, mechanical compatibility, and local bacterial prevention. Despite the focus of some studies on osteoconductive antibacterial scaffolds, there is still much to be explored for an ideal implant [18,19]. Therefore, this study shows a novel combination of processing techniques, materials, and analyses reaching for the "holy grail" in bone regeneration. Thus, porous implants of AM Ti6Al4V were combined with RJS scaffolds of PLGA-HA-RIF and PLGA-COL-HA (**Figure 1**) to obtain bone implants with osteoconductive properties and bacterial infection prevention for bone applications.

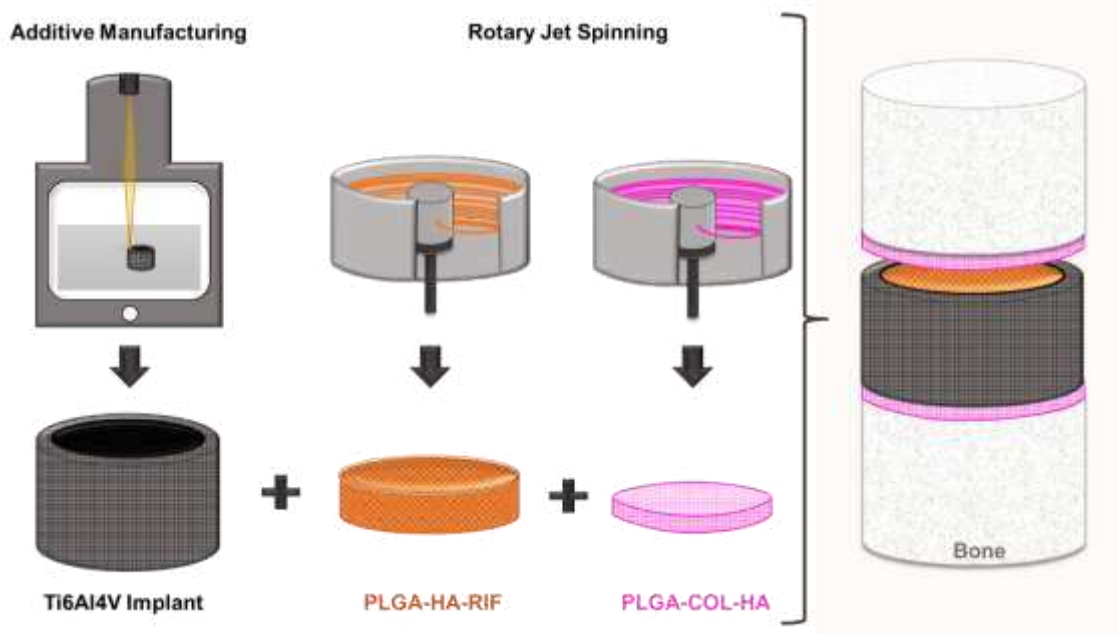

Figure 1. Implant and Scaffolds Schematic

MATERIALS AND METHODS

AM Structure Design and Fabrication

The metallic structure models for this study were designed from body-centered cubic (BCC) unit cells using the nTopology software (nTopology Inc., NY, USA). Tubular structures with dimensions of 6 mm in external diameter, 3 mm in internal diameter, and 9 mm or 3 mm in length, and different pore sizes (300, 450, and 600 μm) were fabricated. The AM structures were manufactured using Electron Beam Powder Bed Fusion (PBF-EB) technology with the EBM Arcam Model Q10 (Arcam EBM, GE Additive Company). A Ti6Al4V alloy powder (Spectra H Ti6Al4V Grade 5, supplied by Ge Additive Company) was used to produce the structures. The platform was pre-heated to 495 °C at a working atmosphere of $1x10^{-3}$ mbar of helium and high vacuum, hatch distance and depth of 0.2 mm and 0.05mm, respectively, a scan speed of 4530 mm/s with a focus offset of 36 mA and a layer thickness of 50 μm was employed in the process.

Scaffold Preparation and Processing

To prepare the polymeric solutions, PLGA (Resomer® LG 824S, Evonik Brasil LTDA.) was solubilized in chloroform, for PLGA-HA and PLGA-HA-RIF, and hexafluoroisopropanol (HFIP; #105228), for PLGA-COL-HA. The nHA (#677418, with particle size <200 nm) was incorporated at a concentration of 20% w/w using a magnetic stirrer. For PLGA-HA-RIF and PLGA-COL-HA, 5% w/w of RIF (#R3501) and a 1:3 ratio of COL (type I collagen; #C9879) were also added to the relative mass concentration, respectively. All solvents and additives were sourced from Sigma-Aldrich LTDA. (Brazil). Scaffolds were fabricated using the RJS equipment described in previous studies from our group [20] at a rotational speed of 12,000 rpm.

Microstructural Characterization of Scaffolds

Morphological characterization of the bioresorbable scaffolds was conducted using Scanning Electron Microscopy (SEM), employing a ZEISS EVO® MA 15 microscope at an operating voltage of 10 kV. The scaffolds were gold-coated prior to SEM analysis, using a Quorum SC7620 sputter coater. The diameter of 50 fibers from each scaffold were determined using ImageJ software. The morphology of nHA and RIF particles was analyzed using Transmission Electron Microscopy (TEM). Micrographs were acquired with the JEOL Transmission Electron Microscope JEM-1400 (Tokyo, Japan) operating at an accelerating voltage of 120 kV.

Chemical and Thermal Analysis of the Scaffolds

The chemical composition of scaffolds and their unprocessed polymers and additives was characterized by Fourier Transform Infrared Spectroscopy (FTIR) employing a PerkinElmer Spectrum 100 equipped with an attenuated total reflectance (ATR) infrared spectrometer. his analysis covered a wavelength range from 650 to 4000 cm^{-1}, with 16 scans performed at a resolution of 4 cm^{-1}. The scaffolds' thermal properties were assessed through thermogravimetric analysis (TGA) conducted on a 2950 thermogravimetric analyzer (TA Instruments, USA). Samples weighing approximately 5 mg were examined under an inert argon atmosphere at a flow rate of 60 mL/min. The analysis was performed at a heating rate of 10 °C/min from 25 °C to 600 °C.

Wettability and *in vitro* degradation of Scaffolds

The hydrophilicity of the scaffolds was evaluated through a contact angle assay in accordance with ASTM D7334 standards. Static contact angles were measured using the Dataphysics model OCA15 equipment. Four replicates of angles between the droplet and scaffolds' surface were obtained using ImageJ software. Hydrolytic degradation of the scaffolds was assessed *in vitro* according to ASTM F1635-11. The scaffolds were initially weighed and then immersed in PBS with a pH of 7.4 and maintained at a temperature of 37 °C. After specific time intervals (30, 60, and 90 days), the samples were retrieved from the solution, dried, and reweighed to assess changes in weight over time.

Drug Encapsulation and Release Studies

RIF's encapsulation and release analysis was conducted using ultraviolet-visible (UV-Vis) spectroscopy at a wavelength of 483 nm with the FilterMax F5 Multimode equipment. First, the drug encapsulation efficiency, related to incorporating RIF into PLGA's matrix, was determined by dissolving the PLGA-HA-RIF scaffolds in 5 mL of chloroform through ultrasonic agitation and subsequent centrifugation for 5 minutes. Scaffolds weighing approximately 10 mg were incubated in 10 mL of PBS (pH 7.4) at 37 °C and 100 rpm. The release was measured from 0 to 720 hours, with 4 mL of the solution withdrawn at specific time intervals for spectrometry analysis. The withdrawn volume was replaced with an equivalent volume of fresh PBS. The experiments were carried out with four replicates. The release investigation was additionally evaluated by employing various kinetic models, including zero-order, first-order, Higuchi, Hixson-Crowell, Korsmeyer-Peppas, and Weibull.

Mechanical Tests, Density, and Porosity Measurements of Implants

The mechanical properties of the Ti6Al4V structures were evaluated through compression testing according to ASTM E9-19. Compression tests were performed using a universal testing machine (WDW-100E) with a 100kN load cell and a speed of 1 mm/min. The stiffness was calculated as the slope of the linear portion of the stress-strain curves obtained. The density and porosity of the Ti6Al4V structures were assessed using a helium gas pycnometer (Micromeritics AccuPyc 1330) after ultrasonic cleaning with ethanol and drying. Moreover, SEM images were analyzed, and the dimensions of 5 pores from the Ti6Al4V structures were measured using ImageJ. For the tests, four tubular specimens for each pore size were used, all having a height of 9 mm, an external diameter of 6 mm, and an internal diameter of 3 mm.

Disk Diffusion Test and Osteoconductive Assessment

Antibacterial activity was evaluated by a disk diffusion test according to the NCCLS M02-A8 standard. For the assay, gram-positive (*Staphylococcus aureus*, ATCC 6538) and gram-negative (*Escherichia coli*, K-12 strain) bacteria were inoculated in LB medium until reaching an optical turbidity of 0.5 and then incubated on agar plates. Scaffold and Ti6Al4V implants containing 7 μg of PLGA-HA-RIF were added to the agar plates to assess the zone of inhibition. The halo diameters were measured using ImageJ. The PLGA-HA scaffold and Ti6Al4V structures were used as a control to compare with PLGA-HA-RIF and Ti6Al4V implants containing PLGA-HA-RIF scaffold.

Osteoconduction was assessed through the in vitro formation of apatite on the implant using simulated body fluid (SBF), as per the ABNT NBR ISO 23317:2017 standard. For the experiment, scaffold samples were cut into 15 mm squares and immersed in 40 mL of SBF solution at a temperature of 37 °C. After four weeks, the samples were removed, rinsed with distilled water, and dried. Apatite formation on the scaffold surfaces was detected using SEM. Additionally, Energy Dispersive X-ray Spectroscopy (EDS), integrated into the SEM microscope, was utilized for elemental composition analysis of the scaffolds after apatite formation.

Cell Viability and Morphology Analysis

Cell viability of the MC3T3-E1 mouse preosteoblast cells with the scaffolds and implants was evaluated using a modified 3-(4,5-dimethylthiazol-2-yl)-2,5-diphenyltetrazolium bromide (MTT) assay. The cells were cultured in α-MEM supplemented with 10% FBS, 100 U/mL penicillin, and 100 μg/mL streptomycin (Life Technologies, Inc.)

in a 5% CO_2 humidified atmosphere at 37 °C. Upon reaching 80% confluence, they were trypsinized, neutralized, and counted using a Countess II automatic counter. The scaffolds and implants were seeded with cells in a 48-well plate and sterilized with UV light overnight. After incubation for 24, 48, and 72 h in a culture medium, MTT solution (0.5 mg/mL in PBS) was added to the cells, followed by a 3 h incubation. The metabolic activity of the cells was measured by absorbance at 570 nm using a scanning spectrophotometric multiwell plate reader (F5 Microplate Reader, Molecular Probes). Control cells were included in a separate 48-well plate for comparison. To analyze cell morphology and adhesion, MC3T3-E1 cells were cultured on the scaffolds for 72 h, fixed with 3.7% formaldehyde, and stained with phalloidin and DAPI for cytoplasmic and nuclear visualization, respectively. Fluorescence images of the cell-seeded scaffolds and implants were captured using a confocal microscope (Leica TCS SP5 II).

Statistical Analysis

The results of the experiments were presented as the mean ± standard deviation. Furthermore, for sample comparison, one-way ANOVA (analysis of variance) with a Bonferroni post-hoc analysis was utilized. Statistical evaluations were conducted using IBM SPSS Statistics 22.0. A p-value of less than 0.05 was considered indicative of statistically significant differences.

RESULTS AND DISCUSSION

Scaffolds morphology

The morphology of the fibrous scaffolds was assessed using SEM (**Figure 2**). Homogeneous fibers with diameters of less than 20 µm were obtained for all produced scaffolds. There was no significant difference in fiber diameters between PLGA-HA (14.0 ± 6.8 µm) and PLGA-HA-RIF (12.7 ± 8.0 µm) scaffolds, showing that RIF addition did not change fiber morphology. However, for PLGA-COL-HA (3.6 ± 2.2 µm) scaffolds, the fiber diameter was reduced by almost 75% compared to PLGA-HA. Other studies also showed this effect on fiber diameter reduction after protein addition [21]. Moreover, no beads were formed due to fiber rupture throughout the process [22]. It is known that solution characteristics and process parameters can influence fiber formation [23], so the parameters chosen were able to produce the scaffolds with homogenous fibers effectively.

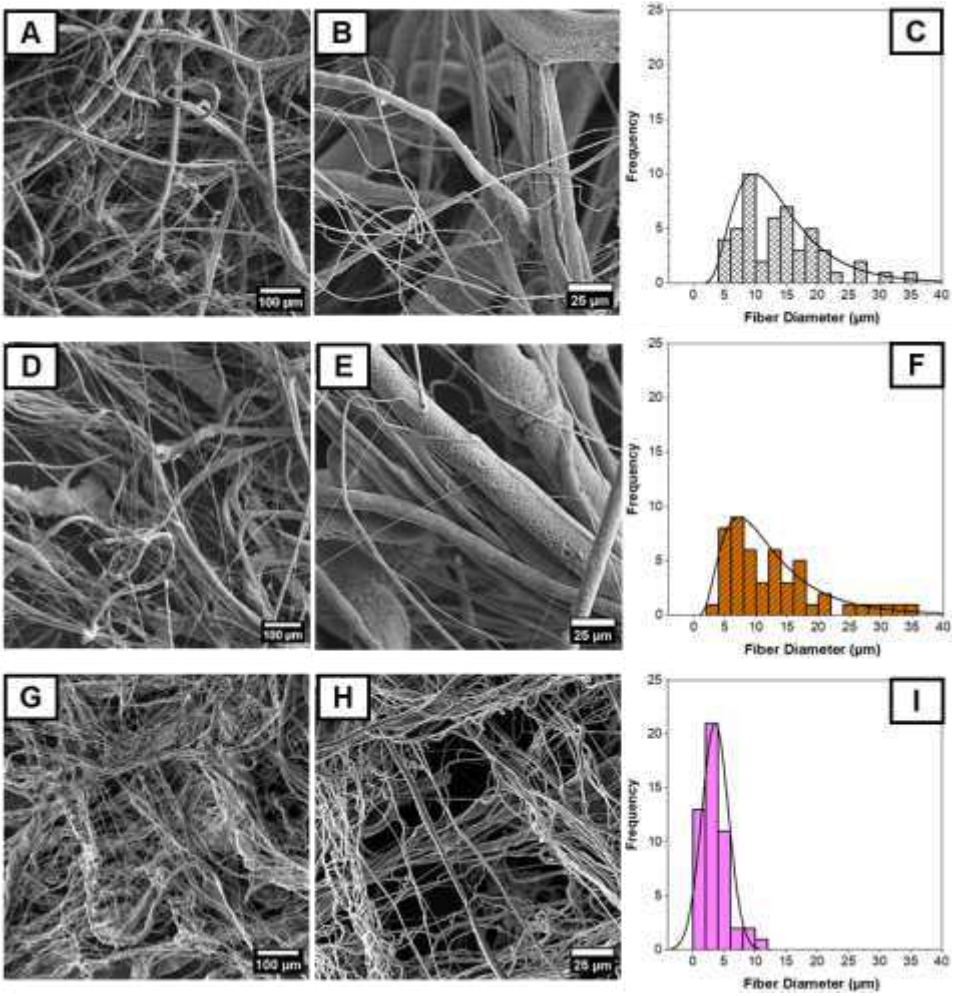

Figure 2. SEM images and histograms of (A-C) PLGA-HA, (D-F) PLGA-HA-RIF, and (G-I) PLGA- HA-COL

The TEM analysis revealed that nHAs were uniformly distributed throughout the fibers in all scaffolds (Figure 3). This distribution suggests the effective incorporation of nHA within the fiber, which is crucial for enhancing the scaffolds' osteoconductive properties. Furthermore, for the PLGA-HA-RIF scaffold, in addition to nHA, the presence of RIF was also identified. While nHA exhibited a spherical morphology, consistent with previous observations [24,25], RIF particles appeared smooth and rod-like [26], contrasting with the nHA morphology and energy. Overall, the TEM analysis suggests that nHA and RIF are effectively incorporated within the scaffold fibers. Incorporating HA and RIF within the polymer matrix of the fibers is advantageous for controlled release applications, as it protects against degradation or loss of bioactivity. Moreover, this internal distribution ensures that the nanoparticles are uniformly dispersed throughout the scaffold, potentially enhancing their biological performance for bone tissue engineering applications.

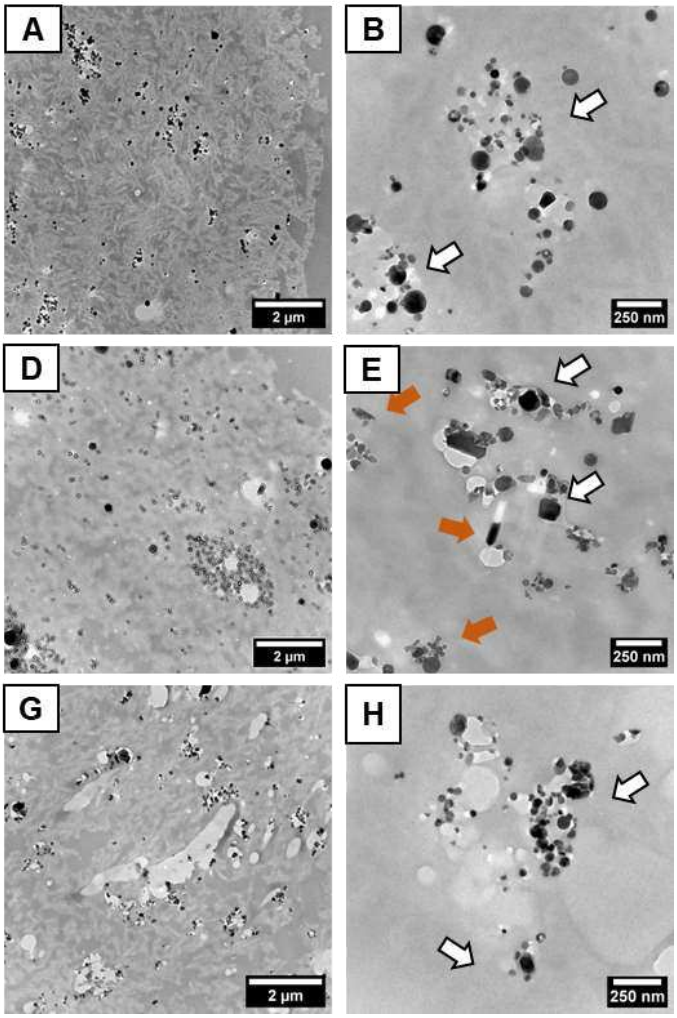

Figure 3. TEM micrographs of (A-B) PLGA-HA, (C-D) PLGA-HA-RIF, and (E-F) PLGA-HA-COL. The white arrows indicate examples of nHA and the orange arrows indicate RIF particles.

Chemical and thermal characterization

The FTIR spectra of the scaffolds are represented in Figure 4A. The characteristic chemical bonds of PLGA were observed in all scaffold spectra. The peak at 1750 cm^{-1} represents the stretching of the carbonyl group (C=O), while the 1084, 1126, and 1181 cm^{-1} peaks correspond to the stretching of the C-O groups of the PLGA ester groups. The 1362, 1380, and 1454 cm^{-1} peaks represent the bending of C-H groups of methyl [27]. The characteristic chemical bonds of HA nanoparticles are also present in the scaffolds of composites containing HA. Peaks corresponding to the phosphate group (PO_4^{3-}) were mainly observed at 1024 cm^{-1} and 866 cm^{-1} [28]. The RIF peaks were overlapped by the polymer peaks due to their low concentration in the scaffolds, which was also observed in

other studies [29,30]. The COL peaks were observed at 3397 cm^{-1}, 2925 - 2828 cm^{-1}, 1647 cm^{-1}, and 1548 cm^{-1}, representing the stretching of the N-H of amide A, C-H of amide B, the C=O of amide I, and the C-N of amide II, respectively [21]. Furthermore, no peaks corresponding to chloroform or HFIP were observed in the scaffolds, showing that the solvent was successfully evaporated throughout the process [31].

The thermal degradation profile of the scaffolds was evaluated using thermogravimetric analysis (Figure 4B-D). For all scaffolds, an initial mass loss of up to 10% was observed near 100 °C, attributed to the evaporation of surface water. [32]. In addition to this initial stage, the scaffolds exhibited a main stage of thermal degradation above 300 °C, corresponding to the degradation of the polymer [32] and COL. The PLGA-HA, PLGA-HA-RIF, and PLGA-COL-HA scaffolds exhibited a mass loss of 82.1%, 79.4%, and 80.2%, respectively. The weight remained, around 20% for all scaffolds, corresponds to the nominal concentration of nHA added (20% w/w), given that HA degrades only at higher temperatures [33].

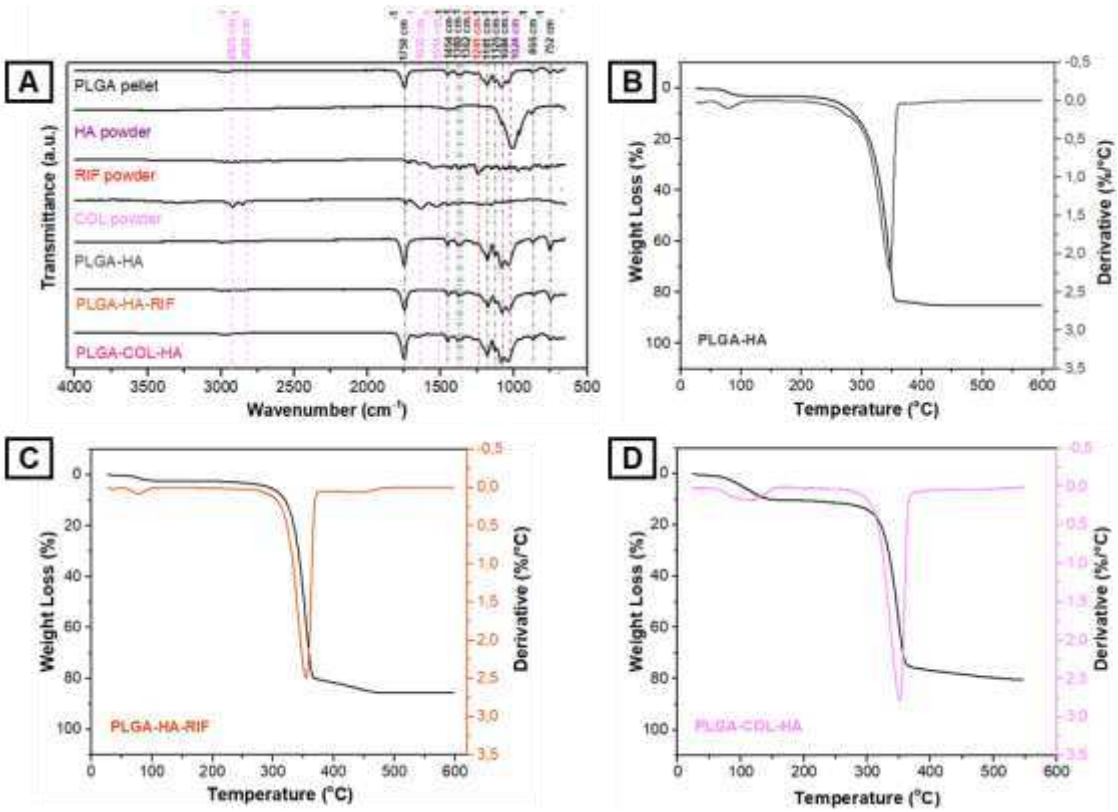

Figure 4. (A) FT-IR spectra of scaffolds and unprocessed polymers and additives and (B) TG and DTG curves of (B) PLGA-HA, (C) PLGA-HA-RIF, and (D) PLGA-HA-COL scaffolds.

An increase in the degradation temperature was observed upon the addition of RIF. The degradation temperature of PLGA-HA-RIF (T_{onset}= 332.3 °C, T_{max}= 353.6 °C, and T_{endset}= 362.5 °C) increased by approximately 10 °C compared to PLGA-20HA (T_{onset}= 317.7 °C, T_{max}= 346 °C, and T_{endset}= 354.1 °C). The incorporation of RIF into polymeric fibers may enhance the thermal stability and degradation temperature of the polymer due to its interaction with the polymeric chains [34]. Meanwhile, COL addition did not affect degradation temperature significantly for PLGA-COL-HA scaffolds (T_{onset}= 318.1 °C, T_{max}= 350.3 °C, and T_{endset}= 356.5 °C) compared to PLGA-HA.

In vitro degradation, wettability, and drug encapsulation and release

The scaffolds' wettability was analyzed using the contact angle technique (Figure 5A). For the scaffolds, contact angles of 102.1° ± 7.8° were found for PLGA-HA, 96.6° ± 3.1° for PLGA-HA-RIF, and 70° ± 8.8° for PLGA-COL-HA (Figure 5A). Thus, it was observed that the scaffolds exhibited a hydrophobic nature due to PLGA [35,36], except for PLGA-COL-HA, as the addition of proteins like COL increased the material's hydrophilicity. Moreover, the RIF addition led to a slight reduction in the contact angle, as observed in other studies [37].

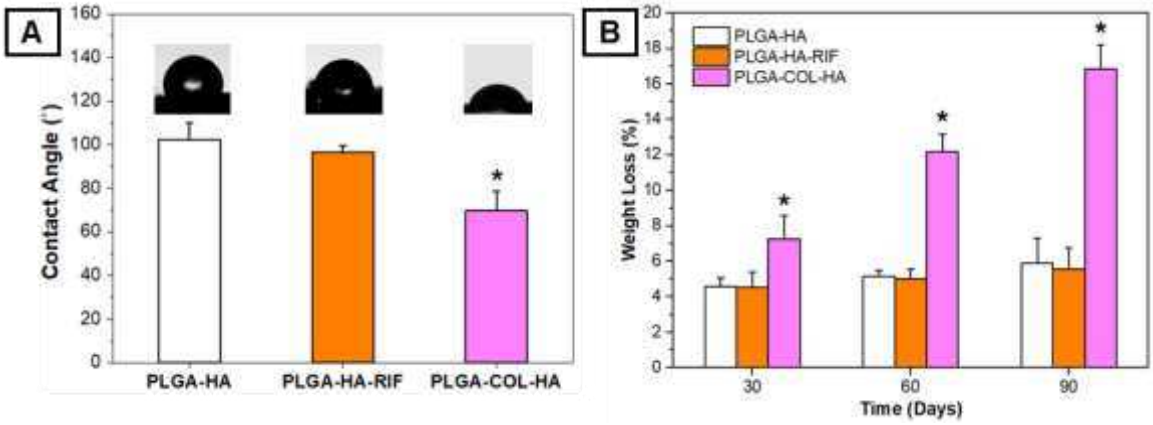

Figure 5. (A) FT-IR spectra of scaffolds and unprocessed polymers and additives and (B) TG and DTG curves of (B) PLGA-HA, (C) PLGA-HA-RIF, and (D) PLGA-HA-COL scaffolds.

The *in vitro* degradation of the scaffolds was assessed hydrolytically for 30, 60, and 90 days (Figure 5B). The PLGA-HA and PLGA-HA-RIF scaffolds exhibited low hydrolytic degradation, with less than 7% degradation after 90 days, except for the PLGA-COL-HA membrane, which showed higher degradation with 16.8% ± 1.4% mass loss. These results are consistent with the hydrophilicity results obtained. However, it is noteworthy to consider

that PLGA is widely recognized for its fast bioresorbability due to its monomers easily metabolized in physiological environments with enzymatic activity, besides hydrolytic degradation.

The addition of rifampicin to the scaffolds was evaluated based on the drug encapsulation efficiency by PLGA and their release into the medium. The PLGA-HA-RIF scaffolds exhibited drug encapsulation of 98.1% ± 4.6%. The release of RIF in PBS was evaluated using UV-Vis spectroscopy (Figure 6). A burst release of RIF from the PLGA-HA-RIF scaffold was observed within the first 48 h with 14.7% ± 2.1%. Subsequently, the release rate tended to be slower and constant over time, resulting in 23.2% ± 3.9% cumulative RIF mass released in 720 h (30 days).

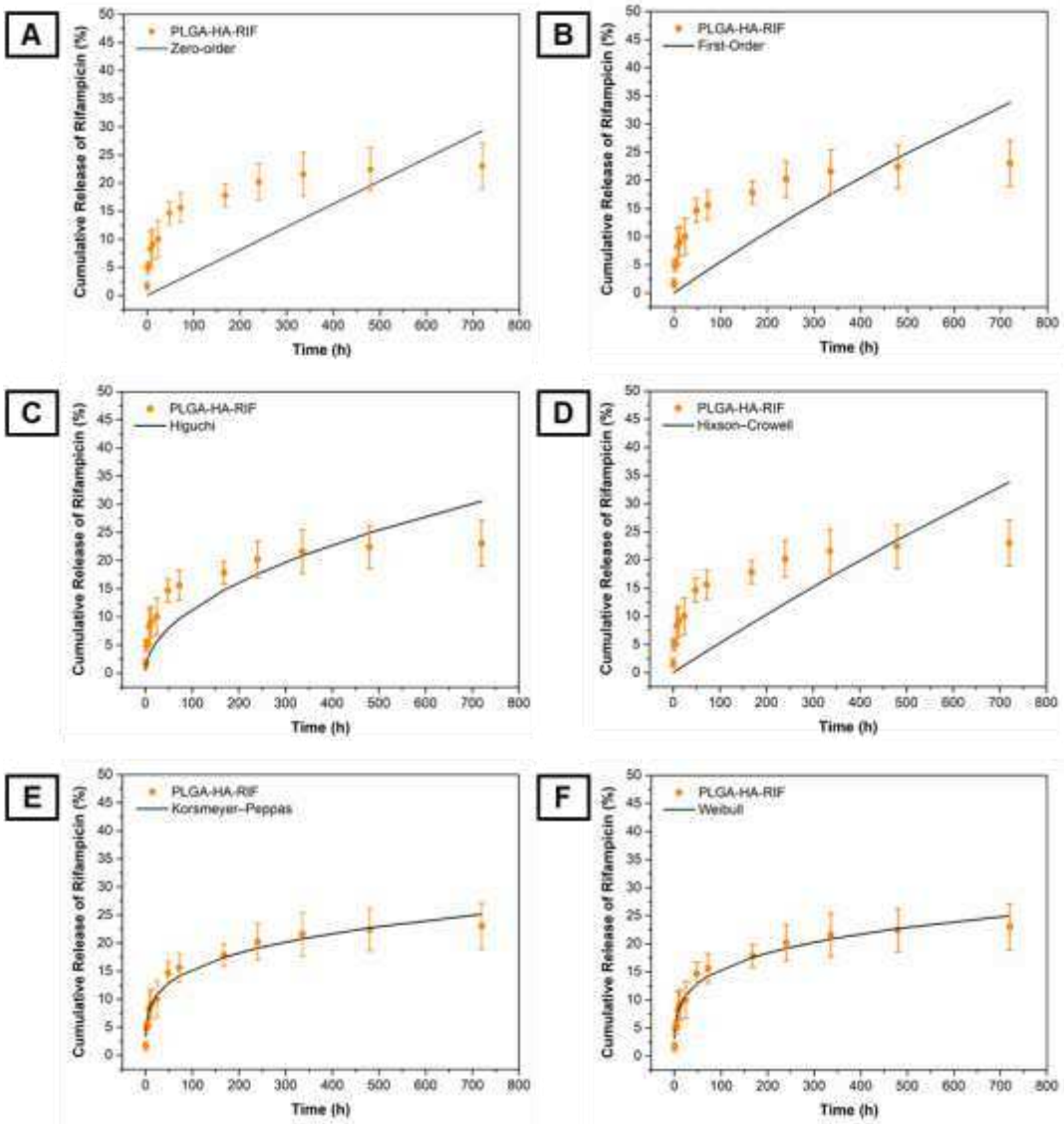

Figure 6. RIF release profile for 720 h and Kinetic models of (a) Zero-Order, (b) First-Order, (c) Higuchi, (d) Hixson-Crowell, (e) Kosmeyer-Peppas, and (f) Weibull applied to the profile

Six kinetic models, zero-order, first-order, Higuchi, Hixson-Crowell, Korsemeyer-Peppas, and Weibull, were used to determine the drug release mechanism of RIF from the scaffold. The Korsemeyer-Peppas (r^2=0.972) and Weibull (r^2=0.976) models presented the highest linearity. The Weibull model is frequently employed to describe the release kinetics from controlled-release mechanisms [38], and the Korsemeyer-Peppas model usually describes the drug release from polymeric systems [39]. Also, the Fickian diffusion mechanism was predominant for the PLGA-HA-RIF scaffold. Thus, the drug release is governed by the diffusion through the polymer matrix (the constant release rate observed) [40], preceded by the initial burst release of the drug adsorbed on the surface [41]. This controlled drug release profile is beneficial for applications in bone implants, as it prevents the initial adhesion and proliferation of bacteria, maintaining local antibacterial activity over several days and reducing the drug's toxicity effects [39,41].

Design and properties of AM Ti6Al4V structure

Ti6Al4V structures were designed and manufactured with different pore sizes (300, 450, and 600 µm) using AM-PBF-EB (Figure 7). For unit cell modeling, body-centered cubic structures were used due to their similarity to bone structure [42]. Through SEM images, it was possible to evaluate the morphology and approximate size of the structure pores (Table 1). The structure exhibited a surface with high roughness due to the remaining powder that was sintered, which is interesting in improving cell adhesion. Finally, with the pycnometry analysis, it was observed that with the increase in pore size, there was an increase in the structure's porosity (Table 1).

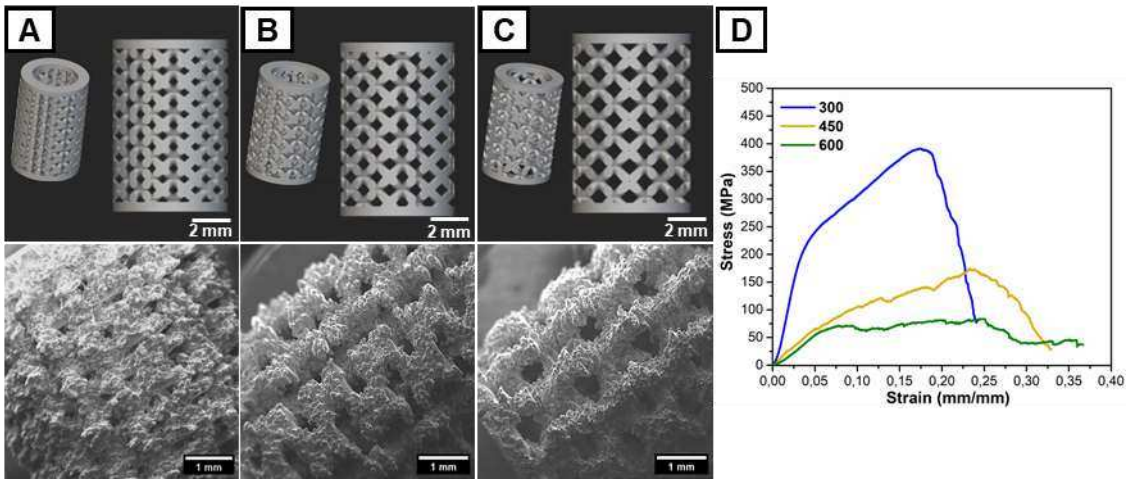

Figure 7. Designed (above) and fabricated (below) AM-PBF-EB structures with pore sizes of (A) 300 µm, (B) 450 µm, and (C) 600 µm, and their (D) Stress-strain curves

The compression test results (Figure 7B and S1) showed that an increase in pore size led to a reduction in the compressive strength and stiffness of the implants (Table 1). It is known that implants need to withstand the mechanical forces exerted but should also have mechanical properties, such as stiffness, close to that of bone, which can vary from 0.05 to 30 GPa [43] to avoid inducing stress-shielding and implant failure [44]. Given its stiffness comparable to trabecular bone and the fact that porosities ranging from 200 to 500 µm have been deemed ideal for bone applications in prior research [45], we opted to focus our further analyses on the 450 µm pore-sized implant.

Table 1. Structural and mechanical properties of the AM Ti6Al4V

Properties	**300 µm**	**450 µm**	**600 µm**
Measured Pore Size (µm)	281.7 ± 58.1	443.5 ± 46.4	584.0 ± 30.1
Density (g/cm^3)	4.49 ± 0.04	4.53 ± 0.02	4.45 ± 0.03
Porosity (%)	45.3 ± 0.5	57.0 ± 0.2	61.1 ± 0.3
Stiffness (GPa)	3.06 ± 0.38	1.84 ± 0.40	1.18 ± 0.08
Compressive Strength at failure (MPa)	438.2 ± 78.7	190.1 ± 84.5	89.4 ± 9.5

Antibacterial and Osteoconductive Properties of the Scaffolds and Implants

The antibacterial activity of the scaffolds and implants was evaluated using the disk diffusion method (Figure 8) with *Escherichia coli (E. coli)* and *Staphylococcus aureus (S. aureus)* bacteria. For both bacteria, the PLGA-HA scaffold and Ti6Al4V structure controls (without RIF) did not exhibit a significant zone of inhibition (ZOI), except for the Ti6Al4V structure in S. aureus (16.7 ± 2.3 mm), which showed a ZOI characteristic of bacteria resistance. When added to *E. coli,* PLGA-HA-RIF scaffolds exhibited a ZOI of 18.7 ± 3.3 mm, indicating intermediate inhibition. Conversely, the implant containing the PLGA-HA-RIF scaffold (Figure S2) had a ZOI of 12.4 ± 2.2 mm, indicating lower diffusion of RIF

through the implant. Regarding *S. aureus*, all scaffolds and implants with PLGA-HA-RIF showed ZOI exceeding 30 mm, indicating sensitive inhibition of the bacteria. These results are consistent since RIF has greater inhibition against gram-positive bacteria, making it suitable for applications such as osteomyelitis [46].

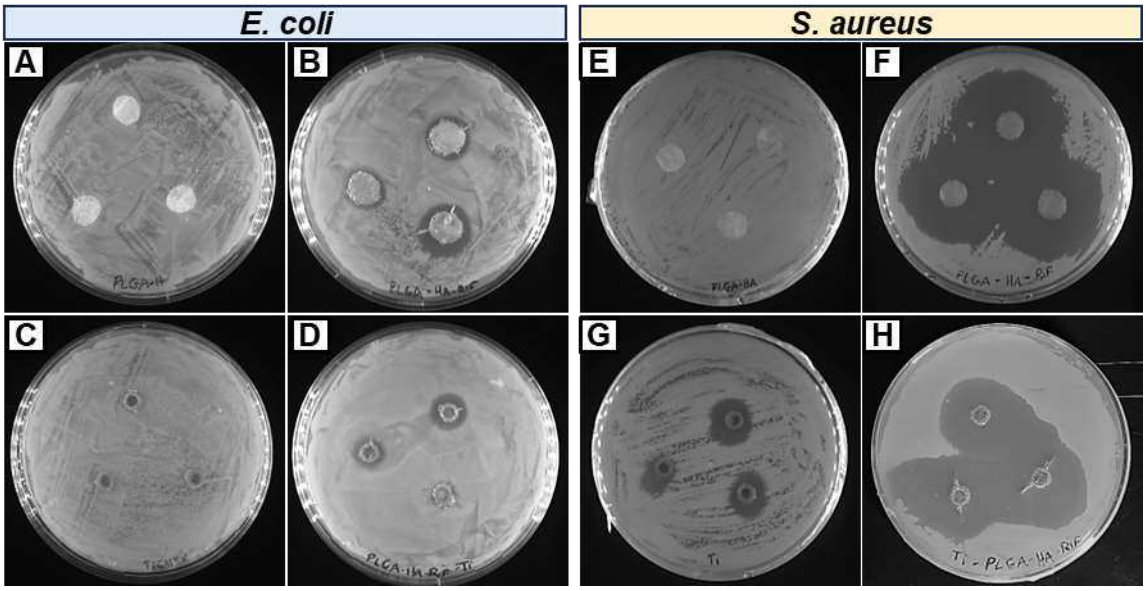

Figure 8. Zone of Inhibition test of (A) PLGA-HA, (B) PLGA-HA-RIF, (C) Ti6Al4V and (D)Ti6Al4V/PLGA-HA-RIF against *E. coli* and (E) PLGA-HA, (F) PLGA-HA-RIF, (G) Ti6Al4V and (H)Ti6Al4V/PLGA-HA-RIF against *S. aureus*.

The osteoconductive capacity of the scaffolds was evaluated based on the formation of apatite on their surface. Thus, the scaffolds were incubated in simulated body fluid (SBF) and observed using SEM (Figure 9). The scaffolds and Ti6Al4V implant exhibited the deposition of spherical particles on their surface, which are characteristic of apatite formation. The EDS analysis also confirmed the calcium (Ca) and phosphorus (P) composition of these deposited mineralized particles on all *scaffolds* and some at the Ti6Al4V implants. Therefore, it is concluded that adding HA increased the scaffolds' bioactivity and their osteoconductive capacity, as observed in other studies [40]. Therefore, using the *scaffolds* in combination with the implant can also help improve its osseointegration.

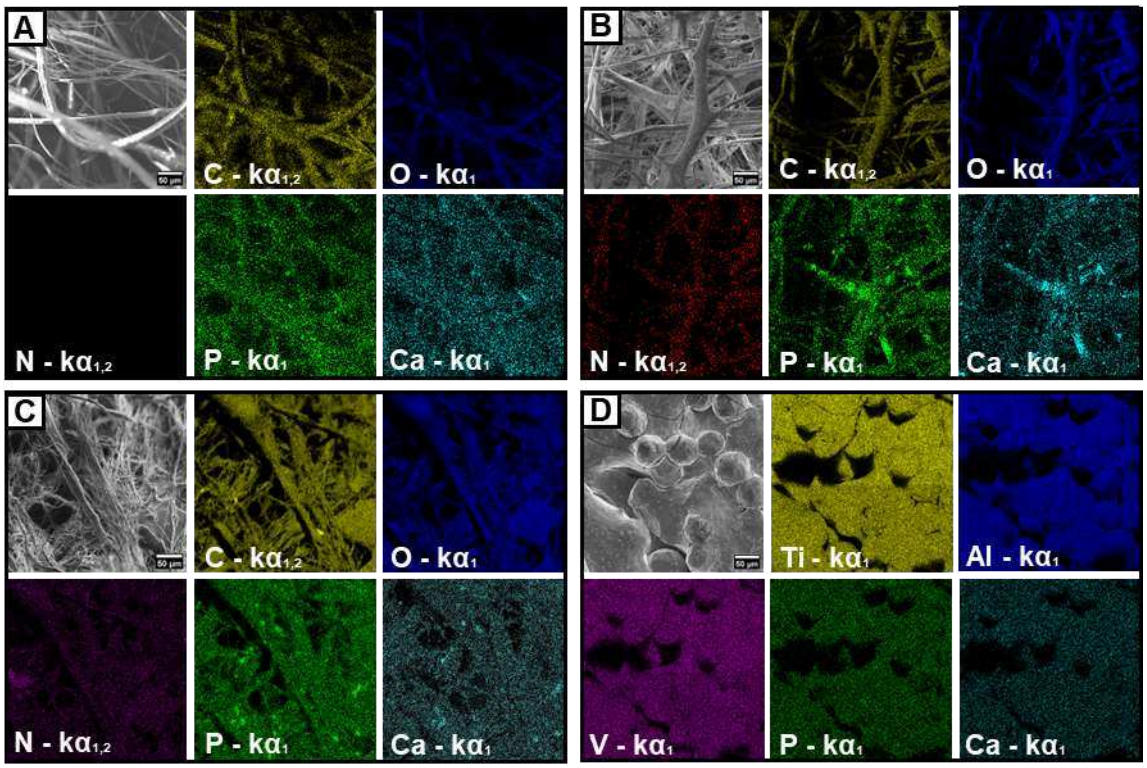

Figure 9. SEM-EDS maps of the (A) PLGA-HA, (B) PLGA-HA-RIF, (C) PLGA-COL-HA scaffolds, and (D) Ti6Al4V implant.

Scaffold cytocompatibility for bone applications

Viability analyses were performed using MTT with MC3T3 preosteoblasts at 24, 48, and 72 hours with all scaffolds and implants (Figure 10A). Compared to the control, PLGA-HA had no significant difference at all times. However, the addition COL slightly reduced proliferation. This reduction in proliferation may be associated with cellular differentiation promoted by HA and COL [47]. The addition of RIF to the scaffolds also reduced cell proliferation compared to the control. It is known that RIF is a potent antibiotic and may have the effect of reducing cell viability [48]. For the implants, a combined effect of reduced viability of Ti6Al4V with the PLGA-HA-RIF scaffolds was observed. However, all scaffolds and implants showed viability higher than 70% at all times and a progressive increase up to 72 hours, indicating that these reduction effects would not be detrimental to cell proliferation.

Confocal microscopy also allowed for the qualitative evaluation of cell proliferation in the scaffolds (Figure 10B-D). After 72 h of culture, cells formed their characteristic

biofilm in all scaffolds and implants, indicating that there was high proliferation and cellular adhesion. This analysis reinforces the findings from the viability study, as cells exhibited a similar proliferation pattern and morphology conducive to high viability, adhesion, proliferation, and cellular differentiation. The scaffolds and implants demonstrated excellent cytocompatibility with pre-osteoblasts, crucial and promising for applications in bone regeneration.

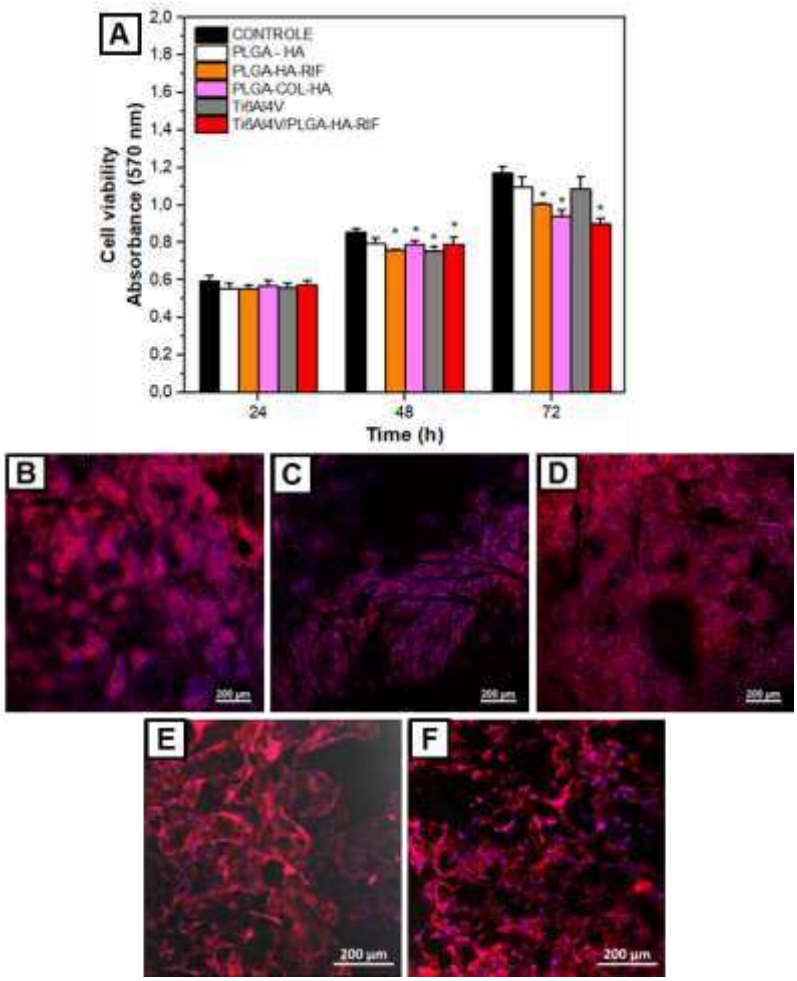

Figure 10. (A) Cell Viability of MC3T3 pre-osteoblasts cell viability on the scaffolds and implants at 24 h, 48 h, and 72 h. Confocal fluorescent images of MC3T3 cells on (B) PLGA-HA, (C) PLGA-HA-RIF, (D) PLGA-COL-HA, (E) Ti6Al4V e (F) Ti6Al4V/PLGA-HA-RIF at 72 h. The blue color corresponds to the nuclei, and the magenta color to the cytoplasm. *$p<0.05$

CONCLUSION

This study introduces a novel approach to bone regeneration by combining porous implants of AM-PBF-EB Ti6Al4V with scaffolds of PLGA-HA-RIF and PLGA-COL-HA. The

morphology and microstructural analysis revealed homogeneous fibers and confirmed the uniform distribution of nHAs within the fibers. Notably, the PLGA-HA-RIF scaffold exhibited the presence of both nHA and RIF particles, with distinct morphologies identified through TEM. The chemical and thermal characterization demonstrated the successful incorporation of HA, RIF, and COL within the scaffolds, as evidenced by FTIR spectra, UV-VIS drug encapsulation, and thermal degradation profiles. Additionally, the controlled release of RIF from the PLGA-HA-RIF scaffold, described by the Weibull and Korsemeyer-Peppas models, highlights its potential for sustained antibacterial activity while maintaining cytocompatibility. The Ti6Al4V structures with 450 µm exhibited mechanical properties and porosity compatible with bone. The scaffolds and implants showed promising antibacterial properties, mainly against *S. aureus*, attributed to the presence of RIF. Moreover, the *scaffolds* had bioactivity promoting osteoconduction and pre-osteoblast proliferation. Overall, these findings underscore the potential of the developed scaffolds and implants for bone tissue engineering applications, offering enhanced osteoconductive properties and bacterial infection prevention.

ACKNOWLEDGMENTS

We express our gratitude for the funding received for this study from the São Paulo Research Foundation (FAPESP) under grants #2020/07923-0 and #2020/14679-9, as well as the National Council for Scientific and Technological Development (CNPq) under grant #140997/2020-2. Additionally, we acknowledge the support provided by TI's Open Labs and the three-dimensional technology core at the Renato Archer Information Technology Center.

REFERENCES

[1] L. C. Zhang, L. Y. Chen, *Adv Eng Mater* **2019**, *21*, 1.
[2] S. M. Kurtz, E. Lau, J. Schmier, K. L. Ong, K. Zhao, J. Parvizi, **2008**, *23*, 984.
[3] S. M. Kurtz, E. Lau, H. Watson, J. K. Schmier, J. Parvizi, *Journal of Arthroplasty* **2012**, *27*, 61.
[4] A. M. Wu, C. Bisignano, S. L. James, G. G. Abady, A. Abedi, E. Abu-Gharbieh, R. K. Alhassan, V. Alipour, J. Arabloo, M. Asaad, W. N. Asmare, A. F. Awedew, M. Banach, S. K. Banerjee, A. Bijani, T. T. M. Birhanu, S. R. Bolla, L. A. Cámera, J. C. Chang, D. Y. Cho, M. T. Chung, R. A. S. Couto, X. Dai, L. Dandona, R. Dandona, F. Farzadfar, I. Filip, F. Fischer, A. A. Fomenkov, T. K. Gill, B. Gupta, J. A. Haagsma, A. Haj-Mirzaian, S. Hamidi, S. I. Hay, I. M. Ilic, M. D. Ilic, R. Q. Ivers, M. Jürisson, R. Kalhor, T. Kanchan, T. Kavetskyy, R. Khalilov, E. A. Khan, M. Khan, C. J. Kneib, V. Krishnamoorthy, G. A. Kumar, N. Kumar, R. Lalloo, S. Lasrado, S. S. Lim, Z. Liu, A. Manafi, N. Manafi, R. G.

Menezes, T. J. Meretoja, B. Miazgowski, T. R. Miller, Y. Mohammad, A. Mohammadian-Hafshejani, A. H. Mokdad, C. J. L. Murray, M. Naderi, M. D. Naimzada, V. C. Nayak, C. T. Nguyen, R. Nikbakhsh, A. T. Olagunju, N. Otstavnov, S. S. Otstavnov, J. R. Padubidri, J. Pereira, H. Q. Pham, M. Pinheiro, S. Polinder, H. Pourchamani, N. Rabiee, A. Radfar, M. H. U. Rahman, D. L. Rawaf, S. Rawaf, M. R. Saeb, A. M. Samy, L. Sanchez Riera, D. C. Schwebel, S. Shahabi, M. A. Shaikh, A. Soheili, R. Tabarés-Seisdedos, M. R. Tovani-Palone, B. X. Tran, R. S. Travillian, P. R. Valdez, T. J. Vasankari, D. Z. Velazquez, N. Venketasubramanian, G. T. Vu, Z. J. Zhang, T. Vos, *Lancet Healthy Longev* **2021**, *2*, e580.
[5] A. M. Jakoi, J. A. Iorio, P. J. Cahill, *Musculoskelet Surg* **2015**, *99*, 171.
[6] W. Wang, K. W. K. Yeung, *Bioact Mater* **2017**, *2*, 224.
[7] R. Langer, J. P. Vacanti, *Science (1979)* **1993**, *260*, 920.
[8] O. Nemoto, T. Asazuma, Y. Yato, H. Imabayashi, H. Yasuoka, A. Fujikawa, *European Spine Journal* **2014**, *23*, 2150.
[9] Y. Chen, X. Wang, X. Lu, L. Yang, H. Yang, W. Yuan, D. Chen, *European Spine Journal* **2013**, *22*, 1539.
[10] Z. Bal, T. Kaito, F. Korkusuz, H. Yoshikawa, *Emergent Mater* **2020**, *3*, 521.
[11] S. W. Ha, J. Park, M. M. Habib, G. R. Beck, *ACS Appl Mater Interfaces* **2017**, *9*, 39185.
[12] Y. Ozawa, T. Kubota, T. Yamamoto, N. Tsukune, R. Koshi, T. Nishida, M. Asano, S. Sato, *J Oral Sci* **2018**, *60*, 514.
[13] S. Liu, J. M. Yu, Y. C. Gan, X. Z. Qiu, Z. C. Gao, H. Wang, S. X. Chen, Y. Xiong, G. H. Liu, S. E. Lin, A. McCarthy, J. V. John, D. X. Wei, H. H. Hou, *Military Medical Research 2023 10:1* **2023**, *10*, 1.
[14] Y. Zamani, J. Mohammadi, G. Amoabediny, M. N. Helder, B. Zandieh-Doulabi, J. Klein-Nulend, *Regen Eng Transl Med* **2020**, DOI 10.1007/s40883-020-00163-1.
[15] S. E. Gilchrist, D. Lange, K. Letchford, H. Bach, L. Fazli, H. M. Burt, *Journal of Controlled Release* **2013**, *170*, 64.
[16] A. Hasan, G. Waibhaw, V. Saxena, L. M. Pandey, *Int J Biol Macromol* **2018**, *111*, 923.
[17] I. C. P. Rodrigues, É. S. N. Lopes, K. D. Pereira, S. C. Huber, A. L. Jardini, J. M. Annichino-Bizzacchi, A. D. Luchessi, L. P. Gabriel, *Sci Rep* **2022**, *12*, DOI 10.1038/s41598-022-09040-z.
[18] F. Jahanmard, M. Croes, M. Castilho, A. Majed, M. J. Steenbergen, K. Lietaert, H. C. Vogely, B. C. H. van der Wal, D. A. C. Stapels, J. Malda, T. Vermonden, S. Amin Yavari, *Journal of Controlled Release* **2020**, *326*, 38.
[19] J. H. Ryu, J. S. Kwon, K. M. Kim, H. J. Hong, W. G. Koh, J. Lee, H. J. Lee, H. J. Choi, S. Yi, H. Shin, M. H. Hong, *ACS Omega* **2019**, *4*, 2302.
[20] I. C. Pereira Rodrigues, L. Tamborlin, A. A. Rodrigues, A. L. Jardini, A. Ducati Luchessi, R. Maciel Filho, É. S. Najar Lopes, L. Pellizzer Gabriel, *J Appl Polym Sci* **2020**, *137*, DOI 10.1002/app.48455.
[21] I. C. P. Rodrigues, K. D. Pereira, L. F. Woigt, A. L. Jardini, A. D. Luchessi, É. S. N. Lopes, T. J. Webster, L. P. Gabriel, *Artif Organs* **2021**, *45*, DOI 10.1111/aor.13857.
[22] M. Krifa, M. A. Hammami, H. Wu, *The Journal of The Textile Institute* **2015**, *106*, 284.
[23] L. Ren, V. Pandit, J. Elkin, T. Denman, J. A. Cooper, S. P. Kotha, *Nanoscale* **2013**, *5*, 2337.
[24] A. A. Shitole, P. W. Raut, N. Sharma, P. Giram, A. P. Khandwekar, B. Garnaik, *J Mater Sci Mater Med* **2019**, *30*, 1.

[25] M. Zhong, J. Lin, Y. Yang, M. Liu, G. Guo, D. Ji, R. Zhang, J. Zhang, *J Biomater Appl* **2022**, *36*, 1588.
[26] H. Liu, Z. Z. He, L. Yu, J. Ma, X. P. Jin, *J Incl Phenom Macrocycl Chem* **2021**, *101*, 111.
[27] T. M. B. K. dos Santos, C. Merlini, Á. Aragones, M. C. Fredel, *Materials Science and Engineering: C* **2019**, *103*, 109728.
[28] M. Krok-Borkowicz, K. Reczyńska, Ł. Rumian, E. Menaszek, M. Orzelski, P. Malisz, P. Silmanowicz, P. Dobrzyński, E. Pamuła, *International Journal of Molecular Sciences 2020, Vol. 21, Page 7541* **2020**, *21*, 7541.
[29] A. Sharma, V. Puri, P. Kumar, I. Singh, K. Huanbutta, *Polymers 2021, Vol. 13, Page 1514* **2021**, *13*, 1514.
[30] A. Sharma, V. Puri, P. Kumar, I. Singh, *Membranes 2021, Vol. 11, Page 7* **2020**, *11*, 7.
[31] I. C. P. Rodrigues, L. Tamborlin, A. A. Rodrigues, A. L. Jardini, A. D. Luchessi, R. Maciel Filho, É. S. N. Lopes, L. P. Gabriel, *J Appl Polym Sci* **2020**, *137*, 1.
[32] Y. Yu, L. Kong, L. Li, N. Li, P. Yan, *Nanoscale Res Lett* **2015**, *10*, 1.
[33] T. Wang, A. Dorner-Reisel, E. Müller, *J Eur Ceram Soc* **2004**, *24*, 693.
[34] C. R. Gough, X. Hu, *International Journal of Molecular Sciences 2021, Vol. 22, Page 9588* **2021**, *22*, 9588.
[35] S. Jin, F. Sun, Q. Zou, J. Huang, Y. Zuo, Y. Li, S. Wang, L. Cheng, Y. Man, F. Yang, J. Li, *Biomacromolecules* **2019**, *20*, 2058.
[36] W. Li, X. Yang, S. Feng, S. Yang, R. Zeng, M. Tu, *Journal of Materials Science: Materials in Medicine 2018 29:8* **2018**, *29*, 1.
[37] S. E. Gilchrist, D. Lange, K. Letchford, H. Bach, L. Fazli, H. M. Burt, *Journal of Controlled Release* **2013**, *170*, 64.
[38] H. Qu, Q. Yao, T. Chen, H. Wu, Y. Liu, C. Wang, A. Dong, *Adv Colloid Interface Sci* **2024**, *325*, 103099.
[39] M. Zegre, E. Poljańska, L. A. Caetano, L. Gonçalves, A. Bettencourt, *Int J Pharm* **2023**, *648*, 123584.
[40] A. S. Kranthi Kiran, A. Kizhakeyil, R. Ramalingam, N. K. Verma, R. Lakshminarayanan, T. S. S. Kumar, M. Doble, S. Ramakrishna, *Ceram Int* **2019**, *45*, 18710.
[41] H. F. Hetta, H. F. Hetta, E. A. Ahmed, E. A. Ahmed, A. G. Hemdan, H. E. M. El-Deek, S. Abd-Elregal, N. H. Abd Ellah, *https://doi.org/10.2217/nnm-2020-0001* **2020**, *15*, 1375.
[42] N. N. A. A. Abdullah, A. H. Abdullah, M. H. Ramlee, *Mater Today Proc* **2023**, DOI 10.1016/J.MATPR.2023.09.199.
[43] S. H. Wu, Y. Li, Y. Q. Zhang, X. K. Li, C. F. Yuan, Y. L. Hao, Z. Y. Zhang, Z. Guo, *Artif Organs* **2013**, *37*, DOI 10.1111/aor.12153.
[44] S. Mondal, R. Ghosh, *Comput Methods Biomech Biomed Engin* **2019**, *22*, 1247.
[45] B. Thavornyutikarn, N. Chantarapanich, Q. Chen, *Bone Tissue Engineering Scaffolding : Computer-Aided Scaffolding Techniques*, **2014**.
[46] A. R. Zelmer, R. Nelson, K. Richter, G. J. Atkins, *Bone Research 2022 10:1* **2022**, *10*, 1.
[47] R. Shu, R. McMullen, M. J. Baumann, L. R. McCabe, *J Biomed Mater Res A* **2003**, *67A*, 1196.
[48] T. Chen, Q. Li, L. Guo, L. Yu, Z. Li, H. Guo, H. Li, M. Zhao, L. Chen, X. Chen, Q. Zhong, L. Zhou, T. Wu, *Materials Science and Engineering: C* **2016**, *58*, 659.

SUPPORTING INFORMATION

Implants promoting osteoconduction and local antibacterial activity for effective osseointegration and osteomyelitis prevention

Isabella Caroline Pereira Rodrigues[1], Karina Danielle Pereira[2,3], Augusto D. Luchessi[2,3], Laís Pellizzer Gabriel[1,2], Éder Sócrates Najar Lopes[1*]

[1] School of Mechanical Engineering, University of Campinas, Campinas, São Paulo, Brazil
[2] School of Applied Sciences, University of Campinas, Limeira, São Paulo, Brazil
[3] Institute of Biosciences, São Paulo State University, Rio Claro, São Paulo, Brazil
* Correspondence to: Éder Sócrates Najar Lopes (E-mail esnlopes@unicamp.br; Telephone: +55 (19) 3521-0017; Street address: Rua Mendeley, 200, Campinas 13083-860, SP, Brazil)

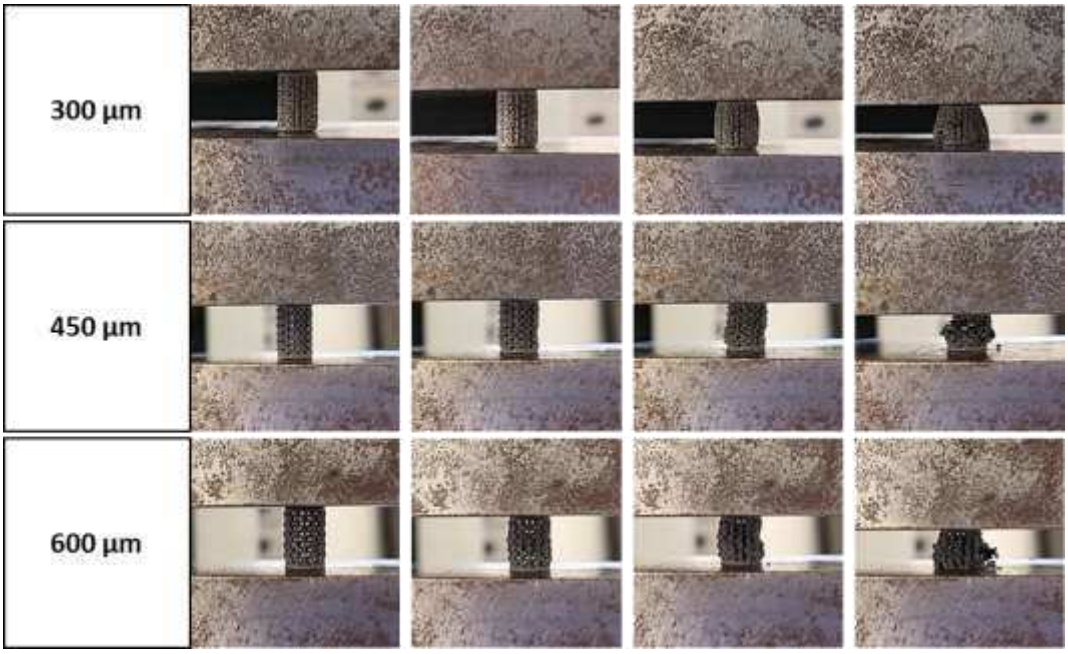

Figure S1. Ti6Al4V structures with different pore sizes during the compression test.

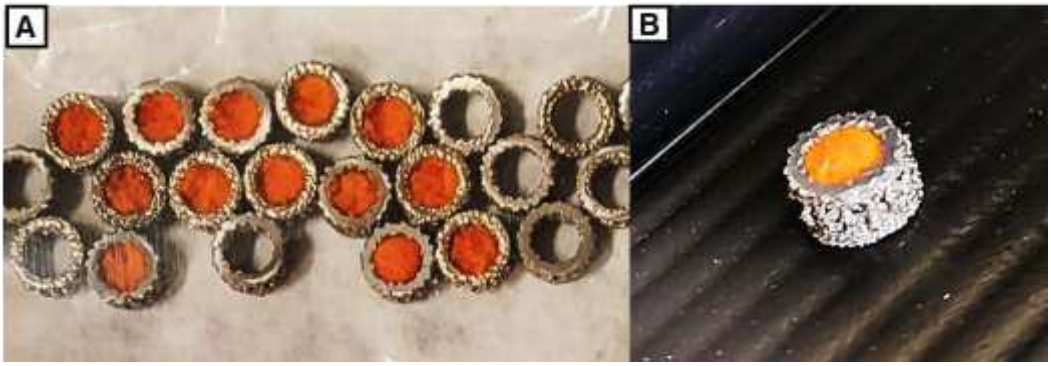

Figure S2. (A) Ti6Al4V implants produced with and without the PLGA-HA-RIF *scaffold* for analysis and (B) Side--view photo of the implant.

6.3. Manuscrito do Artigo 3

Multimaterial Coextrusion (Bio)printing of Composite Polymer Biomaterial Ink and Hydrogel Bioink for Tissue Fabrication

Isabella C. P. Rodrigues, Luis C. O. Clark, Xiao Kuang, Regina Sanchez, Éder S. N. Lopes, Laís P. Gabriel, Yu Shrike Zhang*

I. C. P. Rodrigues, L. C. O. Clark, X. Kuang, R. Sanchez, Y. S. Zhang
Division of Engineering in Medicine, Department of Medicine, Brigham and Women's Hospital, Harvard Medical School, Cambridge, MA 02139, USA
*E-mail: yszhang@bwh.harvard.edu

I. C. P. Rodrigues, L. P. Gabriel, E. S. N. Lopes
School of Mechanical Engineering, University of Campinas, Rua Mendeley, 200, Campinas, SP, 13083-860, Brazil

L. P. Gabriel
School of Applied Sciences, University of Campinas, Rua Pedro Zaccaria, 1300, Limeira, SP, 13484-350, Brazil

Abstract

Bone tissue engineering strategies face considerable challenges owing to the complexity of the bone. This study introduces an unconventional method based on multimaterial 3D coextrusion-(bio)printing to address some of these challenges. The strategy enables simultaneous (bio)printing of a poly(lactic-co-glycolic acid)-based polymer ink laden with hydroxyapatite and a gelatin methacryloyl (GelMA)-based hydrogel bioink containing mesenchymal stem cells. The resulting composite scaffolds exhibited a trabecular bone-like porosity and favorable compressive properties, surpassing those of GelMA alone. The (bio)printed MSCs demonstrated favorable viability, proliferation, morphology, and differentiation. This converged approach in multimaterial (bio)printing has the potential to transform the field of bone tissue engineering, offering a more efficient and effective way to regenerate skeletal tissues.

Keywords: 3D printing; additive manufacturing; bioprinting; bone; poly(lactic-co-glycolic acid) (PLGA); gelatin methacryloyl (GelMA)

1. Introduction

Bone disorders, such as tumors, fractures, and other diseases, are prevalent worldwide [1], mostly requiring grafts to restore the compromised segments. Tissue engineering technologies have evolved immensely in the past years to produce synthetic grafts to regenerate the bone. In particular, three-dimensional (3D) printing techniques are good examples that enable the fabrication of robust grafts with personalizable shapes, porosities, and a wide range of biomaterials [2,3]. 3D (bio)printing further allows different cells to be included and patterned in specific positions [4,5].

For bioprinting, it is oftentimes essential to use hydrogels since they can conveniently allow encapsulation and protection of cells during the bioprinting process [6]. Hydrogels are hydrophilic polymeric networks capable of maintaining large amounts of water [7,8], which can be combined with cells to formulate the bioinks for bioprinting [6]. A class of widely used hydrogel bioink materials include naturally derived biomolecules such as collagen, alginate, or gelatin methacryloyl (GelMA) [6,9]. Among the different options, GelMA is a collagen-derived and cost-effective biomaterial that has been applied as a bioink with promising results [9–12] because of its biocompatibility serving as a familiar microenvironment for cells, as well as on-demand photocrosslinking ability being able to be relatively easily shaped into 3D structures. However, it is known that constructs built purely with hydrogels, such as GelMA, usually possess low mechanical properties [11], which makes it less feasible for applications related to the bone.

Multimaterial extrusion techniques can be used to modulate the properties of bioprinted hydrogel grafts. Nevertheless, these techniques have mostly only allowed different hydrogels to be bioprinted simultaneously [13], which still generally present low mechanical properties. Thus, some research has explored combining other materials with bioinks to enhance the mechanical strengths of 3D-printed/bioprinted grafts [12]. One alternative is the incorporation of polymers[14,15] or ceramics[16] into the printed hydrogel constructs, which may still require mechanical improvement for *in vivo* implantation [14]. Another approach is layer-by-layer sequential deposition or co-printing of a polymer framework and a cell-laden hydrogel [17]. However, this strategy can be time-consuming as the nozzles are constantly exchanged and may thus result in the loss of structures and cells over the duration needed to finish printing.

Therefore, a multimaterial coextrusion technique to simultaneously deposit the polymer and the cell-laden bioink would be of great interest to overcome these shortcomings.

Poly(lactic-co-glycolic acid) (PLGA) has gained attention in recent studies in 3D printing as a promising polymeric biomaterial for bone regeneration [15,18,19]. This is due to its ability to balance mechanical strength and cytocompatibility and act as a degradable matrix that the new tissue can gradually replace. Considering the limitations of high temperatures or toxic solvents usually required to solubilize the polymer molecules, no studies have explored such a simultaneous coextrusion combination with bioink to this date. Of interest, recent works have shown that polymers can also be 3D-printed using solvents such as dimethyl sulfoxide (DMSO), which are more bearable to cells upon short-time exposures [20]. This alternative allows different polymers and composites containing pivotal osteoconductive particles, such as hydroxyapatite (HA), to be simultaneously (bio)printed with hydrogels.

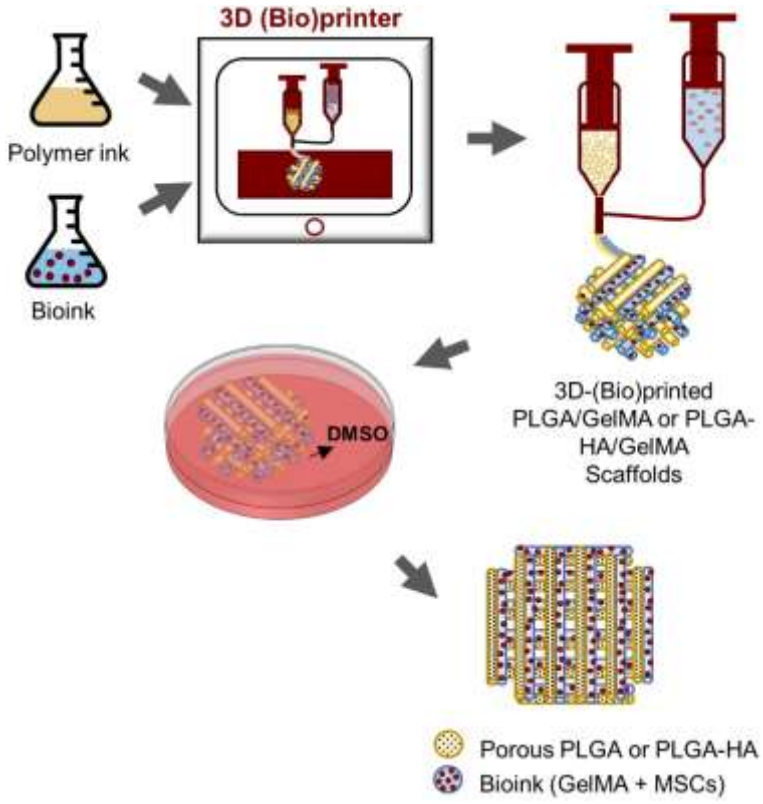

Figure 1. Schematic representation of the multimaterial coextrusion 3D (bio)printing strategy.

In this study, we for the first time report a combinatory 3D (bio)printing strategy to enable multimaterial coextrusion of the polymer-nanoparticle composite and the hydrogel bioink. To showcase the versatility and uniqueness of our strategy, we conducted coextrusion experiments involving pure PLGA or PLGA-HA concurrently printed with GelMA loaded with human mesenchymal stem cells (MSCs). The (bio)printed scaffolds'

morphological, chemical, mechanical, and structural properties were characterized. In addition, we extended our analyses to include a set of detailed evaluations of the (bio)printed scaffolds during culture, covering crucial aspects such as compressive properties, MSC viability, proliferation, and differentiation. This effective process can enable high cell viability levels at relatively fast fabrication speeds (at least half the time needed to print two inks separately) while balancing the mechanical strength requirements and biological activities of the composite scaffolds. Thus, this new 3D (bio)printing strategy may be useful for extended applications, including but likely beyond the bone tissue engineering scenario demonstrated in this work.

2. Materials and methods

2.1. Materials

The 3D-printed scaffolds were produced using PLGA pellets (#LG 824S) from Evonik Corporation (Parsippany, NJ, USA), and DMSO (#276855) and HA (#677418) from Sigma-Aldrich (St. Louis, MO, USA). In addition, Gelatin from porcine skin (#G2500), methacrylic anhydride (#276685), and the photoinitiator lithium phenyl-2,4,6-trimethyl-benzoyl phosphinate (LAP; #900889) were purchased from Sigma-Aldrich, and Dulbecco's phosphate-buffered saline solution (DPBS; pH 7.4, #14190) was purchased from ThermoFisher Scientific (Waltham, MA, USA) to produce the GelMA bioink.

2.2. Cell culture

Human MSCs (#PT-2501) were purchased from Lonza Bioscience (Basel, Switzerland) and cultured in MSC medium composed of MSC Growth Medium BulletKit™ (#PT-3001), also from Lonza Bioscience, supplemented with 1% v/v Antibiotic-Antimycotic (#15240) from ThermoFisher Scientific. The MSCs were maintained in an incubator at 37 ºC and 5% CO_2 with a humidified atmosphere, and the medium was changed every 2 days.

2.3. Bioink preparation

The GelMA bioink was prepared with medium-level methacryloyl-modification following well-established protocols described in previous works [10,21–23]. GelMA was synthesized by dissolving gelatin in DPBS and posteriorly adding methacrylic anhydride to react with gelatin. The unreacted methacrylic anhydride molecules were removed through dialysis, and the final solution was freeze-dried and stored at -20 ºC until further use. Before

bioprinting, the freeze-dried GelMA was dissolved in DPBS, mixed with 0.3% v/v of the LAP photoinitiator, and microfiltered for sterilization to prepare the hydrogel. The cells previously cultured were trypsinized, resuspended in fetal bovine serum (FBS; #10437) containing 1% v/v Antibiotic-Antimycotic (#15240062), both from ThermoFisher Scientific and mixed with GelMA at a concentration of 5×10^6 cells mL^{-1} to obtain the bioink.

2.4. Rheological Characterization of the inks and bioink

The apparent viscosity and temperature-dependent viscoelasticity of the PLGA-based inks were measured on a DHR-3 rheometer (TA Instruments) with a 40-mm-diameter plate geometry (steel Peltier plate). The gap height was set to 1 mm for the samples. The samples were loaded on the lower plate, and any excess samples were trimmed after lowering the gap height. The apparent viscosities ink solutions were measured from 0.1 to 100 s^{-1} using a steady-state flow sweep at a constant temperature. Oscillatory temperature sweeps were performed from 60 to 30 °C for PLGA and from 15 to 37 °C for GelMA at a ramping rate of 2–3 $^oC\ min^{-1}$ at a shear strain of 1% and a frequency of 1 Hz.

2.5. 3D (bio)printing of PLGA/GelMA composite scaffolds

The PLGA scaffolds were printed using an Allevi 2 extrusion bioprinter (3D Systems, Rock Hill, SC, USA). First, the PLGA pellets were dissolved using DMSO at a concentration of 10% w/v, and the solution was continuously mixed at 90 ºC until homogenous to prepare the PLGA ink. For the PLGA-HA ink, 10% w/w HA was homogenized into the solution. After that, the syringe was filled with the PLGA or PLGA-HA ink, which was maintained at 50 ºC and extruded at 15 psi, according to the G-codes designed using the Repetier-Host software (single layer of 15-mm square grids with nine-square pores of approximately 4 mm each) at 3 mm s^{-1}.

For coextrusion, the other syringe in the bioprinter was filled with the GelMA bioink, prepared at 37 ^oC with a cooling step at 4 ^oC for 5 min, and extruded at 30 psi, simultaneously with the PLGA-based ink using our customized two-channel printhead, based on needles (23G) and silicon tubing. The final (bio)printed scaffolds were exposed to ultraviolet (UV) light (13.0 W cm^{-2} for 30 s) to be photocrosslinked for the GelMA portions. Afterwards, the (bio)printed scaffolds were washed with DPBS and MSC medium for non-solvent/solvent-exchange, and incubated with MSC medium for 1, 3, 7, and 14 days. The GelMA bioink was also extruded alone and incubated for comparison with the coextruded scaffolds.

2.6. Characterizations of printed PLGA scaffolds

The microstructures of the printed PLGA and PLGA-HA scaffolds were evaluated using a fluorescence microscope (Axio observer, Carl Zeiss, Oberkochen, Germany). Rhodamine B, a fluorescent dye (#83689; Sigma-Aldrich) was added to the polymer solutions, and a thin layer of PLGA or PLGA-HA was cast. The materials' microstructures were analyzed, and 40 pore sizes were measured using the ImageJ software [24] to plot the histograms. The porosity values of the printed scaffolds were evaluated using apparent density (ρ_{ap}) and bulk density (ρ_{bulk}) measurements. The apparent density was determined by measuring the mass and volume of the printed scaffolds after dried in vacuum. The bulk density was determined by measuring the mass and volume of PLGA or PLGA-HA scaffold after casting in a mold with a known volume. The porosity was then calculated using the following formula [25].

$$\mathrm{P} = \left(1 - \frac{\rho_{\mathrm{ap}}}{\rho_{\mathrm{bulk}}}\right) \times 100\%$$

The volume shrinkage of the printed structures was assessed using linear measurements. The PLGA or PLGA-HA sample was cast in a polydimethylsiloxane (PDMS; SYLGARD™ 184; Dow Chemical Company, Midland, MI, USA) mold with a known volume. After the solvent-exchange process of DMSO in water, linear measurements of the scaffold's length, width, and thickness were taken at different time points. The volume shrinkage was calculated as the percentage change in the volume of the sample. The chemical composition of the scaffolds was analyzed using Fourier-transform infrared (FTIR, Spectrum 100; Perkin Elmer, Waltham, MA, USA) with a resolution of 4 cm^{-1} and a spectra range of 4000 to 650 cm^{-1}. To evaluate the hydrolytic degradation of the printed scaffolds, the PLGA and PLGA-HA samples were placed in DPBS at 37 ℃ and left to degrade for varying periods: 1, 2, 4, 8, and 12 weeks. At each time point, the samples were removed from the DPBS and dried under vacuum. The mass loss was quantified by comparing the initial mass of the sample with the final mass at each time point after drying.

2.7. Mechanical property measurements

The tensile properties of polymeric scaffolds were measured using a mechanical testing machine (Instron 6800 series, Norwood, MA, USA) with a load cell of 100 N. For that, the PLGA and PLGA-HA inks were cast in PDMS rectangular molds of 30×10 mm^2 in size. The samples were subjected to the solvent-exchange process in water for 15 min, 24, 48, 96, 168, and 336 h for the analyses. After superficial drying, the samples clamped in the grips and

were subjected to a tensile test (ASTM D638-14), where gauge length (~15 mm), thickness (~0.5 mm), and width (~10 mm) were determined, and the strain rate was fixed at 5 mm min^{-1}. The strengths and strains at break, and moduli were determined by calculating the slopes of the linear elastic portion of the stress-strain curves.

The lap-shear test was performed on a mechanical testing system (100-N load-cell, Instron 3342). Bilayered rectangular samples (16 mm by 15 mm by 1.5 mm, length by width by thickness) were prepared by casting GelMA ink on top of the PLGA ink. After photocuring and soaking in DPBS overnight, the samples were sandwiched between two glass slides by superglue. The two sides of the glasses were attached to the bottom and top fixture for stretching at 10 mm min^{-1}. The lap shear stress was calculated by the measured force divided by the overlap area (or sample area).

Moreover, the compressive properties of the scaffolds were examined according to ASTM D695-15. For that, the same volumes of polymer ink and GelMA bioink were cast, one on top of the other, in a cubic PDMS mold of 10×10×10 mm^3. Compression tests were performed at a fixed rate of 0.5 mm min^{-1}. The compressive strengths and strains at failure were determined at the moment of failure or at total compression. The compressive modulus of elasticity was calculated as the slope of the linear region of the stress-strain curves.

2.8. Cell viability assay

The viability of the cells in the multimaterial (bio)printed scaffolds (single-layer triangles of 6 mm in side-length) was evaluated on 1, 3, 7, and 14 days using the Live/Dead assay. The kit containing calcein-AM (C3100MP), to stain live cells, and ethidium homodimer-1 (E1169), to stain dead cells, was purchased from ThermoFisher Scientific, and the experiments were conducted following the manufacturer's protocol. The images were taken using the fluorescence microscope. The numbers of live and dead cells in 6 random images for each scaffold were counted using the ImageJ software with the Analyze particles plugin.

2.9. Cell metabolic activity assay

According to the manufacturer's protocol, the [3-(4,5-dimethylthiazol-2-yl)-5-(3-carboxymethoxyphenyl)-2-(4-sulfophenyl)-2H-tetrazolium] (MTS) assay was used to measure formazan absorbance for quantification of cell proliferation on 1, 3, 7, and 14 days in the (bio)printed scaffolds (single-layer triangles of 4 mm in side-length). The MTS solution was prepared using the MSC medium and the MTS reagent (#G1111) from Promega

Corporation (Madison, WI, USA) at a proportion of 3:1 v/v. After removing the medium, 1 mL of the MTS solution was added to each well. After incubating for 3 h at 37 ºC, the supernatant was read by a spectrophotometer (SpectraMax M3, Molecular Devices, San Jose, CA, USA) at 490 nm for quantification. Six samples were measured for each type (bio)printed scaffolds at each time point.

2.10. Cell morphology assessments

For F-actin and nuclei staining, the samples (single-layer triangles of 6 mm in side-length) were fixed on 1, 3, 7, and 14 days of proliferation, and after weeks 1, 2, and 4 of differentiation, with 10% w/v formalin solution (#F5554; Sigma-Aldrich) for 15 min at room temperature. Next, the samples were washed with DPBS and blocked with 5% v/v bovine serum albumin (BSA; #A3983; Sigma-Aldrich) solution in DPBS at room temperature for 1 h. After blocking, the BSA solution was removed, and a solution of Alexa Fluor 594-phalloidin (#A12381; ThermoFisher Scientific) in DPBS with a ratio of 1:400 v/v was added to the samples and left overnight at 4 ºC. The phalloidin solution was removed, and the samples were washed with DPBS; the samples were then incubated with 4',6-diamidino-2-phenylindole (DAPI; #D1306, ThermoFisher Scientific) solution in DPBS diluted at 1:5000 v/v for 15 min, washed, and analyzed using the fluorescence microscope. To evaluate cell spreading, the areas of 20 cells were measured from the images using ImageJ.

2.11. Differentiation assay and immunostaining

After 14 days of culture, the MSC-encapsulating constructs (single-layer triangles of 6 mm in side-length) were cultured in the Human MSC Osteogenic Differentiation Medium BulletKitTM (PT-3002) from Lonza Bioscience for 1, 2, and 4 weeks. For the immunostaining assay, the samples were fixed on weeks 1, 2, and 4 with 10% w/v formalin solution (Sigma-Aldrich) for 15 min at room temperature. Next, the samples were washed with DPBS and 1% v/v BSA/DPBS washing buffer. After the washing buffer, the samples were incubated in a blocking buffer of 5% v/v BSA/DPBS solution and 0.2% v/v Triton X-100 (#T8787; Sigma-Aldrich) in DPBS at room temperature for 2 h. The samples were then incubated with two primary antibody solutions, mouse anti-RUNX2 antibody (#ab76956; Abcam) in DPBS solution diluted at 1:200 v/v and rabbit anti-OCN antibody (#ab198228; Abcam) solution diluted at 1:200 v/v at 4 ºC overnight. After that, samples were washed with the washing buffer solution and treated with matching secondary antibodies Alexa

Fluor Plus 488 goat anti-mouse IgG H&L (#ab150113; Abcam) in DPBS solution diluted at 1:200 v/v and Alexa Fluor Plus 555 goat anti-rabbit IgG H&L (#ab150080; Abcam) in DPBS solution diluted at 1:200 v/v at room temperature for 2 h. Next, the specimens were washed with DPBS and incubated with DAPI in DPBS solution diluted at 1:1000 v/v at room temperature for 15 min. Finally, the samples were washed and analyzed using a fluorescence microscope.

2.12. Statistical analyses

The results were expressed as means ± standard deviations of the means. Three samples were used for all experiments unless stated otherwise. Statistical analyses were performed between scaffolds using one-way analysis of variance (ANOVA), followed by a *post hoc* Bonferroni test. Differences were considered statistically significant at $p<0.05$.

3. Results and Discussion

3.1. PLGA and PLGA-HA scaffolds

3.1.1. Printing, solvent-exchange, and porosity characterizations

While the GelMA bioink has been extensively studied and characterized in prior research [9–12], there is a notable gap in our understanding regarding the printability of the PLGA and PLGA-HA inks proposed in this study. Thus, the preliminary characterization of PLGA and PLGA-HA inks is crucial to provide insights into the material's behavior and define the parameters necessary for a posterior coextrusion. The rheological results of the PLGA and PLGA-HA inks reveal critical insights into their behaviors under varying temperature conditions. In our investigation, gelation was observed during the cooling phase, indicating a thermoresponsive behavior of the inks (**Figure 2A**). This phenomenon would allow precise control over the (bio)printing process by leveraging the gelation temperature (T_{gel}). One notable finding was the composition-dependent difference in the T_{gel} between PLGA and PLGA-HA inks, which increased from 40 °C for PLGA to 46 °C for PLGA-HA. This shift in the T_{gel} may be strategically employed to tailor the ink's state during extrusion and subsequent printing.

Additionally, the observed viscosity differences between PLGA and PLGA-HA at various temperatures provided valuable information for printing optimization. PLGA-HA exhibited higher viscosity than PLGA at room temperature, with a remarkable difference of more than 40-fold (**Figure 2B**). This finding suggested that the ink's rheological response

was influenced by both temperature and composition and that PLGA-HA possessed a significantly thicker consistency at lower temperatures. Furthermore, at higher temperatures (≥ 50 °C), PLGA-HA exhibited slightly higher viscosity than PLGA. Thus, it would allow more consistency in the printability of PLGA compared to PLGA-HA. Moreover, PLGA-HA demonstrated near-Newtonian fluid behavior (~0.80 Pa.s) at 50 °C (**Figure 2C**), indicating that its viscosity was not very sensitive to changes in the shearing rate. This rheological characteristic was further advantageous for maintaining consistent flow properties during extrusion.

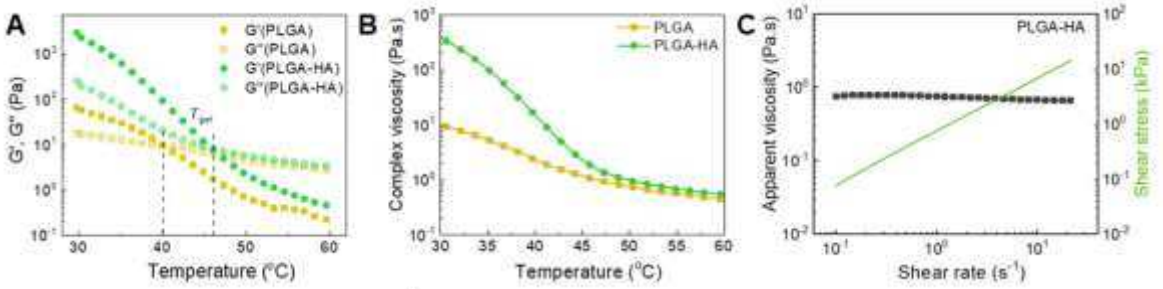

Figure 2. Rheological characterizations of PLGA and PLGA-HA inks. A) Shear storage moduli (G') and loss moduli (G") as a function of temperature at 1 Hz of frequency. B) Temperature-dependent complex viscosities of the inks. C) Apparent viscosity as a function of shear rate and shear stress for the PLGA-HA ink at 50 °C.

Considering the rheological characteristics described, the polymeric inks of PLGA and PLGA-HA solutions/suspensions in DMSO presented printability with the parameters used (**Movie S1**). Fabricating 3D scaffolds with good shape fidelity was also possible, allowing specific objects to be printed (**Figure 3A**). To solidify the inks, deionized water was added to the PLGA and PLGA-HA scaffolds to remove the DMSO. This process led to a volume shrinkage of 27.6 ± 2.6% in PLGA and 25.2 ± 5.4% in PLGA-HA, which was found to remain constant over 96 h once the exchange was complete. The shrinkage was similar to that obtained in other 3D-printed porous structures described in the literature [26].

The use of solvent-exchange to create porosity in polymeric scaffolds has been well-reported in other works[27–29] and was also observed for our 3D-printed scaffolds (**Figure 3B**). The PLGA and PLGA-HA scaffolds featured pore sizes of 137.3 ± 56.1 µm and 103.2 ± 36.4 µm (**Figure 3C**), respectively, whereas the porosity measured was 52.4% ± 5.5% for PLGA and 57.2% ± 3.3% for PLGA-HA scaffolds (**Figure 3D**), thereby mimicking the complex porous microstructure of the bone [30]. Moreover, the 50-300 µm in diameters of the pore sizes can facilitate nutrient and cell infiltration, vascularization, as well as

osteoinduction throughout the scaffolds, essential for bone regeneration [28,31–33]. Overall, the porosities attained through the solvent-exchange procedure here are a vital attribute that enhances the suitability of these polymeric scaffolds as bone grafts.

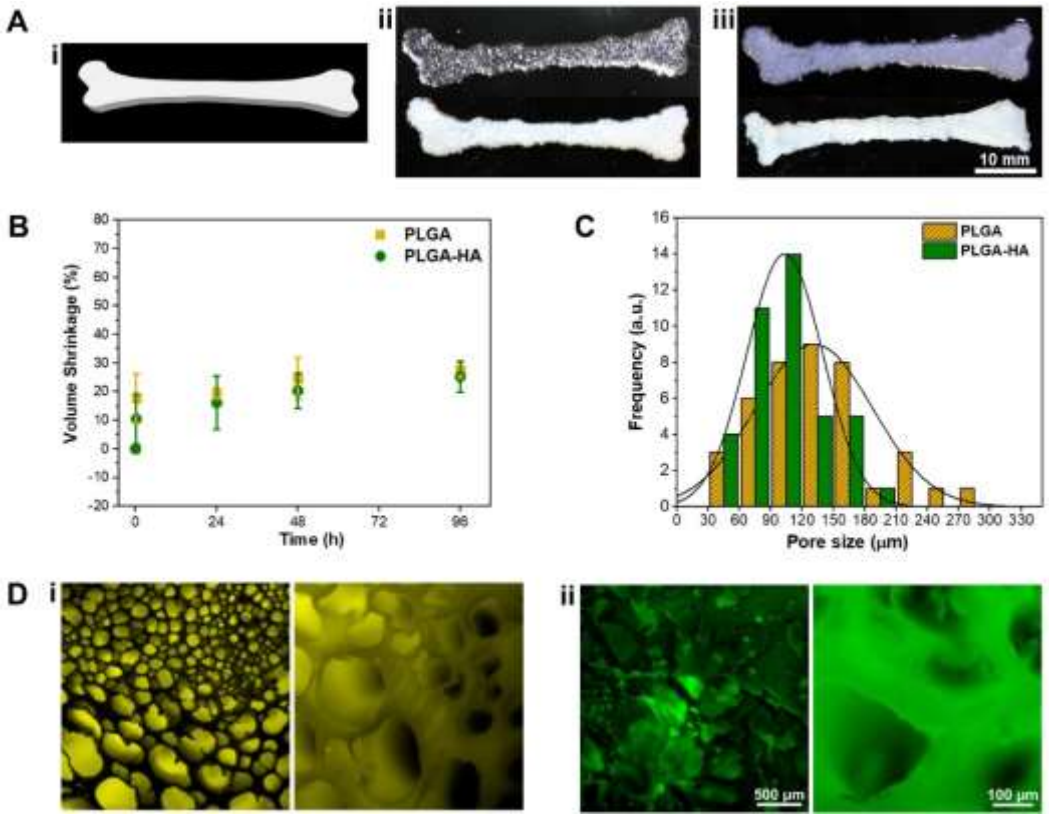

Figure 3. Characterizations of 3D-printed porous PLGA scaffolds. A) (i) Computer-aided design of a bone model; (ii) PLGA scaffold after printing (top) and after 24 h of solvent-exchange (bottom); (iii) PLGA-HA scaffold after printing (top) and after 24 h of solvent-exchange (bottom). B) Volume-shrinkage values of PLGA and PLGA-HA scaffolds (n=3). C) Quantified pore-size histograms of PLGA and PLGA-HA scaffolds (n=20). D) Fluorescence micrographs of (i) PLGA and (ii) PLGA-HA scaffolds; The images were intentionally pseudo-colored to differentiate the two scaffold types.

3.1.2. Solvent-removal and scaffold degradation

The tensile properties of bulk polymeric scaffolds (**Figure 4A**) were used to investigate the DMSO-removal in water over different time points (**Figure 4B**). After 15 min of immersion in water, DMSO still remained among the polymeric chains of PLGA and PLGA-HA scaffolds. This could be noticed by the low tensile strengths at break of both the PLGA and PLGA-HA scaffolds of 0.24 ± 0.02 MPa and 0.05 ± 0.03 MPa, respectively, at this time (**Figure 4C**). Meanwhile, moduli of elasticity (**Figure 4D**) and strains at break (**Figure 4E**)

were also low. After 24 h, the mechanical properties (tensile strengths at break, strains at break, and moduli of elasticity) increased expressively and remained largely constant, suggesting that water successfully removed the majority, if not all, DMSO from the PLGA and PLGA-HA scaffolds. At the end of 336 h, the ultimate tensile strengths obtained were 0.52 ± 0.05 MPa for PLGA and 0.41 ± 0.16 MPa for PLGA-HA, showing significant differences from the values at the initial time point. The increase of mechanical strengths for the scaffolds after DMSO-exchange by water was also reported in other works [34].

To ensure that there was minimum DMSO left in the polymer, we examined the chemical signatures of PLGA and PLGA-HA scaffolds after 24 h of immersion in water using FTIR spectroscopy. The primary chemical bonds of PLGA were identified for PLGA and PLGA-HA at 2995 cm^{-1} and 2945 cm^{-1} (C-H stretching), 1748 cm^{-1} (C=O stretching), 1450 cm^{-1}, 1385 cm^{-1}, and 1358 cm^{-1} (C-H bending), and 1179 cm^{-1} and 1084 cm^{-1} (C-O-C ester group stretching) [35]. Moreover, the presence of HA nanoparticles in the PLGA-HA scaffold could be confirmed by the phosphate group (PO_4^{3-}) peaks, mainly with the band increase at 1040 cm^{-1} [36]. Meanwhile, some DMSO bands, such as that at 2910 cm^{-1} (C-H stretching), were not observed in PLGA or PLGA-HA scaffolds at this time of solvent-exchange [37]. Therefore, the solvent-exchange process at 24 h successfully removed the DMSO from the scaffolds, which is essential [12], as the technology is later translated for the multimaterial coextrusion with the cell-laden bioink.

The *in vitro* degradation of the scaffolds was also evaluated over 12 weeks (**Figure 4G**). At 2 weeks, the weight losses were 4.8% ± 0.7% for P and 5.9% ± 0.3% for PLGA-HA scaffolds. Afterward, the degradation rates became roughly constant for the next 10 weeks, with 6.3% ± 1.0% and 7.6%± 0.7% of mass losses for PLGA and PLGA-HA scaffolds, respectively. The mechanical properties analyzed after 336 h in water were constant, indicating that the hydrolytic degradation did not noticeably affect the scaffold strengths during this period. The degradation profile of the scaffolds should be analyzed to ensure that they can meet the requirements for the intended applications while the tissues are being restored. Our results suggested that the weight losses of the scaffolds were not substantial over 12 weeks assessed, showing their good stability for bone regeneration.

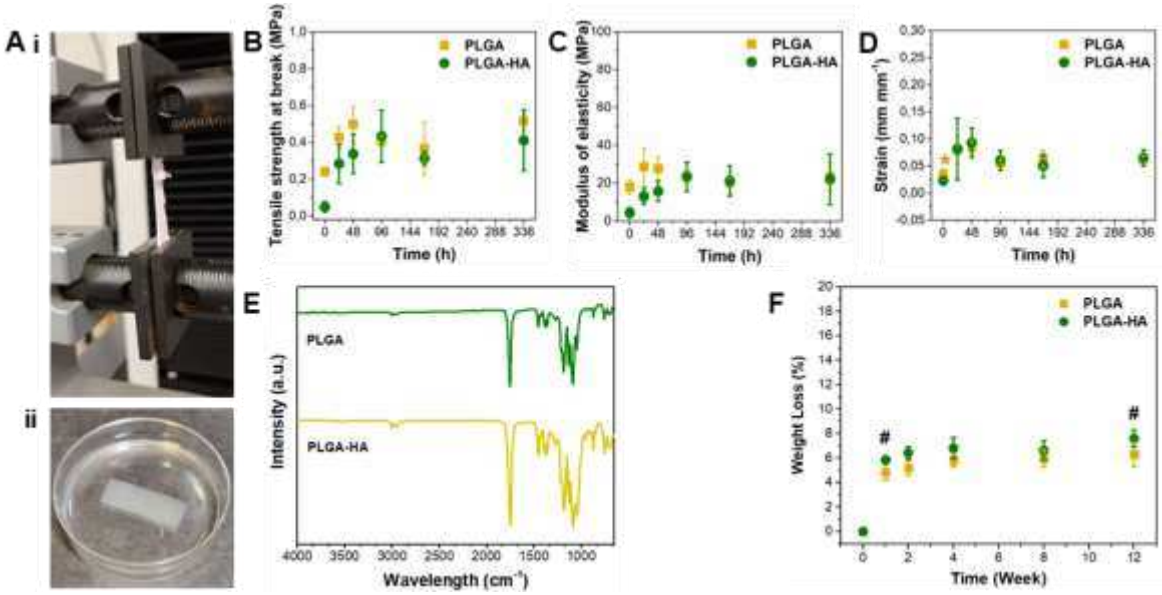

Figure 4. Tensile properties and chemical analyses of solvent-removal, and degradation of PLGA scaffolds. A) i) Photograph showing the tensile test apparatus with the PLGA sample. ii) Photograph showing a typical sample used for the tensile test during solvent-exchange process. B) Tensile strengths at break, C) moduli of elasticity, and D) strains at break of PLGA and PLGA-HA scaffolds at different time points of solvent-exchange. E) FTIR spectra of PLGA and PLGA-HA scaffolds after 24 h of solvent-exchange. F) Degradation profiles of PLGA and PLGA-HA scaffolds. *p<0.05 at different times; #p<0.05 between different scaffolds (n=3).

3.2. Multimaterial coextrusion of PLGA or PLGA-HA with GelMA

3.2.1. Printability and mechanical properties of scaffolds

In this study, we performed multimaterial coextrusion (bio)printing to fabricate the scaffolds for bone regeneration. We employed a parallel needle-enabled system to coextrude PLGA-based inks and the GelMA bioink (**Figure 5A**). The pneumatic operation was utilized to simultaneously apply the different pressures needed to both syringe extruders containing the ink and bioink, allowing for precise control of the extrusion process. Before coextrusion, the GelMA bioink's rheological properties were assessed to understand its printability (**Figure A1**), showing a T_{gel} at 30 ºC with a slightly shear thinning behavior (0.24-0.08 Pa.s). Considering the rheological properties obtained for the PLGA and PLGA-HA inks and the GelMA bioink, it was possible to identify the best temperature and parameters for the coextrusion (bio)printing. As a result, the PLGA or PLGA-HA ink and the GelMA bioink were successfully co-printed with specific arbitrary designs, such as the grid pattern as a demonstration (**Figure 5B**). This method enables the simultaneous coextrusion of diverse materials, allowing for a seamless integration of the polymer and hydrogel components

within the same (bio)printing process. However, precise control over (bio)printing parameters such as pressures, flow rates, and distance between nozzles and the platform can be challenging. Deviations in these parameters during the (bio)printing process can affect the morphology and uniformity of the prints as well as the binding between the filaments. Therefore, improving distance control and ensuring synchronization between the two channels are necessary to achieve more integrated structures, and can be further optimized in the future.

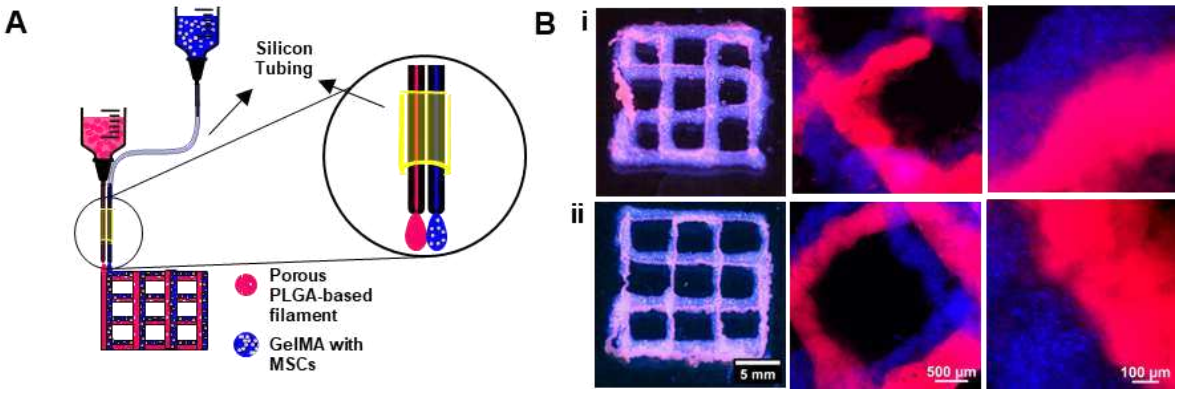

Figure 5. Multimaterial coextrusion of the PLGA or PLGA-HA ink with the GelMA bioink. A) Scheme showing multimaterial coextrusion of the PLGA or PLGA-HA ink and the GelMA bioink. B) i) Photograph and micrographs showing a representative coextruded PLGA/GelMA scaffold; ii) Photograph and micrographs showing a representative coextruded PLGA-HA/GelMA scaffold. Rhodamine (pink) was used to dye the PLGA and PLGA-HA filaments, and fluorescent blue paint was used to dye GelMA.

The lap-shear test was used to investigate the bond between the coextruded PLGA and GelMA (**Figure A2**), allowing a quantitative assessment of the bonding strength between the layers showing a lap-shear stress of 9.3 kPa. Notably, post-test observations revealed the presence of residual GelMA on the surface of PLGA, indicative of the bonding at the interface. In addition, the interfacial morphology was evaluated in more detail (**Figure A3**), validating the intimate bonding relationship between the two materials, further supporting the effectiveness of the PLGA-GelMA interaction during the coextrusion process.

To analyze the mechanical behaviors of the (bio)printed grafts, compressive tests were performed on the scaffolds of PLGA or PLGA-HA ink coextruded with the GelMA bioink, *i.e.*, PLGA/GelMA or PLGA-HA/GelMA, respectively, and compared to pure GelMA and pure PLGA scaffolds. During the experiment, the coextruded PLGA or PLGA-HA layer and

GelMA remained structurally bound under compressive stress (**Figure 6A**), highlighting the robustness of the multimaterial printing approach and its capacity to maintain structural integrity. The mechanical properties of the PLGA/GelMA and PLGA-HA/GelMA scaffolds were significantly higher than those of the pure GelMA scaffolds and were equivalent to those for pure PLGA and PLGA-HA scaffolds (no statistical differences) (**Figure 6B**). The compressive moduli of the multimaterial coextruded scaffolds, PLGA/GelMA (53.0 ± 8.0 MPa) and PLGA-HA/GelMA (65.6 ± 4.8 MPa) were more than 100 times the modulus of GelMA alone (0.4 ± 0.1 MPa) (**Figure 6C**). Moreover, the GelMA scaffolds failed at the strain of 49.2 ± 11.1%, while the PLGA (81.4 ± 2.3%), PLGA-HA (93.8 ± 9.2%), PLGA/GelMA (99.5 ± 3.2%), and PLGA-HA/GelMA (91.4 ± 1.8%) scaffolds were almost entirely compressed without failing (**Figure 5D**).

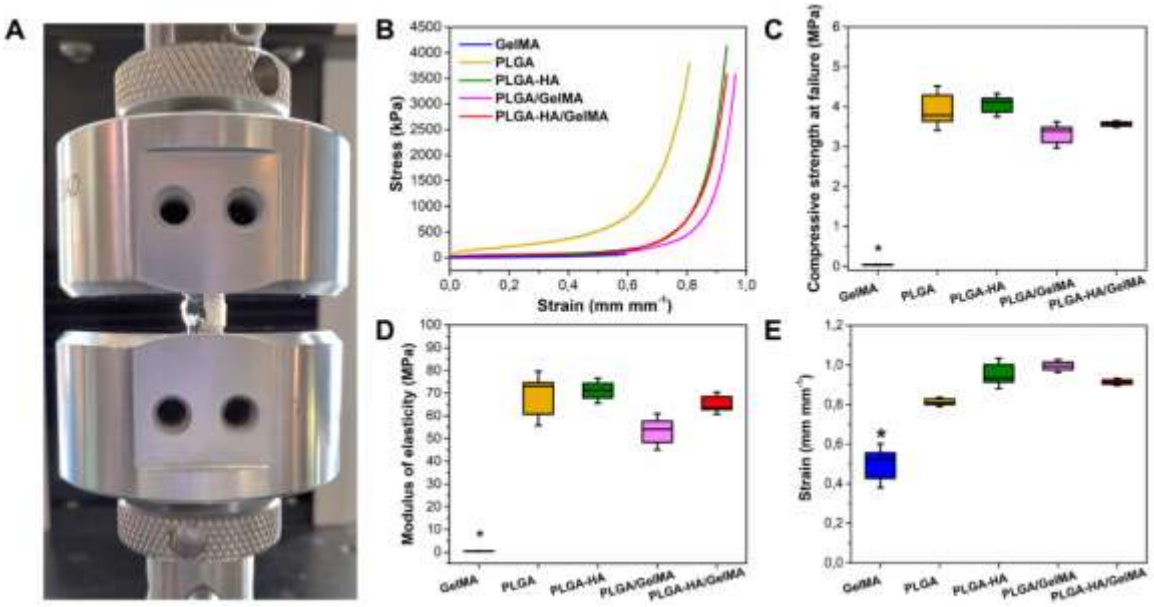

Figure 6. Compression tests of the multimaterial coextruded scaffolds. A) Compressive test apparatus for mechanical analyses of the 3D-(bio)printed scaffolds. B) Representative stress *vs.* strain curves of the compressive tests. C) Compressive strengths at failure of the scaffolds. D) Compressive moduli of elasticity of the scaffolds. E) Strains at failure of the scaffolds. *p<0.05 (n=3).

Meanwhile, the compressive strengths of PLGA/GelMA and PLGA-HA/GelMA scaffolds were measured at 3.3 ± 0.6 MPa for PLGA/GelMA and 3.6 ± 0.1 MPa for PLGA-HA/GelMA (**Figure 6E**), almost 100 times higher than that of GelMA-only (0.03 ± 0.01 MPa). Therefore, the multimaterial coextrusion strategy reported here with the hydrogel bioink and the synthetic polymer ink printed simultaneously was shown to efficiently

enhance the mechanical properties of (bio)printed grafts. The mechanical properties obtained were also higher than other alternative methods utilized, such as increasing the concentration of GelMA (compressive modulus of elasticity lower than 30 kPa) [38] or adding HA directly to the hydrogels (compressive strength at failure lower than 0.3 MPa) [16]. The compressive strength obtained for the 3D-(bio)printed composite scaffolds was comparable to those attainable with the scaffolds purely based on synthetic polymers, making them suitable for applications relating to the trabecular bone [39].

3.3. MSC viability and proliferation after multimaterial coextrusion

MSCs have been widely studied for their potential in bone tissue engineering and regenerative medicine [40]. One of the critical challenges in bioprinting is guaranteeing MSCs' viability and proliferation during their culture process. MSCs were added to the GelMA bioink and bioprinted in conjunction with the PLGA ink through the optimized coextrusion process. The viability of the MSCs was monitored over 1, 3, 7, and 14 days to assess the impacts of the multimaterial coextrusion process as well as solvent-exchange on the cells. In both configurations (PLGA/GelMA and PLGA-HA/GelMA), PLGA and PLGA-HA filaments were visible in the images due to their autofluorescence in red, while GelMA was the parallel filament containing the cells (**Figure 7A**).

The results showed that the 3D-(bio)printed PLGA/GelMA and PLGA-HA/GelMA grafts slightly reduced cell viability on day 1 compared to the bioprinted GelMA hydrogels alone (**Figure 7B**). This observation might have been an effect of the remaining DMSO from the coextruded polymeric filaments on the cells. Although DMSO is relatively bearable to cells, it can still affect cell viability depending on the solvent concentration [20]. However, at day 3, cell viability was already equivalent to the GelMA-alone group with no statistical differences. Additionally, the ratios between live/dead cells were constant over time, with no significant differences in cell viability up until 14 days analyzed among GelMA (75.5 ± 5.4%), PLGA/GelMA (75.4 ± 2.7%), and PLGA-HA/GelMA (77.5 ± 6.2%).

The proliferation of MSCs was further evaluated for all the (bio)printed scaffolds. The MTS analysis was used to correlate the activity of mitochondrial enzymes after MTS conversion with the number of living cells to quantify the proliferation over 1, 3, 7, and 14 days (**Figure 7C**). The results revealed that the proliferation of MSCs significantly reduced on day 3 for the PLGA/GelMA (0.45 ± 0.13) and PLGA-HA/GelMA (0.78 ± 0.34) scaffolds compared to GelMA (1.65 ± 0.25). This reduction might have occurred, again, due to the

presence of residual DMSO within the culture medium at the initial time points. However, after 7 and 14 days, MSC proliferation in the coextruded scaffolds presented similar cellular metabolic activities compared to GelMA-alone, with no statistical differences. Therefore, the data suggested that using coextrusion-enabled multimaterial 3D-(bio)printed PLGA/GelMA or PLGA-HA/GelMA scaffolds for MSC culture could provide an appropriate microenvironment for cell proliferation.

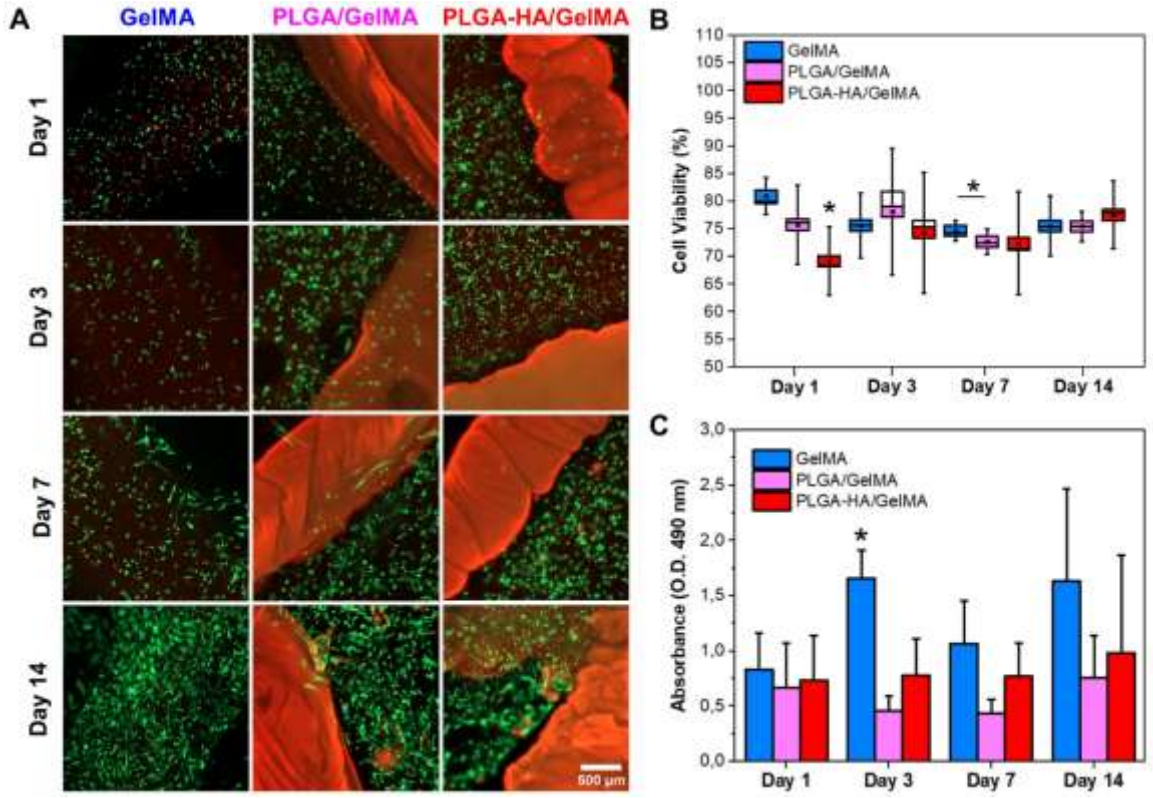

Figure 7. MSC viability and proliferation in 3D-(bio)printed PLGA/GelMA and PLGA-HA/GelMA scaffolds compared to those in pure GelMA scaffolds. A) Live (green)/dead (red) assay of MSCs directly bioprinted with the GelMA portions of the scaffolds (n=3). B) MSC viability values measured by the ratio between live/dead cells in the bioprinted GelMA portions of the scaffolds. C) Proliferation profiles of MSCs in the bioprinted GelMA portions of the scaffolds measured by the MTS assay. *p<0.05 denotes a significant difference between (bio)printed scaffolds.

The morphologies of MSCs on the 3D-(bio)printed PLGA/GelMA and PLGA-HA/GelMA scaffolds were also examined and compared to the GelMA-alone control for 1, 3, 7, and 14 days (**Figure 8**). Again, the printed PLGA and PLGA-HA filaments were visible in blue due to their autofluorescence, parallel with the cell-containing GelMA filament (**Figure A4**), showing the long-lasting bind between the filaments during the 14 days. An interesting observation was that, in the PLGA/GelMA and PLGA-HA/GelMA scaffolds, the

cells did not only grow inside the GelMA hydrogel filaments, but we could also find the cells populating the surfaces of the PLGA and PLGA-HA filaments, indicating interactions between the hydrogel and polymeric components in these composite configurations.

The cell morphologies changed throughout the culture period according to the type of the (bio)printed scaffolds. For the 1st day, the cells in all the scaffolds exhibited a rounded and compact morphology with a higher nucleus-to-cytoplasm ratio (**Figure 8A**). This is expected as the cells adapt to the new microenvironment they were cultured in. After 3 days, some MSCs encapsulated in bioprinted pure GelMA showed a spindle-shaped morphology with more elongated cells, which can be verified by the cell area measurements (**Figure 8B**). However, most MSCs cultured within the GelMA filaments in PLGA/GelMA and PLGA-HA/GelMA scaffolds still exhibited a rounded morphology. This result was in accordance with cell viability and proliferation results, showing that the cells were possibly still subjected to the stress caused by the initial solvent-removal process, thus presenting a compact shape. On day 7, nevertheless, the MSCs in PLGA-HA/GelMA started to assume an elongated morphology, while PLGA/GelMA did not yet present spreading cells. It has been well-reported that HA nanoparticles can promote the expression of cytoskeletal proteins, such as actin filaments [41], which may have influenced the cell shape in this phase for the PLGA-HA/GelMA scaffolds. Finally, on day 14, the MSCs spread their cytoplasm in all the (bio)printed scaffolds and better-adapted to the 3D microstructure of the GelMA and PLGA-HA/GelMA scaffolds.

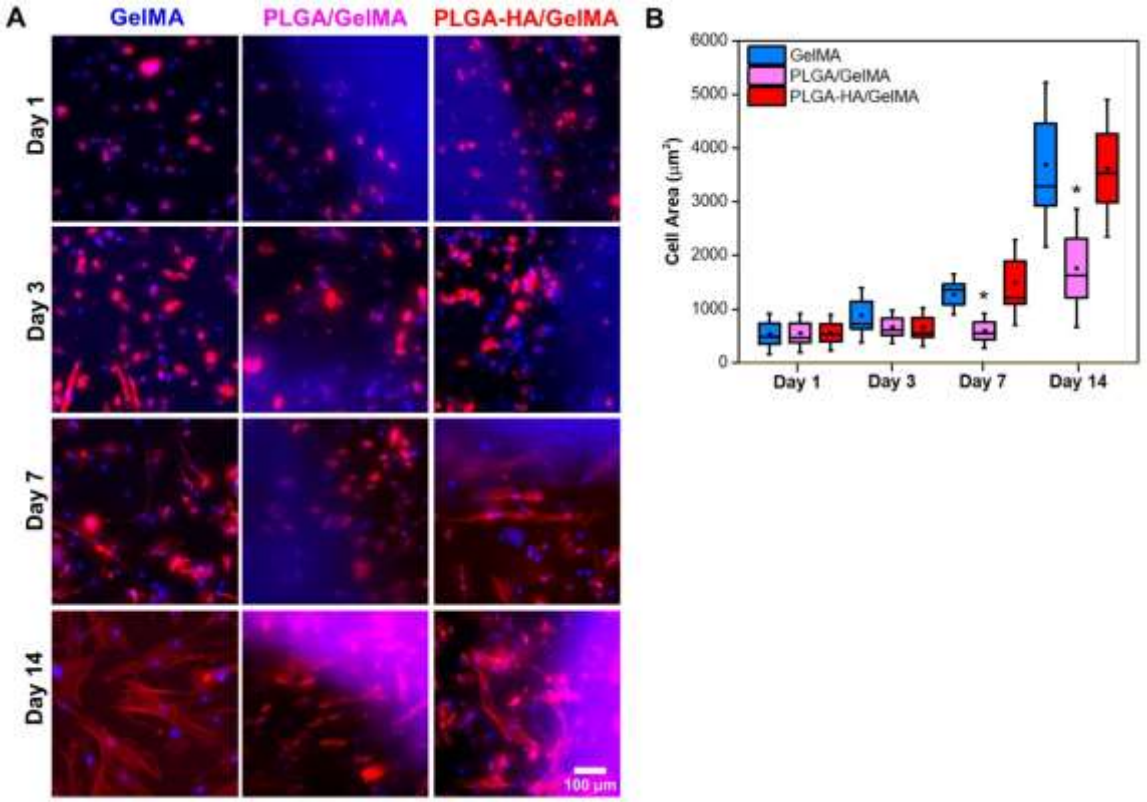

Figure 8. MSC spreading in (bio)printed GelMA, PLGA/GelMA, and PLGA-HA/GelMA scaffolds. A) Fluorescence images of cell morphologies using phalloidin (red) to identify the cytoskeleton and DAPI (blue) for the nuclei (n=3). B) Cell area measurements in the (bio)printed scaffolds (n=20). *$p<0.05$ denotes a significant difference between (bio)printed scaffolds.

3.4. Differentiation of MSCs in the (bio)printed scaffolds

The differentiation of MSCs into osteoblasts is critical for the fabricated scaffolds used towards bone applications. If MSCs can successfully differentiate, the approach may then be translated in the future to stem cells derived from patients being cultured and differentiated for specific application scenarios in a personalizable manner. According to the literature, the morphology of the MSCs during the differentiation into osteoblasts can vary depending on the culture conditions and stage of differentiation. The osteogenic differentiation process is typically from the elongated morphology of undifferentiated MSCs to a cuboidal shape, ultimately to mature osteoblasts' stellate shape [42] The morphologies observed for the (bio)printed scaffolds in different configurations all showed the elongated cells after 14 days of proliferation and 1 week of differentiation, starting to differentiate into more prominent cytoplasm, characteristic of the cuboidal-shaped cells, primarily observed

at week 2; eventually, a stellate-like morphology at week 4 of differentiation was visible (**Figure A5**).

In addition to the changes in cellular morphology, the expressions of two key osteogenic differentiation markers – Runt-related transcription factor 2 (Runx2) and osteocalcin (OCN) – were finally evaluated (**Figure 9A**). The Runx2 protein is expressed during the early stages of osteogenic differentiation [38], indicating the commitment of MSCs to the osteoblast lineage. In addition, Runx2 is known for regulating the expression of other crucial genes for bone formation, such as OCN. OCN is a protein produced by mature osteoblasts in the final stages of differentiation that is important for the mineralization of the bone [43]. The results suggested higher expression of both Runx2 and OCN in MSCs since week 1 of differentiation in the (bio)printed PLGA-HA/GelMA scaffolds (**Figure 9B-C**). These expressions were significantly higher when compared to those for cells in the PLGA/GelMA scaffolds. This observation indicated that HA nanoparticles in the PLGA-HA filaments of the PLGA-HA/GelMA grafts likely promoted the osteogenic differentiation of MSCs. Ultimately, the MSCs in all the scaffolds differentiated, producing both markers by the end of week 4 of differentiation.

Overall, the data suggested the potential of multimaterial 3D coextrusion (bio)printing in developing scaffolds that could support the growth and differentiation of MSCs over an extended period. However, more research is needed to optimize the processing conditions for optimal cell growth and differentiation. In addition, using HA as a bioactive additive could be a valuable approach to promoting osteogenic differentiation of MSCs, as widely reported. Nevertheless, future studies should evaluate the bone regeneration efficacy of the multimaterial (bio)printed scaffolds in vivo to ensure its translational applicability.

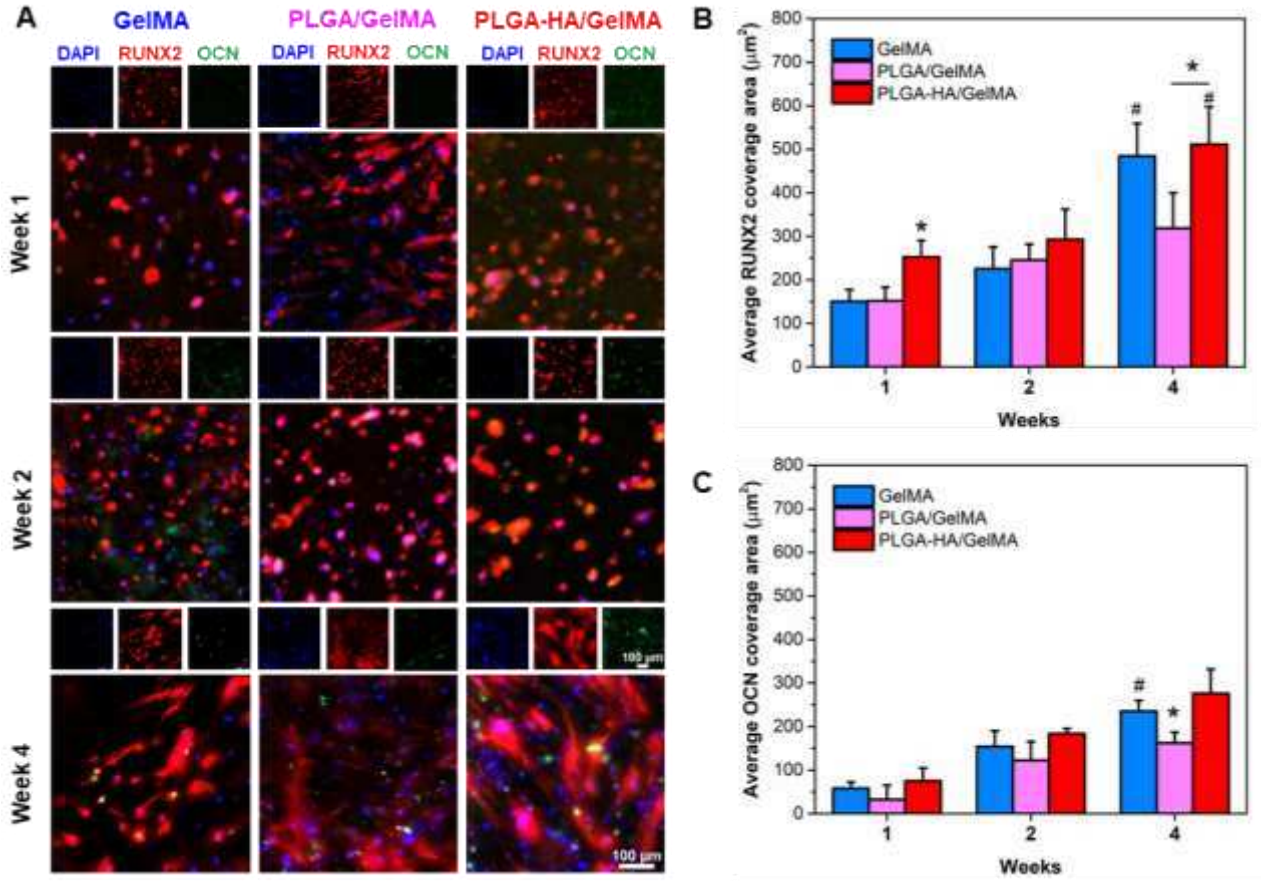

Figure 9. Osteogenic differentiation of MSCs in 3D-(bio)printed GelMA, PLGA/GelMA, and PLGA-HA/GelMA scaffolds. A) Immunostaining images with RUNX2 (red) and OCN (green) biomarkers of MSCs at 1, 2, and 4 weeks following osteogenic differentiation. B) Quantification results of RUNX2 by average cell coverage area. C) Quantification results of OCN by average cell coverage area. *$p<0.05$ denotes a significant difference between (bio)printed scaffolds and #$p<0.05$ at different times; two-way ANOVA (n=3).

4. Conclusions

In this work, PLGA or PLGA-HA ink was printed simultaneously with the MSC-laden GelMA bioink using a unique multimaterial coextrusion process. The significance of this novel approach is the ability to achieve (bio)printing efficiency with simultaneous biological and mechanical functionality. The microstructure of the printed PLGA filaments was examined, showing porosity and pore sizes in the same range of trabecular bone formed *via* solvent-exchange by removing DMSO from the prints. Of note, the rheological properties of both the polymer inks and the GelMA bioink were evaluated, and the multimaterial

coextrusion showed good printability of both. The PLGA-based layer showed interfacial bonding to GelMA. The compressive properties of the (bio)printed composite scaffolds were significantly higher when compared to pure GelMA despite still inferiority to the native bones, and thus, the strategy is deemed promising for non-load-bearing bone applications. Importantly, the study showed that the coextruded composite scaffolds exhibited similar results in MSC viability, proliferation, and morphology within the GelMA portions compared to the bioprinted GelMA alone, suggesting the cytocompatibility of the method. Finally, the differentiation analyses revealed that osteogenic differentiation of the MSCs was enhanced with the presence of HA in the PLGA filaments, further validating the potential of these multimaterial, multiscale composite structures for promoting cellular behaviors for tissue engineering applications.

Declaration of Interests

YSZ consulted for Allevi by 3D Systems, and sits on the scientific advisory board and holds options of Xellar, neither of which however, participated in or bias the work.

Acknowledgments

This work was supported by FAPESP, grants #2020/14679-9, #2020/07923-0, and #2023/11076-0, São Paulo Research Foundation, and Brigham Research Institute. The authors would like to thank the Electronic Packaging staff of the Information Technology Center (CTI Renato Archer), the Evonik Corporation (Piscataway, NJ, USA) for providing a polymer sample, and the Zhang Laboratory team, especially Sushila Maharjan, Liming Lian, and Carlos-Ezio Garciamendez-Mijares, for the valuable insights. Isabella C. P. Rodrigues was also supported by Fulbright with the Doctoral Dissertation Research Award.

References

[1] Wu AM, Bisignano C, James SL, Abady GG, Abedi A, Abu-Gharbieh E, et al. Global, regional, and national burden of bone fractures in 204 countries and territories, 1990–2019: a systematic analysis from the Global Burden of Disease Study 2019. Lancet Healthy Longev 2021;2:e580–92. https://doi.org/10.1016/S2666-7568(21)00172-0.

[2] Wang X, Xu S, Zhou S, Xu W, Leary M, Choong P, et al. Topological design and additive manufacturing of porous metals for bone scaffolds and orthopaedic implants: A review. Biomaterials 2016;83:127–41. https://doi.org/10.1016/j.biomaterials.2016.01.012.

[3] Madrid APM, Vrech SM, Sanchez MA, Rodriguez AP. Advances in additive manufacturing for bone tissue engineering scaffolds. Materials Science and Engineering C 2019;100:631–44. https://doi.org/10.1016/j.msec.2019.03.037.

[4] Murphy S V., Atala A. 3D bioprinting of tissues and organs. Nat Biotechnol 2014;32:773–85. https://doi.org/10.1038/nbt.2958.
[5] Zhu K, Chen N, Liu X, Mu X, Zhang W, Wang C, et al. A General Strategy for Extrusion Bioprinting of Bio-Macromolecular Bioinks through Alginate-Templated Dual-Stage Crosslinking. Macromol Biosci 2018;18:1–8. https://doi.org/10.1002/mabi.201800127.
[6] Hölzl K, Lin S, Tytgat L, van Vlierberghe S, Gu L, Ovsianikov A. Bioink properties before, during and after 3D bioprinting. Biofabrication 2016;8. https://doi.org/10.1088/1758-5090/8/3/032002.
[7] Zhang YS, Khademhosseini A. Advances in engineering hydrogels. Science (1979) 2017;356. https://doi.org/10.1126/SCIENCE.AAF3627/ASSET/FF981CF9-F818-45D8-A693-CA10D4ABEE12/ASSETS/GRAPHIC/356_AAF3627_F5.JPEG.
[8] Shen Y, Cao X, Lu M, Gu H, Li M, Posner DA, et al. Current treatments after spinal cord injury: Cell engineering, tissue engineering, and combined therapies. Smart Medicine 2022;1:e20220017. https://doi.org/10.1002/SMMD.20220017.
[9] Ying G-LL, Jiang N, Maharjan S, Yin Y-XX, Chai R-RR, Cao X, et al. Aqueous Two-Phase Emulsion Bioink-Enabled 3D Bioprinting of Porous Hydrogels. Advanced Materials 2018;30:1–9. https://doi.org/10.1002/adma.201805460.
[10] Loessner D, Meinert C, Kaemmerer E, Martine LC, Yue K, Levett PA, et al. Functionalization, preparation and use of cell-laden gelatin methacryloyl-based hydrogels as modular tissue culture platforms. Nat Protoc 2016;11:727–46. https://doi.org/10.1038/nprot.2016.037.
[11] Nichol JW, Koshy ST, Bae H, Hwang CM, Yamanlar S, Khademhosseini A. Cell-laden microengineered gelatin methacrylate hydrogels. Biomaterials 2010;31:5536–44. https://doi.org/10.1016/j.biomaterials.2010.03.064.
[12] Liu W, Zhong Z, Hu N, Zhou Y, Maggio L, Miri AK, et al. Coaxial extrusion bioprinting of 3D microfibrous constructs with cell-favorable gelatin methacryloyl microenvironments. Biofabrication 2018;10:24102. https://doi.org/10.1088/1758-5090/aa9d44.
[13] Wang Y, Kankala RK, Zhu K, Wang S-B, Zhang YS, Chen A-Z. Coaxial Extrusion of Tubular Tissue Constructs Using a Gelatin/GelMA Blend Bioink. ACS Biomater Sci Eng 2019;5:5514–24. https://doi.org/10.1021/ACSBIOMATERIALS.9B00926.
[14] Critchley S, Sheehy EJ, Cunniffe G, Diaz-Payno P, Carroll SF, Jeon O, et al. 3D printing of fibre-reinforced cartilaginous templates for the regeneration of osteochondral defects. Acta Biomater 2020;113:130–43. https://doi.org/10.1016/J.ACTBIO.2020.05.040.
[15] Ko YG, Kwon OH. Reinforced gelatin-methacrylate hydrogels containing poly(lactic-co-glycolic acid) nanofiber fragments for 3D bioprinting. Journal of Industrial and Engineering Chemistry 2020;89:147–55. https://doi.org/10.1016/j.jiec.2020.04.021.
[16] Song P, Li M, Zhang B, Gui X, Han Y, Wang L, et al. DLP fabricating of precision GelMA/HAp porous composite scaffold for bone tissue engineering application. Compos B Eng 2022;244:110163. https://doi.org/10.1016/J.COMPOSITESB.2022.110163.
[17] Kundu J, Shim JH, Jang J, Kim SW, Cho DW. An additive manufacturing-based PCL-alginate-chondrocyte bioprinted scaffold for cartilage tissue engineering. J Tissue Eng Regen Med 2015;9:1286–97. https://doi.org/10.1002/TERM.1682.
[18] Diaz-Gomez L, Elizondo ME, Koons GL, Diba M, Chim LK, Cosgriff-Hernandez E, et al. Fiber engraving for bioink bioprinting within 3D printed tissue engineering scaffolds. Bioprinting 2020;18:e00076. https://doi.org/10.1016/j.bprint.2020.e00076.
[19] Zamani Y, Mohammadi J, Amoabediny G, Helder MN, Zandieh-Doulabi B, Klein-Nulend J. Bioprinting of Alginate-Encapsulated Pre-osteoblasts in PLGA/β-TCP Scaffolds

Enhances Cell Retention but Impairs Osteogenic Differentiation Compared to Cell Seeding after 3D-Printing. Regen Eng Transl Med 2020. https://doi.org/10.1007/s40883-020-00163-1.
[20] Luo Z, Tang G, Ravanbakhsh H, Li W, Wang M, Kuang X, et al. Vertical Extrusion Cryo(bio)printing for Anisotropic Tissue Manufacturing. Advanced Materials 2021:2108931. https://doi.org/10.1002/ADMA.202108931.
[21] Lian L, Zhou C, Tang G, Xie M, Wang Z, Luo Z, et al. Uniaxial and Coaxial Vertical Embedded Extrusion Bioprinting. Adv Healthc Mater 2021:2102411. https://doi.org/10.1002/ADHM.202102411.
[22] Ma HL, Li W, Wang M, Varanda LC, Perussi JR, Zhang YS, et al. In vitro 3D malignant melanoma model for the evaluation of hypericin-loaded oil-in-water microemulsion in photodynamic therapy. Biodes Manuf 2022;5:660–73. https://doi.org/10.1007/S42242-022-00202-6/FIGURES/7.
[23] Liu Q, Mille LS, Villalobos C, Anaya I, Vostatek M, Yi S, et al. 3D-bioprinted cholangiocarcinoma-on-a-chip model for evaluating drug responses. Biodes Manuf 2023;6:373–89. https://doi.org/10.1007/S42242-022-00229-9/FIGURES/7.
[24] Schneider CA, Rasband WS, Eliceiri KW. NIH Image to ImageJ: 25 years of image analysis. Nature Methods 2012 9:7 2012;9:671–5. https://doi.org/10.1038/nmeth.2089.
[25] Zou L, Hu L, Pan P, Tarafder S, Du M, Geng Y, et al. Icariin-releasing 3D printed scaffold for bone regeneration. Compos B Eng 2022;232:109625. https://doi.org/10.1016/J.COMPOSITESB.2022.109625.
[26] Liang H, Wang Y, Chen S, Liu Y, Liu Z, Bai J. Nano-Hydroxyapatite Bone Scaffolds with Different Porous Structures Processed by Digital Light Processing 3D Printing 2022. https://doi.org/10.18063/ijb.v8i1.502.
[27] Chen J, Wang Y, Liu J, Xu X. Preparation, characterization, physicochemical property and potential application of porous starch: A review. Int J Biol Macromol 2020;148:1169–81. https://doi.org/10.1016/J.IJBIOMAC.2020.02.055.
[28] Ferreira F v., Otoni CG, de France KJ, Barud HS, Lona LMF, Cranston ED, et al. Porous nanocellulose gels and foams: Breakthrough status in the development of scaffolds for tissue engineering. Materials Today 2020;37:126–41. https://doi.org/10.1016/J.MATTOD.2020.03.003.
[29] Seok JM, Rajangam T, Jeong JE, Cheong S, Joo SM, Oh SJ, et al. Fabrication of 3D plotted scaffold with microporous strands for bone tissue engineering. J Mater Chem B 2020;8:951–60. https://doi.org/10.1039/C9TB02360G.
[30] Collins MN, Ren G, Young K, Pina S, Reis RL, Oliveira JM. Scaffold Fabrication Technologies and Structure/Function Properties in Bone Tissue Engineering. Adv Funct Mater 2021;31:2010609. https://doi.org/10.1002/ADFM.202010609.
[31] Zhang Y, Liu X, Zeng L, Zhang J, Zuo J, Zou J, et al. Polymer Fiber Scaffolds for Bone and Cartilage Tissue Engineering. Adv Funct Mater 2019;29:1903279. https://doi.org/10.1002/ADFM.201903279.
[32] Zhu L, Luo D, Liu Y. Effect of the nano/microscale structure of biomaterial scaffolds on bone regeneration. International Journal of Oral Science 2020 12:1 2020;12:1–15. https://doi.org/10.1038/s41368-020-0073-y.
[33] Murugan S, Parcha SR. Fabrication techniques involved in developing the composite scaffolds PCL/HA nanoparticles for bone tissue engineering applications. J Mater Sci Mater Med 2021;32:1–10. https://doi.org/10.1007/S10856-021-06564-0/TABLES/4.
[34] Xu D, Xu T, Gao G, Xiao Y, Wang Z, Chen J, et al. Effect of solvent–matrix interactions on structures and mechanical properties of micelle-crosslinked gels. J Polym Sci B Polym Phys 2019;57:473–83. https://doi.org/10.1002/POLB.24805.

[35] Pandey N, Hakamivala A, Xu C, Hariharan P, Radionov B, Huang Z, et al. Biodegradable Nanoparticles Enhanced Adhesiveness of Mussel-Like Hydrogels at Tissue Interface. Adv Healthc Mater 2018;7:1701069. https://doi.org/10.1002/ADHM.201701069.
[36] Qian G, Fan P, He F, Ye J. Novel Strategy to Accelerate Bone Regeneration of Calcium Phosphate Cement by Incorporating 3D Plotted Poly(lactic-co-glycolic acid) Network and Bioactive Wollastonite. Adv Healthc Mater 2019;8:1801325. https://doi.org/10.1002/ADHM.201801325.
[37] Eom Y, Ju H, Park Y, Chae DW, Jung YM, Kim BC, et al. Effect of dissolution pathways of polyacrylonitrile on the solution homogeneity: Thermodynamic- or kinetic-controlled dissolution. Polymer (Guildf) 2020;205:122697. https://doi.org/10.1016/J.POLYMER.2020.122697.
[38] Wang M, Li W, Mille LS, Ching T, Luo Z, Tang G, et al. Digital Light Processing Based Bioprinting with Composable Gradients. Advanced Materials 2022;34:2107038. https://doi.org/10.1002/ADMA.202107038.
[39] Yan Y, Chen H, Zhang H, Guo C, Yang K, Chen K, et al. Vascularized 3D printed scaffolds for promoting bone regeneration. Biomaterials 2019;190–191:97–110. https://doi.org/10.1016/J.BIOMATERIALS.2018.10.033.
[40] Liu Y, Guo Q, Zhang X, Wang Y, Mo X, Wu T. Progress in Electrospun Fibers for Manipulating Cell Behaviors. Advanced Fiber Materials 2023;5:1241–72. https://doi.org/10.1007/S42765-023-00281-9/FIGURES/15.
[41] Yang X, Li Y, He W, Huang Q, Zhang R, Feng Q. Hydroxyapatite/collagen coating on PLGA electrospun fibers for osteogenic differentiation of bone marrow mesenchymal stem cells. J Biomed Mater Res A 2018;106:2863–70. https://doi.org/10.1002/JBM.A.36475.
[42] Gavazzo P, Viti F, Donnelly H, Oliva MAG, Salmeron-Sanchez M, Dalby MJ, et al. Biophysical phenotyping of mesenchymal stem cells along the osteogenic differentiation pathway. Cell Biol Toxicol 2021;37:915–33. https://doi.org/10.1007/S10565-020-09569-7/FIGURES/4.
[43] Meesuk L, Suwanprateeb J, Thammarakcharoen F, Tantrawatpan C, Kheolamai P, Palang I, et al. Osteogenic differentiation and proliferation potentials of human bone marrow and umbilical cord-derived mesenchymal stem cells on the 3D-printed hydroxyapatite scaffolds. Scientific Reports 2022 12:1 2022;12:1–19. https://doi.org/10.1038/s41598-022-24160-2.

Appendix

Multimaterial Coextrusion (Bio)printing of Composite Polymer Biomaterial Ink and Hydrogel Bioink for Tissue Fabrication

Isabella C. P. Rodrigues, Luis C. O. Clark, Xiao Kuang, Regina Sanchez, Éder S. N. Lopes, Laís P. Gabriel, Yu Shrike Zhang*

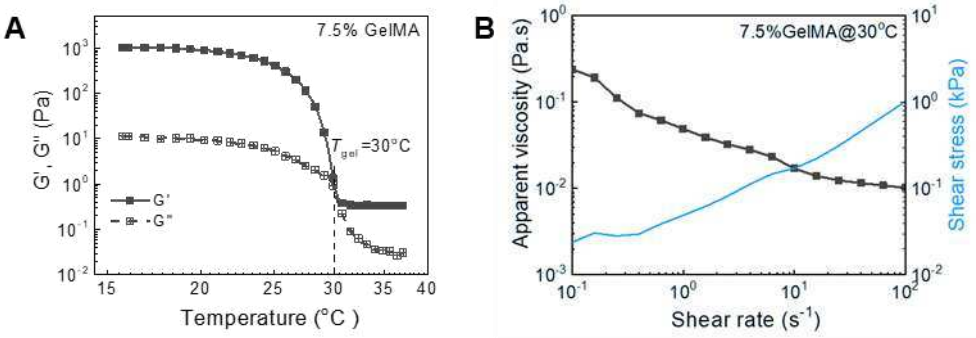

Figure A1. Characterizations of the GelMA bioink. A) Shear storage modulus (G') and loss modulus (G") as a function of temperature at 1 Hz of frequency. B) Apparent viscosity as a function of shear rate and shear stress for the GelMA bioink at 30 °C.

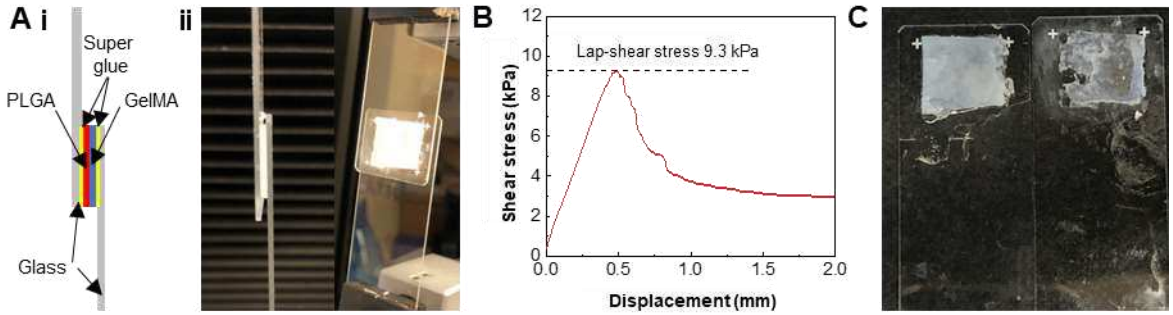

Figure A2. Characterization of bonding between PLGA and GelMA. A) i) Schematic and ii) photographs of the lap-shear test setup. B) Shear stress versus displacement curve. C) Photograph showing both glass parts with the residual bonded layers fractured in the middle after the lap-shear test.

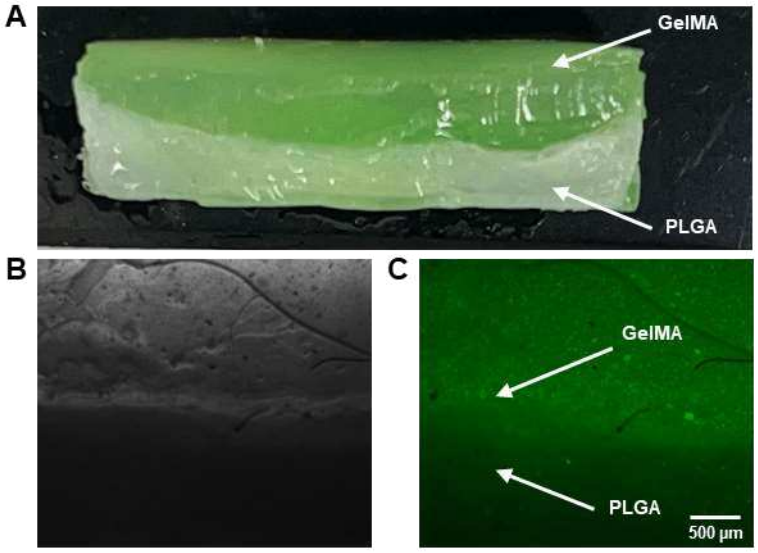

Figure A3. Characterization of the interfacial morphology between PLGA and GelMA. A) Photograph of the GelMA bonded with PLGA. B) Optical and C) fluorescence microscopic images of the interface between PLGA and GelMA. Fluorescent green paint was added to GelMA for visualization.

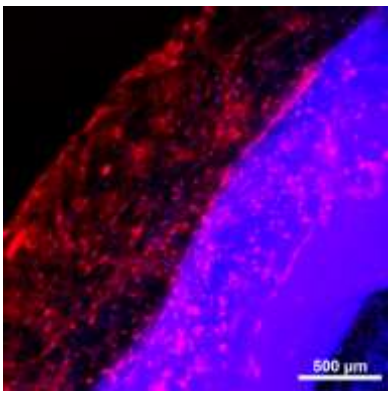

Figure A4. Coextrusion-(bio)printed PLGA-HA/GelMA scaffolds containing MSCs cultured

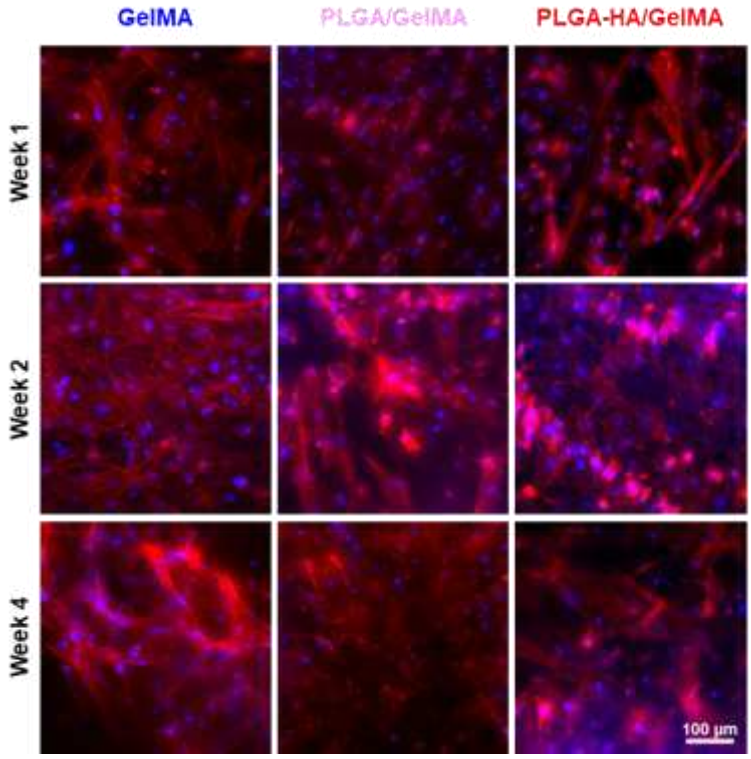

for 7 days.

Figure A5. Morphologies of MSCs during osteogenic differentiation within bioprinted GelMA, as well as coextrusion-(bio), printed PLGA/GelMA and PLGA-HA/GelMA scaffolds encapsulating MSCs cultured for 1, 2, and 4 weeks.

7 DISCUSSÃO

Os estudos envolvidos nessa tese de doutorado demonstram o potencial da rotofiação e de diferentes técnicas de MA para produzir *scaffold*s e implantes de maneira eficiente e customizada, com propriedades necessárias para promover a regeneração óssea. Dessa maneira, o foco principal está na obtenção de *scaffold*s ou implantes que contenham aditivos que estimulem os mecanismos de osseointegração (osteogênese, osteoindução e, principalmente, osteocondução), atividade antibacteriana para prevenção de osteomielite e em propriedades mecânicas e estruturais mais eficazes para aplicação óssea.

O manuscrito do artigo "Osteoconductive composite membranes produced by rotary jet spinning of bioresorbable PLGA present bioactivity for bone regeneration" apresenta resultados significativos sobre a produção e caracterização de membranas osteocondutivas produzidas por rotofiação de PLGA biorreabsorvível contendo HA(NPs), com o objetivo de investigar sua bioatividade para regeneração óssea. Inicialmente, foi determinada a concentração crítica da solução para permitir a formação das fibras, sendo esta estabelecida em 8% g/mL tanto para PLGA quanto para PLGA-HA(NPs). A análise da morfologia das membranas por MEV revelou a obtenção de fibras contínuas e homogêneas para todas as velocidades de rotação testadas, indicando estabilidade no processo de produção das fibras.

A caracterização química confirmou a presença de grupos químicos característicos do PLGA e das nanopartículas de HA nas membranas compósitas, enquanto análises térmicas permitiram avaliar quantitativamente a adição das HA(NPs) e a degradação térmica das membranas. Além da confirmação da presença das HA(NPs) nas membranas, TEM e EDS permitiram verificar sua distribuição homogênea no interior das fibras. A avaliação da bioatividade revelou a formação de apatita nas membranas contendo HA(NPs), sugerindo maior bioatividade e potencial de engenharia tecidual óssea. Adicionalmente, os ensaios de viabilidade celular demonstraram alta biocompatibilidade das membranas com células pré-osteoblásticas, permitindo a formação de monocamaca celular, sugerindo potencial de formação de tecido ósseo. Em resumo, os resultados deste estudo destacam o potencial das membranas compostas de PLGA-HA(NPs) como materiais promissores para regeneração óssea, oferecendo uma visão otimista de suas aplicações futuras na engenharia de tecidos ósseos.

O manuscrito do estudo “Implants promoting osteoconduction and local antibacterial activity for effective osseointegration and osteomyelitis prevention” aborda a produção de implantes capazes de promover osteocondução e atividade antibacteriana local para melhorar a osseointegração e prevenir a osteomielite. A morfologia dos *scaffold*s foi avaliada por MEV, demonstrando a obtenção de fibras homogêneas com diâmetros menores que 20 µm para todos os *scaffold*s produzidos. Não houve diferença significativa nos diâmetros das fibras entre os *scaffold*s de PLGA-HA e PLGA-HA-RIF, indicando que a adição de RIF não alterou a morfologia das fibras. No entanto, os *scaffold*s PLGA-COL-HA apresentaram uma redução de quase 75% no diâmetro das fibras em comparação com o PLGA-HA, resultado condizente com estudos anteriores que mostraram esse efeito após a adição de proteínas (RODRIGUES et al., 2021b).

Análises de TEM revelaram uma distribuição uniforme de HA(NPs) nas fibras, sugerindo a incorporação eficaz de HA em todos os *scaffold*s, fundamental para melhorar suas propriedades osteocondutivas. Além disso, para o *scaffold* PLGA-HA-RIF, a presença de RIF foi identificada, com partículas de RIF apresentando uma morfologia alongada, contrastando com a morfologia esférica das HA(NPs). A análise química e térmica dos *scaffold*s confirmou a presença do PLGA, COL, HA e RIF nos *scaffold*s correspondentes, através da presença dos grupos químicos no espectro e das alterações na estabilidade e degradação térmica dos *scaffold*s. A adição de COL aumentou significativamente a hidrofilicidade e degradação comparada aos outros *scaffolds*. A liberação controlada de RIF do *scaffold* de PLGA-HA-RIF foi avaliada, sendo aderente aos modelos de liberação controlada com mecanismo de difusão de Fick predominante, indicando uma liberação gradual e constante do fármaco ao longo do tempo, benéfico para aplicações em implantes ósseos, reduzindo possível toxicidade celular inerente do antibiótico.

Além disso, estruturas de Ti6Al4V com diferentes tamanhos de poros foram projetadas e fabricadas utilizando MA pela técnica de PBF-EB. Os resultados dos testes de compressão indicaram uma redução na resistência à compressão e rigidez dos implantes com o aumento do tamanho do poro O tamanho de poro equivalente a 450 µm demonstrou morfologia e propriedades mecânicas adequadas para aplicações ósseas. A avaliação da atividade antibacteriana dos *scaffold*s e implantes demonstrou a eficácia do RIF contra *Escherichia coli* e *Staphylococcus aureus*, indicando uma inibição sensível da *S. aureus*. A capacidade osteocondutiva dos *scaffold*s foi confirmada pela formação de apatita em sua superfície após incubação em fluido corporal simulado, indicando sua promissora aplicabilidade para

osseointegração. Além disso, os *scaffold*s e implantes demonstraram alta viabilidade de pré-osteoblastos, promovendo a adesão e proliferação celular. Em suma, os resultados deste estudo mostram que os *scaffold*s e implantes desenvolvidos são promissores para aplicações em engenharia de tecidos ósseos, combinando propriedades osteocondutivas, atividade antibacteriana local e biocompatibilidade para melhorar a osseointegração e prevenir infecções ósseas.

O artigo "Multimaterial Coextrusion (Bio)printing of Composite Polymer Biomaterial Ink and Hydrogel Bioink for Tissue Fabrication" aborda uma nova técnica para bioimpressão 3D de *scaffold*s poliméricos combinados com biotintas de GelMA contendo células-tronco mesenquimais (MSCs) para aplicações em regeneração tecidual, com foco particular na regeneração óssea. Inicialmente, o estudo aborda a caracterização das “tintas” poliméricas de PLGA e PLGA-HA em DMSO, destacando seu comportamento reológico, como viscosidade e temperatura de gelificação. Observou-se uma diferença na temperatura de gelificação entre as tintas, o que pode ser estrategicamente utilizado para controlar o processo de extrusão durante a impressão 3D. Além disso, a adição de PBS ou meio de cultivo para remoção do solvente foi eficaz e levou a uma contração volumétrica das estruturas impressas. A troca de solvente permitiu a criação de porosidade nos *scaffold*s, mimetizando a microestrutura porosa do osso, o que pode facilitar a infiltração celular e vascularização. Em relação à degradação dos *scaffold*s, observou-se que ao longo do tempo os *scaffold*s apresentaram degradação hidrolítica controlada, mostrando estabilidade e adequação para a regeneração óssea.

A coextrusão multimaterial de PLGA e PLGA-HA com GelMA demonstrou ser viável, permitindo a fabricação de *scaffold*s com propriedades mecânicas significativamente superiores aos *scaffold*s apenas de GelMA. A técnica também mostrou capacidade de manter a integridade estrutural dos *scaffold*s na análise de compressão, fornecendo uma abordagem promissora para a fabricação de *scaffold*s compósitos para regeneração óssea. A viabilidade e proliferação das MSCs após a coextrusão multimaterial foram avaliadas, revelando que os *scaffold*s de PLGA/GelMA e PLGA-HA/GelMA não afetaram significativamente a viabilidade ou proliferação celular em comparação com os *scaffold*s apenas de GelMA. Além disso, observou-se que as células cresciam tanto dentro dos filamentos de GelMA quanto nas superfícies dos filamentos de PLGA e PLGA-HA, indicando interações entre os componentes hidrogel e polimérico.

Por fim, o estudo avaliou a diferenciação das MSCs nos *scaffold*s impressos, demonstrando que a presença de HA nos *scaffold*s PLGA-HA/GelMA promoveu a expressão de marcadores de diferenciação osteogênica, indicando um potencial aprimorado para a regeneração óssea. Em resumo, os resultados deste estudo sugerem que a abordagem de coextrusão multimaterial pode ser uma estratégia eficaz para fabricar *scaffold*s compostos para regeneração óssea, com propriedades mecânicas aprimoradas e capacidade de suportar o crescimento, proliferação e diferenciação de MSCs. No entanto, são necessários mais estudos para otimizar as condições de processamento e avaliar a eficácia da regeneração óssea *in vivo*.

8 CONCLUSÕES

As lesões no aparelho locomotor representam desafios substanciais para a qualidade de vida dos pacientes, frequentemente exigindo intervenções cirúrgicas para restaurar a função e mitigar complicações associadas. Esse estudo abordou uma variedade de técnicas de fabricação, desde a rotofiação até a bioimpressão 3D, demonstrando a versatilidade e eficácia de cada abordagem na produção de implantes e scaffolds com propriedades específicas. Os resultados obtidos indicam que os materiais desenvolvidos são altamente promissores em termos de bioatividade, biocompatibilidade, osteocondução e capacidade de prevenir infecções bacterianas. Os implantes produzidos por meio de manufatura aditiva e as membranas fibrosas fabricadas por rotofiação apresentaram características desejáveis, como morfologia homogênea, distribuição uniforme de HA e liberação controlada da RIF. Além disso, os scaffolds compostos produzidos por coextrusão multimaterial demonstraram propriedades mecânicas aprimoradas e capacidade de promover a diferenciação de células-tronco mesenquimais para facilitar a regeneração óssea.

Esses resultados oferecem uma visão otimista para o futuro do tratamento de lesões no aparelho locomotor, indicando que os implantes desenvolvidos neste estudo têm o potencial de superar as limitações dos implantes atuais, melhorando assim os resultados clínicos e a qualidade de vida dos pacientes. Com isso, este trabalho contribui significativamente para o avanço da engenharia de tecidos ósseos e oferece uma base sólida para pesquisas futuras nessa área crucial da medicina regenerativa.

9 SUGESTÕES DE TRABALHOS FUTUROS

Apesar do grande potencial dos scaffolds e implantes desenvolvinos nesse trabalho, estudos adicionais podem garantir a tradução bem-sucedida desses avanços para a prática clínica. Dessa maneira, algumas sugestões para trabalhos futuros incluem:

- Avaliação das taxas de biorreabsorção utilizando degradação enzimática para compreender a duração e atuação dos *scaffolds* no organismo;
- Estudos sobre possíveis efeitos da utilização de dispersantes na incorporação das nanopartículas aos *scaffolds*;
- Avaliação de potenciais estruturas anfifílicas ou hidrofílicas para aumentar a liberação de antibiótico;
- Estudos mais robustos sobre os mecanismos de diferenciação celular de pré-osteoblastos na presença dos *scaffolds;*
- Otimização dos parâmetros de processamento em PBF-EB para obter estruturas com maior fidelidade ao modelo projetado;
- Estudos adicionais para otimizar as condições, reprodutibilidade e escalabilidade das técnicas de processamento;
- Avaliação da resposta inflamatória dos *scaffolds* com estudo de liberação de citocinas inflamatórias;
- Estudos de eficácia e segurança a longo prazo;
- Validação da eficácia da regeneração óssea através de estudos *in vivo.*

REFERÊNCIAS

ABRAHAM, Adarsh Mathew; VENKATESAN, Subramani. A review on application of biomaterials for medical and dental implants. **Proceedings of the Institution of Mechanical Engineers, Part L: Journal of Materials: Design and Applications**, *[S. l.]*, v. 237, n. 2, p. 249–273, 2023. DOI: 10.1177/14644207221121981/ASSET/IMAGES/LARGE/10.1177_14644207221121981-FIG7.JPEG. Disponível em: https://journals.sagepub.com/doi/full/10.1177/14644207221121981. Acesso em: 5 jun. 2024.

AGARWAL, Rachit; GARCÍA, Andrés J. Biomaterial strategies for engineering implants for enhanced osseointegration and bone repair. **Advanced Drug Delivery Reviews**, *[S. l.]*, v. 94, p. 53–62, 2015. DOI: 10.1016/j.addr.2015.03.013.

AGARWAL, Sankalp; CURTIN, James; DUFFY, Brendan; JAISWAL, Swarna. Biodegradable magnesium alloys for orthopaedic applications: A review on corrosion, biocompatibility and surface modifications. **Materials Science and Engineering C**, *[S. l.]*, v. 68, p. 948–963, 2016. DOI: 10.1016/j.msec.2016.06.020. Disponível em: http://dx.doi.org/10.1016/j.msec.2016.06.020.

ALABORT, E.; BARBA, D.; REED, R. C. Design of metallic bone by additive manufacturing. **Scripta Materialia**, OxMet Technologies, 34 Centre for Innovation and EnterpriseBegbroke Science ParkOX5 1PF, United Kingdom, v. 164, p. 110–114, 2019. DOI: 10.1016/j.scriptamat.2019.01.022.

ALBREKTSSON, Tomas; CHRCANOVIC, Bruno; ÖSTMAN, Per Olov; SENNERBY, Lars. Initial and long-term crestal bone responses to modern dental implants. **Periodontology 2000**, *[S. l.]*, v. 73, n. 1, p. 41–50, 2017. DOI: 10.1111/PRD.12176. Disponível em: https://onlinelibrary.wiley.com/doi/full/10.1111/prd.12176. Acesso em: 6 jun. 2024.

ALBUHAIRN, B.; HIND, D.; HUTCHINSON, A. Antibiotic prophylaxis for wound infections in total joint arthroplasty : A systematic review. **Journal of Bone and Joint Surgery - Series B**, *[S. l.]*, v. 90, n. 7, p. 915–919, 2008. DOI: 10.1302/0301-620X.90B7.20498.

ANDRADE, T. M.; MELLO, D. C. R.; ELIAS, C. M. V; ABDALA, J. M. A.; SILVA, E.; VASCONCELLOS, L. M. R.; TIM, C. R.; MARCIANO, F. R.; LOBO, A. O. In vitro and in vivo evaluation of rotary-jet-spun poly(ε-caprolactone) with high loading of nano-hydroxyapatite. **Journal of Materials Science: Materials in Medicine**, Instituto Científico e Tecnológico, Universidade Brasil, Itaquera, São Paulo, Brazil, v. 30, n. 2, 2019. DOI: 10.1007/s10856-019-6222-1. Disponível em: https://doi.org/10.1007/s10856-019-6222-1.

ANSARY, R. H.; AWANG, M. B.; RAHMAN, M. M. Biodegradable poly(D,L-lactic-co-glycolic acid)-based micro/nanoparticles for sustained release of protein drugs - A review. **Tropical Journal of Pharmaceutical Research**, Kulliyyah of Pharmacy, International Islamic University Malaysia, 25200 Kuantan, Malaysia, v. 13, n. 7, p. 1179–1190, 2014. DOI: 10.4314/tjpr.v13i7.24. Disponível em: https://doi.org/10.4314/tjpr.v13i7.24.

ARAGÓN, Javier; FEOLI, Sergio; IRUSTA, Silvia; MENDOZA, Gracia. Composite scaffold obtained by electro-hydrodynamic technique for infection prevention and treatment in bone repair. **International Journal of Pharmaceutics**, *[S. l.]*, v. 557, n. November 2018, p. 162–169, 2019. DOI: 10.1016/j.ijpharm.2018.12.002.

ARTS, Mark P.; WOLFS, Jasper F. C.; CORBIN, Terry P. Porous silicon nitride spacers versus PEEK cages for anterior cervical discectomy and fusion: clinical and radiological results of a single-blinded randomized controlled trial. **European Spine Journal**, *[S. l.]*, v. 26, n. 9, p. 2372–2379, 2017. DOI: 10.1007/s00586-017-5079-6.

ARTS, Mark P.; WOLFS, Jasper Fc; CORBIN, Terry P. The CASCADE trial: Effectiveness of ceramic versus PEEK cages for anterior cervical discectomy with interbody fusion; Protocol of a blinded randomized controlled trial. **BMC Musculoskeletal Disorders**, *[S. l.]*, v. 14, p. 1–7, 2013. DOI: 10.1186/1471-2474-14-244.

BABIS, George C.; MAVROGENIS, Andreas F. Cobalt-chrome porous-coated implant-bone interface in total joint arthroplasty. **Bone-Implant Interface in Orthopedic Surgery: Basic Science to Clinical Applications**, *[S. l.]*, v. 9781447154099, p. 55–65, 2014. DOI: 10.1007/978-1-4471-5409-9_5/FIGURES/5. Disponível em: https://link.springer.com/chapter/10.1007/978-1-4471-5409-9_5. Acesso em: 14 maio. 2023.

BERGER, Michael B.; JACOBS, Thomas W.; BOYAN, Barbara D.; SCHWARTZ, Zvi. Hot isostatic pressure treatment of 3D printed Ti6Al4V alters surface modifications and cellular response. **Journal of Biomedical Materials Research - Part B Applied Biomaterials**, *[S. l.]*, v. 108, n. 4, p. 1262–1273, 2020. DOI: 10.1002/jbm.b.34474.

BIKAS, H.; STAVROPOULOS, P.; CHRYSSOLOURIS, G. Additive manufacturing methods and modelling approaches: a critical review. **The International Journal of Advanced Manufacturing Technology**, *[S. l.]*, v. 83, n. 1, p. 389–405, 2016. DOI: 10.1007/s00170-015-7576-2.

BOCK, Ryan M.; MCENTIRE, Bryan J.; BAL, B. Sonny; RAHAMAN, Mohamed N.; BOFFELLI, Marco; PEZZOTTI, Giuseppe. Surface modulation of silicon nitride ceramics for orthopaedic applications. **Acta Biomaterialia**, *[S. l.]*, v. 26, p. 318–330, 2015. DOI: 10.1016/j.actbio.2015.08.014. Disponível em: http://dx.doi.org/10.1016/j.actbio.2015.08.014.

BOON, M. R.; VAN DER HORST, G.; VAN DER PLUIJM, G.; TAMSMA, J. T.; SMIT, J. W. A.; RENSEN, P. C. N. Bone morphogenetic protein 7: A broad-spectrum growth factor with multiple target therapeutic potency. **Cytokine and Growth Factor Reviews**, Department of General Internal Medicine, Endocrinology and Metabolic Diseases, Leiden University Medical Center, Leiden, Netherlands, v. 22, n. 4, p. 221–229, 2011. DOI: 10.1016/j.cytogfr.2011.08.001. Disponível em: https://www.scopus.com/inward/record.uri?eid=2-s2.0-81155149867&doi=10.1016%2Fj.cytogfr.2011.08.001&partnerID=40&md5=712c4acdcecbd9cbb5045ecc13b71c45.

BOZKURT, Celal; ŞENKÖYLÜ, Alpaslan; AKTAŞ, Erdem; SARIKAYA, Baran; SIPAHIOĞLU, Serkan; GÜRBÜZ, Riza; TIMUÇIN, Muharrem. Biomechanical Evaluation

of a Novel Apatite-Wollastonite Ceramic Cage Design for Lumbar Interbody Fusion: A Finite Element Model Study. **BioMed Research International**, *[S. l.]*, v. 2018, 2018. DOI: 10.1155/2018/4152543.

BRACEY, D. N.; SEYLER, T. M.; JINNAH, A. H.; LIVELY, M. O.; WILLEY, J. S.; SMITH, T. L.; VAN DYKE, M. E.; WHITLOCK, P. W. A decellularized porcine xenograft-derived bone scaffold for clinical use as a bone graft substitute: A critical evaluation of processing and structure. **Journal of Functional Biomaterials**, Department of Orthopaedic Surgery, Wake Forest School of Medicine, Winston-Salem, NC 27157, United States, v. 9, n. 3, 2018. DOI: 10.3390/jfb9030045. Disponível em: https://www.scopus.com/inward/record.uri?eid=2-s2.0-85051819725&doi=10.3390%2Fjfb9030045&partnerID=40&md5=76f944d3017a6f8bc1fbbdcc1a21c350.

BUSER, Z.; BRODKE, D. S.; YOUSSEF, J. A.; MEISEL, H. J.; MYHRE, S. L.; HASHIMOTO, R.; PARK, J. B.; YOON, S. T.; WANG, J. C. Synthetic bone graft versus autograft or allograft for spinal fusion: A systematic review. **Journal of Neurosurgery: Spine**, Department of Orthopaedic Surgery, Keck School of Medicine, University of Southern California, Elaine Stevely Hoffman Medical Research Center, HMR 710, 2011 Zonal Ave., Los Angeles, CA 90033, United States, v. 25, n. 4, p. 509–516, 2016. DOI: 10.3171/2016.1.SPINE151005. Disponível em: https://www.scopus.com/inward/record.uri?eid=2-s2.0-84990851652&doi=10.3171%2F2016.1.SPINE151005&partnerID=40&md5=41b2554a8a76c09ddaf97de52a7605e3.

CASALETTO, M. P.; INGO, G. M.; KACIULIS, S.; MATTOGNO, G.; PANDOLFI, L.; SCAVIA, G. Surface studies of in vitro biocompatibility of titanium oxide coatings. **Applied Surface Science**, Amsterdam, v. 172, n. 1–2, p. 167–177, 2001. DOI: 10.1016/S0169-4332(00)00844-8.

CESAR, R.; BRAVO-CASTILLERO, J.; RAMOS, R. R.; PEREIRA, C. A. M.; ZANIN, H.; ROLLO, J. M. D. A. Relating mechanical properties of vertebral trabecular bones to osteoporosis. **Computer Methods in Biomechanics and Biomedical Engineering**, *[S. l.]*, v. 23, n. 2, p. 54–68, 2020. DOI: 10.1080/10255842.2019.1699542.

CHAU, A. M. T.; XU, L. L.; WONG, J. H. Y.; MOBBS, R. J. Current status of bone graft options for anterior interbody fusion of the cervical and lumbar spine. **Neurosurgical Review**, Department of Neurosurgery, Royal Prince Alfred Hospital, Sydney, Australia, v. 37, n. 1, p. 23–37, 2014. DOI: 10.1007/s10143-013-0483-9. Disponível em: https://doi.org/10.1007/s10143-013-0483-9.

CHEN, Cen; HAO, Ya; BAI, Xue; NI, Junjie; CHUNG, Sung Min; LIU, Fan; LEE, In Seop. 3D printed porous Ti6Al4V cage: Effects of additive angle on surface properties and biocompatibility; bone ingrowth in Beagle tibia model. **Materials and Design**, *[S. l.]*, v. 175, n. 928, p. 107824, 2019. DOI: 10.1016/j.matdes.2019.107824.

CHEN, G.; DENG, C.; LI, Y. P. TGF-β and BMP signaling in osteoblast differentiation and bone formation. **International Journal of Biological Sciences**, Institute of Genetics, Life Science College, Zhejiang University, 388 Yuhang Road, Hangzhou 310058, China, v. 8, n. 2, p. 272–288, 2012. DOI: 10.7150/ijbs.2929. Disponível em:

https://www.scopus.com/inward/record.uri?eid=2-s2.0-84863040008&doi=10.7150%2Fijbs.2929&partnerID=40&md5=5f1b20e7c9622c15991a62c8968a9385.

CHEN, Qizhi; THOUAS, George A. Metallic implant biomaterials. **Materials Science and Engineering R: Reports**, *[S. l.]*, v. 87, p. 1–57, 2015. DOI: 10.1016/j.mser.2014.10.001.

CHEN, Y.; WANG, X.; LU, X.; YANG, L.; YANG, H.; YUAN, W.; CHEN, D. Comparison of titanium and polyetheretherketone (PEEK) cages in the surgical treatment of multilevel cervical spondylotic myelopathy: A prospective, randomized, control study with over 7-year follow-up. **European Spine Journal**, Department of Spine Surgery, Changzheng Hospital, Second Military Medical University, 415 Fengyang Road, 200003 Shanghai, China, v. 22, n. 7, p. 1539–1546, 2013. DOI: 10.1007/s00586-013-2772-y. Disponível em: https://www.scopus.com/inward/record.uri?eid=2-s2.0-84879941659&doi=10.1007%2Fs00586-013-2772-y&partnerID=40&md5=8c80465887608244acf0fbf87052cb3a.

CVRČEK, Ladislav; HORÁKOVÁ, Marta. Plasma Modified Polymeric Materials for Implant Applications. **Non-Thermal Plasma Technology for Polymeric Materials: Applications in Composites, Nanostructured Materials, and Biomedical Fields**, *[S. l.]*, p. 367–407, 2019. DOI: 10.1016/B978-0-12-813152-7.00014-7. Acesso em: 9 maio. 2023.

DAENTZER, Dorothea et al. Preliminary results in anterior cervical discectomy and fusion with an experimental bioabsorbable cage - clinical and radiological findings in an ovine animal model. **SpringerPlus**, *[S. l.]*, v. 2, n. 1, p. 1–8, 2013. DOI: 10.1186/2193-1801-2-418.

DAENTZER, Dorothea et al. Bioabsorbable interbody magnesium-polymer cage: Degradation kinetics, biomechanical stiffness, and histological findings from an ovine cervical spine fusion model. **Spine**, *[S. l.]*, v. 39, n. 20, p. E1220–E1227, 2014. DOI: 10.1097/BRS.0000000000000507.

DATASUS. **Sistema De Informações Ambulatoriais do SUS (SIA/SUS)**. 2023. Disponível em: http://tabnet.datasus.gov.br/.

DEFRATES, K. G.; MOORE, R.; BORGESI, J.; LIN, G. W.; MULDERIG, T.; BEACHLEY, V.; HU, X. Protein-Based Fiber Materials in Medicine: A Review. **Nanomaterials**, *[S. l.]*, v. 8, n. 7, p. 26, 2018. DOI: 10.3390/nano8070457. Disponível em: https://doi.org/10.3390/nano8070457.

DELANEY, Lauren J. et al. Ultrasound-triggered antibiotic release from PEEK clips to prevent spinal fusion infection: Initial evaluations. **Acta Biomaterialia**, *[S. l.]*, v. 93, p. 12–24, 2019. DOI: 10.1016/j.actbio.2019.02.041. Disponível em: https://doi.org/10.1016/j.actbio.2019.02.041.

D'SOUZA, Marissa; MACDONALD, Nicholas A.; GENDREAU, Julian L.; DUDDLESTON, Pate J.; FENG, Austin Y.; HO, Allen L. Graft materials and biologics for spinal interbody fusion. **Biomedicines**, *[S. l.]*, v. 7, n. 4, p. 1–15, 2019. DOI: 10.3390/biomedicines7040075.

DUMAS, Mathieu; TERRIAULT, Patrick; BRAILOVSKI, Vladimir. Modelling and characterization of a porosity graded lattice structure for additively manufactured biomaterials. **Materials & Design**, *[S. l.]*, v. 121, p. 383–392, 2017. DOI: https://doi.org/10.1016/j.matdes.2017.02.021.

DUX, K. E. Implantable Materials Update. **Clinics in Podiatric Medicine and Surgery**, *[S. l.]*, v. 36, n. 4, p. 535- +, 2019. DOI: 10.1016/j.cpm.2019.06.001.

ECHAVE, M. C.; PIMENTA-LOPES, C.; PEDRAZ, J. L.; MEHRALI, M.; DOLATSHAHI-PIROUZ, A.; VENTURA, F.; ORIVE, G. Enzymatic crosslinked gelatin 3D scaffolds for bone tissue engineering. **International Journal of Pharmaceutics**, NanoBioCel Group, Laboratory of Pharmaceutics, School of Pharmacy, University of the Basque Country UPV/EHU, Paseo de la Universidad 7, Vitoria-Gasteiz, 01006, Spain, v. 562, p. 151–161, 2019. DOI: 10.1016/j.ijpharm.2019.02.043.

ELLIOTT, Cameron A.; FOX, Richard; ASHFORTH, Robert; GOURISHANKAR, Sita; NATARAJ, Andrew. Magnetic resonance imaging artifact following anterior cervical discectomy and fusion with a trabecular metal cage. **Journal of Neurosurgery: Spine**, *[S. l.]*, v. 24, n. 3, p. 496–501, 2016. DOI: 10.3171/2015.5.SPINE14219.

FATOYE, F.; GEBRYE, T.; ODEYEMI, I. Real-world incidence and prevalence of low back pain using routinely collected data. **Rheumatology International**, *[S. l.]*, v. 39, n. 4, p. 619–626, 2019. DOI: 10.1007/s00296-019-04273-0.

FENG, X. Chemical and biochemical basis of cell-bone matrix interaction in health and disease. **Current Chemical Biology**, Department of Pathology, University of Alabama at Birmingham, 1670 University Blvd., Birmingham, AL 35294, United States, v. 3, n. 2, p. 189–196, 2009. DOI: 10.2174/187231309788166398. Disponível em: https://www.scopus.com/inward/record.uri?eid=2-s2.0-68449091259&doi=10.2174%2F187231309788166398&partnerID=40&md5=68febfaca6f86da550c6cadb2339bd8b.

FERNÁNDEZ-FAIREN, Mariano; ALVARADO, Enrique; TORRES, Ana. Eleven-Year Follow-Up of Two Cohorts of Patients Comparing Stand-Alone Porous Tantalum Cage Versus Autologous Bone Graft and Plating in Anterior Cervical Fusions. **World Neurosurgery**, *[S. l.]*, v. 122, p. e156–e167, 2019. DOI: 10.1016/j.wneu.2018.09.160. Disponível em: https://doi.org/10.1016/j.wneu.2018.09.160.

FISCHER, C. R.; CASSILLY, R.; CANTOR, W.; EDUSEI, E.; HAMMOURI, Q.; ERRICO, T. A systematic review of comparative studies on bone graft alternatives for common spine fusion procedures. **European Spine Journal**, Columbia University Medical Center PH11-1109, 622 West 168th Street, New York NY 10032, United States, v. 22, n. 6, p. 1423–1435, 2013. DOI: 10.1007/s00586-013-2718-4. Disponível em: https://www.scopus.com/inward/record.uri?eid=2-s2.0-84879229323&doi=10.1007%2Fs00586-013-2718-4&partnerID=40&md5=87199853ea9d570302d87eae1da76738.

FU, Le; XIONG, Yi; CARLSSON, Gunnar; PALMER, Michael; ÖRN, Stefan; ZHU, Wei; WENG, Xisheng; ENGQVIST, Håkan; XIA, Wei. Biodegradable Si3N4 bioceramic sintered with Sr, Mg and Si for spinal fusion: Surface characterization and biological

evaluation. **Applied Materials Today**, *[S. l.]*, v. 12, p. 260–275, 2018. DOI: 10.1016/j.apmt.2018.06.002.

GAI, X.; BAI, Y.; LI, S.; HOU, W.; HAO, Y.; ZHANG, X.; YANG, R.; MISRA, R. D. K. In-situ monitoring of the electrochemical behavior of cellular structured biomedical Ti-6Al-4V alloy fabricated by electron beam melting in simulated physiological fluid. **Acta Biomaterialia**, Institute of Metal Research, Chinese Academy of Sciences, 72 Wenhua Road, Shenyang, 110016, China, v. 106, p. 387–395, 2020. DOI: 10.1016/j.actbio.2020.02.008.

GANESH, V. K.; RAMAKRISHNA, K.; GHISTA, Dhanjoo N. Biomechanics of bone-fracture fixation by stiffness-graded plates in comparison with stainless-steel plates. **BioMedical Engineering Online**, *[S. l.]*, v. 4, 2005. DOI: 10.1186/1475-925X-4-46/FIGURES/1. Acesso em: 14 maio. 2023.

GENTILE, Piergiorgio; CHIONO, Valeria; CARMAGNOLA, Irene; HATTON, Paul V. An overview of poly(lactic-co-glycolic) Acid (PLGA)-based biomaterials for bone tissue engineering. **International Journal of Molecular Sciences**, *[S. l.]*, v. 15, n. 3, p. 3640–3659, 2014. DOI: 10.3390/ijms15033640. Disponível em: https://doi.org/10.3390/ijms15033640.

GHAYOR, Chafik; WEBER, Franz E. Osteoconductive microarchitecture of bone substitutes for bone regeneration revisited. **Frontiers in Physiology**, *[S. l.]*, v. 9, n. JUL, p. 1–10, 2018. DOI: 10.3389/fphys.2018.00960.

GIBON, Emmanuel; AMANATULLAH, Derek F.; LOI, Florence; PAJARINEN, Jukka; NABESHIMA, Akira; YAO, Zhenyu; HAMADOUCHE, Moussa; GOODMAN, Stuart B. The biological response to orthopaedic implants for joint replacement: Part I: Metals. **Journal of Biomedical Materials Research Part B: Applied Biomaterials**, *[S. l.]*, v. 105, n. 7, p. 2162–2173, 2017. DOI: 10.1002/JBM.B.33734. Disponível em: https://onlinelibrary.wiley.com/doi/full/10.1002/jbm.b.33734. Acesso em: 14 maio. 2023.

GILCHRIST, Samuel E.; LANGE, Dirk; LETCHFORD, Kevin; BACH, Horacio; FAZLI, Ladan; BURT, Helen M. Fusidic acid and rifampicin co-loaded PLGA nanofibers for the prevention of orthopedic implant associated infections. **Journal of Controlled Release**, *[S. l.]*, v. 170, n. 1, p. 64–73, 2013. DOI: 10.1016/j.jconrel.2013.04.012. Acesso em: 30 maio. 2021.

GOHARIAN, Amirhossein; ABDULLAH, Mohamed R. Bioinert Metals (Stainless Steel, Titanium, Cobalt Chromium). **Trauma Plating Systems: Biomechanical, Material, Biological, and Clinical Aspects**, *[S. l.]*, p. 115–142, 2017. DOI: 10.1016/B978-0-12-804634-0.00007-0. Acesso em: 14 maio. 2023.

HASAN, Abshar; WAIBHAW, Gyan; SAXENA, Varun; PANDEY, Lalit M. Nano-biocomposite scaffolds of chitosan, carboxymethyl cellulose and silver nanoparticle modified cellulose nanowhiskers for bone tissue engineering applications. **International Journal of Biological Macromolecules**, *[S. l.]*, v. 111, p. 923–934, 2018. DOI: 10.1016/j.ijbiomac.2018.01.089.

HUANG, Haiyue et al. COVID-19: A Call for Physical Scientists and Engineers. **ACS Nano**, *[S. l.]*, 2020. DOI: 10.1021/acsnano.0c02618.

HUANG, Jianghong; XIONG, Jianyi; LIU, Jianquan; ZHU, Weimin; CHEN, Jielin; DUAN, Li; ZHANG, Jufeng; WANG, Daping. Evaluation of the novel three-dimensional porous poly (L-lactic acid)/nano-hydroxyapatite composite scaffold. **Bio-Medical Materials and Engineering**, *[S. l.]*, v. 26, n. s1, p. S197–S205, 2015. DOI: 10.3233/BME-151306.

JAHAN, K.; TABRIZIAN, M. Composite biopolymers for bone regeneration enhancement in bony defects. **Biomaterials Science**, *[S. l.]*, v. 4, n. 1, p. 25–39, 2016. DOI: 10.1039/c5bm00163c.

JAHANMARD, F. et al. Bactericidal coating to prevent early and delayed implant-related infections. **Journal of Controlled Release**, *[S. l.]*, v. 326, n. March, p. 38–52, 2020. DOI: 10.1016/j.jconrel.2020.06.014.

JAKOI, A. M.; IORIO, J. A.; CAHILL, P. J. Autologous bone graft harvesting: a review of grafts and surgical techniques. **Musculoskeletal Surgery**, University Orthopedic Institute at Hahnemann, 240 North Broad Street, Mail Stop 420, Philadelphia, PA 19102, United States, v. 99, n. 3, p. 171–178, 2015. DOI: 10.1007/s12306-015-0351-6. Disponível em: https://www.scopus.com/inward/record.uri?eid=2-s2.0-84947426974&doi=10.1007%2Fs12306-015-0351-6&partnerID=40&md5=1a86265011b93739b6bef90d8a2acf2f.

KANERVA, Lasse; FÖRSTRÖM, Lars. Allergic nickel and chromate hand dermatitis induced by orthopaedic metal implant. **Contact Dermatitis**, *[S. l.]*, v. 44, n. 2, p. 103–104, 2001. DOI: 10.1034/J.1600-0536.2001.4402096.X. Disponível em: https://onlinelibrary.wiley.com/doi/full/10.1034/j.1600-0536.2001.4402096.x. Acesso em: 14 maio. 2023.

KAUR, Sukhpreet; GHADIRINEJAD, Khashayar; OSKOUEI, Reza H. An overview on the tribological performance of titanium alloys with surface modifications for biomedical applications. **Lubricants**, *[S. l.]*, v. 7, n. 8, 2019. DOI: 10.3390/lubricants7080065.

KELLY, Cambre N.; MILLER, Andrew T.; HOLLISTER, Scott J.; GULDBERG, Robert E.; GALL, Ken. Design and Structure–Function Characterization of 3D Printed Synthetic Porous Biomaterials for Tissue Engineering. **Advanced Healthcare Materials**, *[S. l.]*, v. 7, n. 7, p. 1–16, 2018. DOI: 10.1002/adhm.201701095.

KERSTEN, Roel F. M. R.; WU, Gang; POURAN, Behdad; VAN DER VEEN, Albert J.; WEINANS, Harrie H.; DE GAST, Arthur; ÖNER, F. Cumhur; VAN GAALEN, Steven M. Comparison of polyetheretherketone versus silicon nitride intervertebral spinal spacers in a caprine model. **Journal of Biomedical Materials Research - Part B Applied Biomaterials**, *[S. l.]*, v. 107, n. 3, p. 688–699, 2019. DOI: 10.1002/jbm.b.34162.

KERSTEN, Roel Fmr; VAN GAALEN, Steven M.; ARTS, Mark P.; ROES, Kit Cb; DE GAST, Arthur; CORBIN, Terry P.; ÖNER, F. Cumhur. The SNAP trial: A double blind multi-center randomized controlled trial of a silicon nitride versus a PEEK cage in transforaminal lumbar interbody fusion in patients with symptomatic degenerative lumbar

disc disorders: Study protocol. **BMC Musculoskeletal Disorders**, *[S. l.]*, v. 15, n. 1, 2014. DOI: 10.1186/1471-2474-15-57.

KERSTEN, Roel Frederik Mark Raymond; VAN GAALEN, Steven M.; DE GAST, Arthur; ÖNER, F. Cumhur. Polyetheretherketone (PEEK) cages in cervical applications: A systematic review. **Spine Journal**, *[S. l.]*, v. 15, n. 6, p. 1446–1460, 2015. DOI: 10.1016/j.spinee.2013.08.030.

KIM, Chang Yong; JUNG, Youngmee; LIM, Soonho; KIM, Soo Hyun. On the enhancement of thermo-mechanical properties of poly(L-lactide) by solid-state extrusion for biodegradable spinal fixation devices. **Macromolecular Research**, *[S. l.]*, v. 25, n. 9, p. 890–897, 2017. DOI: 10.1007/s13233-017-5106-9.

KNUTSEN, Ashleen R.; BORKOWSKI, Sean L.; EBRAMZADEH, Edward; FLANAGAN, Colleen L.; HOLLISTER, Scott J.; SANGIORGIO, Sophia N. Static and dynamic fatigue behavior of topology designed and conventional 3D printed bioresorbable PCL cervical interbody fusion devices. **Journal of the Mechanical Behavior of Biomedical Materials**, *[S. l.]*, v. 49, p. 332–342, 2015. DOI: 10.1016/j.jmbbm.2015.05.015.

KODAMA, Tomonobu; NAKAI, Ryusuke; GOTO, Kenji; SHIMA, Kunihiro; IWATA, Hiroo. Preparation of an Au-Pt alloy free from artifacts in magnetic resonance imaging. **Magnetic Resonance Imaging**, *[S. l.]*, v. 44, p. 38–45, 2017. DOI: 10.1016/j.mri.2017.07.006. Disponível em: https://doi.org/10.1016/j.mri.2017.07.006.

KURODA, Y.; KITADA, M.; WAKAO, S.; DEZAWA, M. Bone marrow mesenchymal cells: How do they contribute to tissue repair and are they really stem cells? **Archivum Immunologiae et Therapiae Experimentalis**, Department of Stem Cell Biology and Histology, Tohoku University, Graduate School of Medicine, 2-1, Seiryo-machi, Aoba-Ku, Sendai 980-8575, Japan, v. 59, n. 5, p. 369–378, 2011. DOI: 10.1007/s00005-011-0139-9. Disponível em: https://www.scopus.com/inward/record.uri?eid=2-s2.0-80054091287&doi=10.1007%2Fs00005-011-0139-9&partnerID=40&md5=face6215cd974382bdb7330e30b70b7c.

KURTZ, Steven M.; LAU, Edmund; SCHMIER, Jordana; ONG, Kevin L.; ZHAO, Ke; PARVIZI, Javad. Infection Burden for Hip and Knee Arthroplasty in the United States. *[S. l.]*, v. 23, n. 7, p. 984–991, 2008. DOI: 10.1016/j.arth.2007.10.017.

KURTZ, Steven M.; LAU, Edmund; WATSON, Heather; SCHMIER, Jordana K.; PARVIZI, Javad. Economic Burden of Periprosthetic Joint Infection in the United States. **Journal of Arthroplasty**, *[S. l.]*, v. 27, n. 8, p. 61- 65.e1, 2012. DOI: 10.1016/j.arth.2012.02.022.

LANGER, R.; VACANTI, J. P. Tissue engineering. **Science**, Department of Chemical Engineering, Harvard-M.I.T. Division of Health, Sciences and Technology, Massachusetts Institute of Technology, Cambridge, MA 02319, United States, v. 260, n. 5110, p. 920–926, 1993. DOI: 10.1126/science.8493529. Disponível em: https://www.scopus.com/inward/record.uri?eid=2-s2.0-0027595948&doi=10.1126%2Fscience.8493529&partnerID=40&md5=e32b65fe2864c402be36ce4b1b4dafdf.

LEBHAR, Jonathan; KRIEGEL, Pierre; CHATELLIER, Patrick; BRETON, Yann; ROPARS, Mickael; HUTEN, Denis. Tantalum implants for posterior lumbar interbody fusion: A safe method at medium-term follow-up? **Orthopaedics and Traumatology: Surgery and Research**, *[S. l.]*, v. 106, n. 2, p. 269–274, 2020. DOI: 10.1016/j.otsr.2019.10.028. Disponível em: https://doi.org/10.1016/j.otsr.2019.10.028.

LEE, J. H.; KIM, S. K.; KANG, S. S.; HAN, S. J.; LEE, C. K.; CHANG, B. S. A Long-Term Follow-up, Multicenter, Comparative Study of the Radiologic, and Clinical Results between a CaO-SiO2-P2O5-B2O3 Bioactive Glass Ceramics (BGS-7) Intervertebral Spacer and Titanium Cage in 1-Level Posterior Lumbar Interbody Fusion. **Clinical Spine Surgery**, Department of Orthopedic Surgery, College of Medicine Seoul National University, Seoul, South Korea, 2020. DOI: 10.1097/BSD.0000000000000950. Disponível em: https://www.scopus.com/inward/record.uri?eid=2-s2.0-85080134268&doi=10.1097%2FBSD.0000000000000950&partnerID=40&md5=55873f8e9d5877461e8e29801ef47fef.

LI, J. L.; QIN, L.; YANG, K.; MA, Z. J.; WANG, Y. X.; CHENG, L. L.; ZHAO, D. W. Materials evolution of bone plates for internal fixation of bone fractures: A review. **Journal of Materials Science & Technology**, *[S. l.]*, v. 36, p. 190–208, 2020. a. DOI: 10.1016/j.jmst.2019.07.024.

LI, Junlei; QIN, Ling; YANG, Ke; MA, Zhijie; WANG, Yongxuan; CHENG, Liangliang; ZHAO, Dewei. Materials evolution of bone plates for internal fixation of bone fractures: A review. **Journal of Materials Science and Technology**, *[S. l.]*, v. 36, p. 190–208, 2020. b. DOI: 10.1016/j.jmst.2019.07.024.

LI, X. L.; HOU, T.; LU, Y. S.; YANG, B. A method for controlling the surface morphology of centrifugally spun starch-based fibers. **Journal of Applied Polymer Science**, *[S. l.]*, v. 135, n. 6, p. 7, 2018. DOI: 10.1002/app.45810.

LIN, Sien et al. PLGA/β-TCP composite scaffold incorporating salvianolic acid B promotes bone fusion by angiogenesis and osteogenesis in a rat spinal fusion model. **Biomaterials**, *[S. l.]*, v. 196, p. 109–121, 2019. DOI: 10.1016/j.biomaterials.2018.04.004.

LIU, Fei; RAN, Qichun; ZHAO, Miao; ZHANG, Tao; ZHANG, David Z.; SU, Zuqiang. **Additively Manufactured Continuous Cell-Size Gradient Porous Scaffolds: Pore Characteristics, Mechanical Properties and Biological Responses In Vitro**. **Materials** , 2020. a. DOI: 10.3390/ma13112589.

LIU, S.; WANG, Y.; LIANG, Z.; ZHOU, M.; CHEN, C. Comparative Clinical Effectiveness and Safety of Bone Morphogenetic Protein Versus Autologous Iliac Crest Bone Graft in Lumbar Fusion: A Meta-analysis and Systematic Review. **Spine**, Department of Neurosurgery, Fujian Medical University Union Hospital, Fuzhou, Fujian, China, v. 45, n. 12, p. E729–E741, 2020. b. DOI: 10.1097/BRS.0000000000003372. Disponível em: https://www.scopus.com/inward/record.uri?eid=2-s2.0-85085714557&doi=10.1097%2FBRS.0000000000003372&partnerID=40&md5=9f77bae3d6bc537289ea4b79e6c9d055.

LOESSNER, Daniela et al. Functionalization, preparation and use of cell-laden gelatin methacryloyl-based hydrogels as modular tissue culture platforms. **Nature Protocols**, *[S. l.]*, v. 11, n. 4, p. 727–746, 2016. DOI: 10.1038/nprot.2016.037. Acesso em: 12 set. 2021.

LOORDHUSWAMY, A.; THINAKARAN, S.; VENKATESHWAPURAM RANGASWAMY, G. D. Centrifugal spun osteoconductive ultrafine fibrous mat as a scaffold for bone regeneration. **Journal of Drug Delivery Science and Technology**, Department of Textile Technology, Anna University, Chennai, India, v. 60, 2020. DOI: 10.1016/j.jddst.2020.101978. Disponível em: https://doi.org/10.1016/j.jddst.2020.101978.

LU, Ming et al. Application of a novel porous tantalum implant in rabbit anterior lumbar spine fusion model: In vitro and in vivo experiments. **Chinese Medical Journal**, *[S. l.]*, v. 132, n. 1, p. 51–62, 2019. DOI: 10.1097/CM9.0000000000000030.

LU, Y.; LI, Y.; ZHANG, S.; XU, G. J.; FU, K.; LEE, H.; ZHANG, X. W. Parameter study and characterization for polyacrylonitrile nanofibers fabricated via centrifugal spinning process. **European Polymer Journal**, *[S. l.]*, v. 49, n. 12, p. 3834–3845, 2013. DOI: 10.1016/j.eurpolymj.2013.09.017.

MASTERS, Elysia A. et al. Evolving concepts in bone infection: redefining “biofilm”, “acute vs. chronic osteomyelitis”, “the immune proteome” and “local antibiotic therapy”. **Bone Research**, *[S. l.]*, v. 7, n. 1, 2019. DOI: 10.1038/s41413-019-0061-z.

MCGILVRAY, Kirk C.; EASLEY, Jeremiah; SEIM, Howard B.; REGAN, Daniel; BERVEN, Sigurd H.; HSU, Wellington K.; MROZ, Thomas E.; PUTTLITZ, Christian M. Bony ingrowth potential of 3D-printed porous titanium alloy: a direct comparison of interbody cage materials in an in vivo ovine lumbar fusion model. **Spine Journal**, *[S. l.]*, v. 18, n. 7, p. 1250–1260, 2018. DOI: 10.1016/j.spinee.2018.02.018.

MCNEILL INGHAM, Sheila J.; DE CARVALHO, Rogerio Teixeira; ABDALLA, Rene J.; FU, Freddie H.; LOVEJOY, C. Owen. Bony Morphology: Comparative Anatomy and its Importance for the Anterior Cruciate Ligament. **Operative Techniques in Orthopaedics**, *[S. l.]*, v. 27, n. 1, p. 2–7, 2017. DOI: 10.1053/J.OTO.2017.01.002. Acesso em: 14 maio. 2023.

MINDRU, T. B.; IGNAT, L.; MINDRU, I. B.; PINTEALA, M. Morphological aspects of polymer fiber mats obtained by air flow rotary-jet spinning. **Fibers and Polymers**, *[S. l.]*, v. 14, n. 9, p. 1526–1534, 2013. DOI: 10.1007/s12221-013-1526-0.

MOBBS, R. J.; CHUNG, M.; RAO, P. J. Bone graft substitutes for anterior lumbar interbody fusion. **Orthopaedic surgery**, Neuro Spine Clinic, Prince of Wales Private Hospital, Randwick, Australia. ralphmobbs@hotmail.com, v. 5, n. 2, p. 77–85, 2013. DOI: 10.1111/os.12030. Disponível em: https://www.scopus.com/inward/record.uri?eid=2-s2.0-84891385334&doi=10.1111%2Fos.12030&partnerID=40&md5=aef20652ef66f39537b1454e3a36b129.

MONDAL, S.; GHOSH, R. Bone remodelling around the tibia due to total ankle replacement: effects of implant material and implant–bone interfacial conditions. **Computer Methods in Biomechanics and Biomedical Engineering**, School of Engineering, Indian Institute of Technology Mandi, Mandi, India, v. 22, n. 16, p. 1247–1257, 2019. DOI:

10.1080/10255842.2019.1661385. Disponível em: https://www.scopus.com/inward/record.uri?eid=2-s2.0-85072627591&doi=10.1080%2F10255842.2019.1661385&partnerID=40&md5=fa68d2cff83d5cf571a6bdb4d67297ac.

MOSTOFI, K.; MOGHADDAM, B. G.; PEYRAVI, M.; KHOUZANI, R. K. Preliminary results of anterior cervical arthroplasty by porous alumina ceramic cage for cervical disc herniation surgery. **Journal of Craniovertebral Junction and Spine**, Department of Neurosurgery, Center Clinical, Chirurgie de Rachis, Soyaux, France, v. 9, n. 4, p. 223–226, 2018. DOI: 10.4103/jcvjs.JCVJS_95_18. Disponível em: https://www.scopus.com/inward/record.uri?eid=2-s2.0-85060638423&doi=10.4103%2Fjcvjs.JCVJS_95_18&partnerID=40&md5=13bd65ccb13c6765573b27d39c5409dd.

MOURA, Lucas S.; VITTORIA, Gianfranco D.; GABRIEL, André H. G.; FONSECA, Eduardo B.; GABRIEL, Laís P.; WEBSTER, Thomas J.; LOPES, Éder S. N. A highly accurate methodology for the prediction and correlation of mechanical properties based on the slimness ratio of additively manufactured tensile test specimens. **Journal of Materials Science**, *[S. l.]*, v. 55, n. 22, p. 9578–9596, 2020. DOI: 10.1007/S10853-020-04654-Y/FIGURES/8. Disponível em: https://link.springer.com/article/10.1007/s10853-020-04654-y. Acesso em: 7 maio. 2023.

MU, Junnan; LUO, Danni; LI, Wei; DING, Yaping. Multiscale polymeric fibers for drug delivery and tissue engineering. **Biomedical Technology**, *[S. l.]*, v. 5, p. 60–72, 2024. DOI: 10.1016/J.BMT.2023.05.001. Acesso em: 5 jun. 2024.

NEMOTO, Osamu; ASAZUMA, Takashi; YATO, Yoshiyuki; IMABAYASHI, Hideaki; YASUOKA, Hiroki; FUJIKAWA, Akira. Comparison of fusion rates following transforaminal lumbar interbody fusion using polyetheretherketone cages or titanium cages with transpedicular instrumentation. **European Spine Journal**, *[S. l.]*, v. 23, n. 10, p. 2150–2155, 2014. DOI: 10.1007/s00586-014-3466-9.

NUNE, K. C.; KUMAR, A.; MISRA, R. D. K.; LI, S. J.; HAO, Y. L.; YANG, R. Functional response of osteoblasts in functionally gradient titanium alloy mesh arrays processed by 3D additive manufacturing. **Colloids and Surfaces B: Biointerfaces**, *[S. l.]*, v. 150, p. 78–88, 2017. DOI: https://doi.org/10.1016/j.colsurfb.2016.09.050.

NUNE, K. C.; KUMAR, A.; MURR, L. E.; MISRA, R. D. K. Interplay between self-assembled structure of bone morphogenetic protein-2 (BMP-2) and osteoblast functions in three-dimensional titanium alloy scaffolds: Stimulation of osteogenic activity. **Journal of Biomedical Materials Research - Part A**, *[S. l.]*, v. 104, n. 2, p. 517–532, 2016. DOI: 10.1002/jbm.a.35592.

OLIVARES-NAVARRETE, R.; HYZY, S. L.; SLOSAR, P. J.; SCHNEIDER, J. M.; SCHWARTZ, Z.; BOYAN, B. D. Implant materials generate different peri-implant inflammatory factors: Poly-ether-ether-ketone promotes fibrosis and microtextured titanium promotes osteogenic factors. **Spine**, *[S. l.]*, v. 40, n. 6, p. 399–404, 2015. DOI: 10.1097/BRS.0000000000000778. Disponível em: https://www.scopus.com/inward/record.uri?eid=2-s2.0-

84954076781&doi=10.1097%2FBRS.0000000000000778&partnerID=40&md5=c7d93983c2191ad294a4a032d6bc81aa.

OLIVARES-NAVARRETE, Rene; GITTENS, Rolando A.; SCHNEIDER, Jennifer M.; HYZY, Sharon L.; HAITHCOCK, David A.; ULLRICH, Peter F.; SCHWARTZ, Zvi; BOYAN, Barbara D. Osteoblasts exhibit a more differentiated phenotype and increased bone morphogenetic protein production on titanium alloy substrates than on poly-ether-ether-ketone. **Spine Journal**, *[S. l.]*, v. 12, n. 3, p. 265–272, 2012. DOI: 10.1016/j.spinee.2012.02.002. Disponível em: http://dx.doi.org/10.1016/j.spinee.2012.02.002.

OZAWA, Y.; KUBOTA, T.; YAMAMOTO, T.; TSUKUNE, N.; KOSHI, R.; NISHIDA, T.; ASANO, M.; SATO, S. Comparison of the bone augmentation ability of absorbable collagen sponge with that of hydroxyapatite/ collagen composite. **Journal of Oral Science**, Division of Applied Oral Sciences, Nihon University Graduate School of Dentistry, Tokyo, Japan, v. 60, n. 4, p. 514–518, 2018. DOI: 10.2334/josnusd.17-0465.

PADILLA-GAINZA, V.; RODRÍGUEZ-TOBÍAS, H.; MORALES, G.; LEDEZMA-PÉREZ, A.; ALVARADO-CANCHÉ, C.; RODRÍGUEZ, C.; GILKERSON, R.; LOZANO, K. Processing-structure-property relationships of biopolyester/zinc oxide fibrous scaffolds engineered by centrifugal spinning. **Polymers for Advanced Technologies**, Synthesis and Avanced Materials Department, Centro de Investigación en Química Aplicada, Saltillo, Mexico, 2020. DOI: 10.1002/pat.4987.

PENK, Anja et al. The pore size of PLGA bone implants determines the de novo formation of bone tissue in tibial head defects in rats. **Magnetic Resonance in Medicine**, *[S. l.]*, v. 70, n. 4, p. 925–935, 2013. DOI: 10.1002/mrm.24541.

PEREIRA, Tanisha; KENNEDY, John V.; POTGIETER, Johan. A comparison of traditional manufacturing vs additive manufacturing, the best method for the job. *Em*: PROCEDIA MANUFACTURING 2019, **Anais** [...]. : Elsevier B.V., 2019. p. 11–18. DOI: 10.1016/j.promfg.2019.02.003.

QIU, Zhi-Ye; CUI, Yun; WANG, Xiu-Mei. Chapter 1 - Natural Bone Tissue and Its Biomimetic. *Em*: WANG, Xiu-Mei; QIU, Zhi-Ye; CUI, Helen B. T. Mineralized Collagen Bone Graft Substitutes (org.). **Woodhead Publishing Series in Biomaterials**. [s.l.] : Woodhead Publishing, 2019. p. 1–22. DOI: https://doi.org/10.1016/B978-0-08-102717-2.00001-1.

RAMPICHOVÁ, M.; BUZGO, M.; MÍČKOVÁ, A.; VOCETKOVÁ, K.; SOVKOVÁ, V.; LUKÁŠOVÁ, V.; FILOVÁ, E.; RUSTICHELLI, F.; AMLER, E. Platelet-functionalized three-dimensional poly-ε-caprolactone fibrous scaffold prepared using centrifugal spinning for delivery of growth factors. **International Journal of Nanomedicine**, Indoor Environmental Quality, University Center for Energy Efficient Buildings, Czech Technical University in Prague, Buštěhrad, Czech Republic, v. 12, p. 347–361, 2017. DOI: 10.2147/IJN.S120206.

RAN, Qichun; YANG, Weihu; HU, Yan; SHEN, Xinkun; YU, Yonglin; XIANG, Yang; CAI, Kaiyong. Osteogenesis of 3D printed porous Ti6Al4V implants with different pore

sizes. **Journal of the Mechanical Behavior of Biomedical Materials**, *[S. l.]*, v. 84, p. 1–11, 2018. DOI: https://doi.org/10.1016/j.jmbbm.2018.04.010.

RAO, Prashanth J.; PELLETIER, Matthew H.; WALSH, William R.; MOBBS, Ralph J. Spine Interbody Implants: Material Selection and Modification, Functionalization and Bioactivation of Surfaces to Improve Osseointegration. **Orthopaedic Surgery**, *[S. l.]*, v. 6, n. 2, p. 81–89, 2014. DOI: 10.1111/os.12098.

RAWLS, A.; FISHER, R. E. Developmental and functional anatomy of the spine. *Em*: **The Genetics and Development of Scoliosis: Second Edition**. School of Life Sciences, Arizona State University, Tempe, AZ, United States: Springer International Publishing, 2018. p. 1–29. DOI: 10.1007/978-3-319-90149-7_1. Disponível em: https://www.scopus.com/inward/record.uri?eid=2-s2.0-85053733439&doi=10.1007%2F978-3-319-90149-7_1&partnerID=40&md5=e08457aaa4b6c3b41fde0169060d6e5f.

REDDI, A. H. Cell Biology and Biochemistry of Endochondral Bone Development. **Collagen and Related Research**, *[S. l.]*, v. 1, n. 2, p. 209–226, 1981. DOI: 10.1016/S0174-173X(81)80021-0. Acesso em: 5 jun. 2024.

RODRIGUES, I. C. P.; CAMPO, K. N.; ARNS, C. W.; GABRIEL, L. P.; WEBSTER, T. J.; LOPES, É. S. N. From Bulk to Nanoparticles: An Overview of Antiviral Materials, Its Mechanisms, and Applications. **Particle and Particle Systems Characterization**, *[S. l.]*, v. 38, n. 8, 2021. a. DOI: 10.1002/ppsc.202100044.

RODRIGUES, I. C. P.; PEREIRA, K. D.; WOIGT, L. F.; JARDINI, A. L.; LUCHESSI, A. D.; LOPES, É. S. N.; WEBSTER, T. J.; GABRIEL, L. P. A novel technique to produce tubular scaffolds based on collagen and elastin. **Artificial Organs**, *[S. l.]*, v. 45, n. 5, 2021. b. DOI: 10.1111/aor.13857.

RODRIGUES, Isabella Caroline Pereira; TAMBORLIN, Leticia; RODRIGUES, Ana Amélia; JARDINI, André Luiz; LUCHESSI, Augusto Ducati; MACIEL FILHO, Rubens; LOPES, Éder Sócrates Najar; GABRIEL, Laís Pellizzer. Polyurethane fibrous membranes tailored by rotary jet spinning for tissue engineering applications. **Journal of Applied Polymer Science**, *[S. l.]*, v. 137, n. 11, p. 1–10, 2020. a. DOI: 10.1002/app.48455. Disponível em: https://doi.org/10.1002/app.48455.

RODRIGUES, Isabella Caroline Pereira; WOIGT, Luiza Freire; PEREIRA, Karina Danielle; LUCHESSI, Augusto Ducati; LOPES, Éder Sócrates Najar; WEBSTER, Thomas J.; GABRIEL, Laís Pellizzer. Low-cost hybrid scaffolds based on polyurethane and gelatin. **Journal of Materials Research and Technology**, *[S. l.]*, v. 9, n. 4, p. 7777–7785, 2020. b. DOI: 10.1016/j.jmrt.2020.04.049.

ROGALSKI, J. J.; BASTIAANSEN, C. W. M.; PEIJS, T. Rotary jet spinning review - a potential high yield future for polymer nanofibers. **Nanocomposites**, *[S. l.]*, v. 3, n. 4, p. 97–121, 2017. DOI: 10.1080/20550324.2017.1393919.

RUCKH, Timothy T.; OLDINSKI, Rachael A. Antimicrobial effects of nanofiber poly (caprolactone) tissue scaffolds releasing rifampicin. *[S. l.]*, p. 1411–1420, 2012. DOI: 10.1007/s10856-012-4609-3.

RYU, Jeong Hyun et al. Synergistic Effect of Porous Hydroxyapatite Scaffolds Combined with Bioactive Glass/Poly(lactic- co-glycolic acid) Composite Fibers Promotes Osteogenic Activity and Bioactivity. **ACS Omega**, *[S. l.]*, v. 4, n. 1, p. 2302–2310, 2019. DOI: 10.1021/acsomega.8b02898.

SAMELKO, Lauryn; LANDGRAEBER, Stefan; MCALLISTER, Kyron; JACOBS, Joshua; HALLAB, Nadim James. Cobalt Alloy Implant Debris Induces Inflammation and Bone Loss Primarily through Danger Signaling, Not TLR4 Activation: Implications for DAMP-ening Implant Related Inflammation. **PLOS ONE**, *[S. l.]*, v. 11, n. 7, p. e0160141, 2016. DOI: 10.1371/JOURNAL.PONE.0160141. Disponível em: https://journals.plos.org/plosone/article?id=10.1371/journal.pone.0160141. Acesso em: 14 maio. 2023.

SAMUEL, M. P.; MISHRA, A. K.; MISHRA, R. K. Additive Manufacturing of Ti-6Al-4V Aero Engine Parts: Qualification for Reliability. **Journal of Failure Analysis and Prevention**, *[S. l.]*, v. 18, n. 1, p. 136–144, 2018. DOI: 10.1007/s11668-018-0393-9.

SENATOV, F. S.; NIAZA, K. V.; ZADOROZHNYY, M. Yu; MAKSIMKIN, A. V.; KALOSHKIN, S. D.; ESTRIN, Y. Z. Mechanical properties and shape memory effect of 3D-printed PLA-based porous scaffolds. **Journal of the Mechanical Behavior of Biomedical Materials**, *[S. l.]*, v. 57, p. 139–148, 2016. DOI: 10.1016/j.jmbbm.2015.11.036.

SHAHREZAIE, Mostafa; ZAMANIAN, Ali; SAHRANAVARD, Melika; SHAHREZAEE, Mohammad Hossein. A critical review on the 3D bioprinting in large bone defects regeneration. **Bioprinting**, *[S. l.]*, v. 37, p. e00327, 2024. DOI: 10.1016/J.BPRINT.2023.E00327. Acesso em: 13 fev. 2024.

SHAHRIAR, S. M.; MONDAL, Jagannath; HASAN, Mohammad Nazmul; REVURI, Vishnu; LEE, Dong Yun; LEE, Yong-Kyu. Electrospinning nanofibers for therapeutics delivery. **Nanomaterials**, *[S. l.]*, v. 9, n. 4, p. 532, 2019.

SIVASANKAR, M. V.; CHINTA, Madhavi Latha; SREENIVASA RAO, P. Zirconia based composite scaffolds and their application in bone tissue engineering. **International Journal of Biological Macromolecules**, *[S. l.]*, v. 265, p. 130558, 2024. DOI: 10.1016/J.IJBIOMAC.2024.130558. Acesso em: 5 jun. 2024.

SORUSHANOVA, A. et al. The Collagen Suprafamily: From Biosynthesis to Advanced Biomaterial Development. **Advanced Materials**, *[S. l.]*, v. 31, n. 1, p. 39, 2019. DOI: 10.1002/adma.201801651.

STAIGER, Mark P.; PIETAK, Alexis M.; HUADMAI, Jerawala; DIAS, George. Magnesium and its alloys as orthopedic biomaterials: A review. **Biomaterials**, *[S. l.]*, v. 27, n. 9, p. 1728–1734, 2006. DOI: 10.1016/j.biomaterials.2005.10.003.

TAKAHASHI, Hiroyuki et al. Effects of autogenous bone graft on mass and quality of trabecular bone in Ti6Al4V spinal cage fabricated with electron beam melting. **Materials Transactions**, *[S. l.]*, v. 60, n. 1, p. 144–148, 2019. DOI: 10.2320/matertrans.M2018329.

TALHA, Mohd; BEHERA, C. K.; SINHA, O. P. A review on nickel-free nitrogen containing austenitic stainless steels for biomedical applications. **Materials Science and Engineering:**

C, *[S. l.]*, v. 33, n. 7, p. 3563–3575, 2013. DOI: 10.1016/J.MSEC.2013.06.002. Acesso em: 14 maio. 2023.

TANIGUCHI, Naoya; FUJIBAYASHI, Shunsuke; TAKEMOTO, Mitsuru; SASAKI, Kiyoyuki; OTSUKI, Bungo; NAKAMURA, Takashi; MATSUSHITA, Tomiharu; KOKUBO, Tadashi; MATSUDA, Shuichi. Effect of pore size on bone ingrowth into porous titanium implants fabricated by additive manufacturing: An in vivo experiment. **Materials Science and Engineering: C**, *[S. l.]*, v. 59, p. 690–701, 2016. DOI: https://doi.org/10.1016/j.msec.2015.10.069.

THAVORNYUTIKARN, Boonlom; CHANTARAPANICH, Nattapon; CHEN, Qizhi. **Bone tissue engineering scaffolding : computer-aided scaffolding techniques**. [s.l: s.n.]. DOI: 10.1007/s40204-014-0026-7.

VASCONCELLOS, L. M. R. et al. Rotary-jet spun polycaprolactone/nano-hydroxyapatite scaffolds modified by simulated body fluid influenced the flexural mode of the neoformed bone. **Journal of Materials Science: Materials in Medicine**, Department of Bioscience and Oral Diagnosis, Institute of Science and Technology, Sao Paulo State University, Sao Jose dos Campos, Sao Paulo 12245-000, Brazil, v. 31, n. 8, 2020. DOI: 10.1007/s10856-020-06403-8. Disponível em: https://doi.org/10.1007/s10856-020-06403-8.

VO, Tiffany N.; KASPER, F. Kurtis; MIKOS, Antonios G. Strategies for controlled delivery of growth factors and cells for bone regeneration. **Advanced Drug Delivery Reviews**, *[S. l.]*, v. 64, n. 12, p. 1292–1309, 2012. DOI: 10.1016/j.addr.2012.01.016. Disponível em: http://dx.doi.org/10.1016/j.addr.2012.01.016.

WALSH, W. R.; OHNO, M.; GUZELSU, N. Bone composite behaviour: effects of mineral-organic bonding. **Journal of Materials Science: Materials in Medicine**, *[S. l.]*, v. 5, n. 2, p. 72–79, 1994. DOI: 10.1007/BF00121694/METRICS. Disponível em: https://link.springer.com/article/10.1007/BF00121694. Acesso em: 5 jun. 2024.

WANG, W.; YEUNG, K. W. K. Bone grafts and biomaterials substitutes for bone defect repair: A review. **Bioactive Materials**, Department of Orthopaedics and Traumatology, The University of Hong Kong, Pokfulam, Hong Kong, v. 2, n. 4, p. 224–247, 2017. DOI: 10.1016/j.bioactmat.2017.05.007. Disponível em: https://www.scopus.com/inward/record.uri?eid=2-s2.0-85043320451&doi=10.1016%2Fj.bioactmat.2017.05.007&partnerID=40&md5=835296870c696b46fc49c9bbe37b9b03.

WARBURTON, Andrew; GIRDLER, Steven J.; MIKHAIL, Christopher M.; AHN, Amy; CHO, Samuel K. Biomaterials in spinal implants: A review. **Neurospine**, *[S. l.]*, v. 17, n. 1, p. 101–110, 2020. DOI: 10.14245/ns.1938296.148.

WEBSTER, T. J.; PATEL, A. A.; RAHAMAN, M. N.; SONNY BAL, B. Anti-infective and osteointegration properties of silicon nitride, poly(ether ether ketone), and titanium implants. **Acta Biomaterialia**, *[S. l.]*, v. 8, n. 12, p. 4447–4454, 2012. DOI: 10.1016/j.actbio.2012.07.038. Disponível em: http://dx.doi.org/10.1016/j.actbio.2012.07.038.

WU, Su Hua; LI, Yi; ZHANG, Yong Quan; LI, Xiao Kang; YUAN, Chao Fan; HAO, Yu Lin; ZHANG, Zhi Yong; GUO, Zheng. Porous Titanium-6 Aluminum-4 Vanadium Cage Has Better Osseointegration and Less Micromotion Than a Poly-Ether-Ether-Ketone Cage in Sheep Vertebral Fusion. **Artificial Organs**, *[S. l.]*, v. 37, n. 12, 2013. DOI: 10.1111/aor.12153.

WUISMAN, P. I. J. M.; SMIT, T. H. Bioresorbable polymers: Heading for a new generation of spinal cages. **European Spine Journal**, *[S. l.]*, v. 15, n. 2, p. 133–148, 2006. DOI: 10.1007/s00586-005-1003-6.

WYSOCKI, B.; IDASZEK, J.; SZLAZAK, K.; STRZELCZYK, K.; BRYNK, T.; KURZYDŁOWSKI, K. J.; ŚWIESZKOWSKI, W. Post processing and biological evaluation of the titanium scaffolds for bone tissue engineering. **Materials**, Faculty of Materials Science and Engineering, Warsaw University of Technology, 141 Woloska Str., Warsaw, 02-507, Poland, v. 9, n. 3, 2016. DOI: 10.3390/ma9030197.

XU, Haocheng et al. Evaluation of a Porous Bioabsorbable Interbody Mg-Zn Alloy Cage in a Goat Cervical Spine Model. **BioMed Research International**, *[S. l.]*, v. 2018, 2018. DOI: 10.1155/2018/7961509.

YANG, Fei et al. Laser beam melting 3D printing of Ti6Al4V based porous structured dental implants: fabrication, biocompatibility analysis and photoelastic study. **Scientific Reports**, *[S. l.]*, v. 7, n. 1, p. 45360, 2017. DOI: 10.1038/srep45360.

YANG, W.; DONG, Y.; HONG, Y.; GUANG, Q.; CHEN, X. Evaluation of anterior vertebral interbody fusion using osteogenic mesenchymal stem cells transplanted in collagen sponge. **Clinical Spine Surgery**, Department of Orthopaedics, Fifth People's Hospital of Fudan University, Ruili Road No. 128, Shanghai, Minhangqu, 200240, China, v. 29, n. 4, p. E201–E207, 2016. DOI: 10.1097/BSD.0b013e31825ca123. Disponível em: https://www.scopus.com/inward/record.uri?eid=2-s2.0-85007354943&doi=10.1097%2FBSD.0b013e31825ca123&partnerID=40&md5=869db3f519b379f433931a25b8f4ef0e.

ZADEGAN, Shayan Abdollah; ABEDI, Aidin; JAZAYERI, Seyed Behnam; BONAKI, Hirbod Nasiri; VACCARO, Alexander R.; RAHIMI-MOVAGHAR, Vafa. Clinical application of ceramics in anterior cervical discectomy and fusion: A review and update. **Global Spine Journal**, *[S. l.]*, v. 7, n. 4, p. 343–349, 2017. DOI: 10.1177/2192568217699201. Disponível em: https://doi.org/10.1177/2192568217699201.

ZAMANI, Yasaman; MOHAMMADI, Javad; AMOABEDINY, Ghassem; HELDER, Marco N.; ZANDIEH-DOULABI, Behrouz; KLEIN-NULEND, Jenneke. Bioprinting of Alginate-Encapsulated Pre-osteoblasts in PLGA/β-TCP Scaffolds Enhances Cell Retention but Impairs Osteogenic Differentiation Compared to Cell Seeding after 3D-Printing. **Regenerative Engineering and Translational Medicine**, *[S. l.]*, 2020. DOI: 10.1007/s40883-020-00163-1.

ZEUGOLIS, D. I.; KHEW, S. T.; YEW, E. S. Y.; EKAPUTRA, A. K.; TONG, Y. W.; YUNG, L. Y. L.; HUTMACHER, D. W.; SHEPPARD, C.; RAGHUNATH, M. Electro-spinning of pure collagen nano-fibres - Just an expensive way to make gelatin?

Biomaterials, *[S. l.]*, v. 29, n. 15, p. 2293–2305, 2008. DOI: 10.1016/j.biomaterials.2008.02.009.

ZHANG, Fan; XU, Haocheng; WANG, Hongli; GENG, Fang; MA, Xiaosheng; SHAO, Minghao; XU, Shun; LU, Feizhou; JIANG, Jianyuan. Quantitative analysis of near-implant magnesium accumulation for a Si-containing coated AZ31 cage from a goat cervical spine fusion model. **BMC Musculoskeletal Disorders**, *[S. l.]*, v. 19, n. 1, p. 1–8, 2018. a. DOI: 10.1186/s12891-018-2027-5.

ZHANG, Lai Chang; CHEN, Liang Yu. A Review on Biomedical Titanium Alloys: Recent Progress and Prospect. **Advanced Engineering Materials**, *[S. l.]*, v. 21, n. 4, p. 1–29, 2019. DOI: 10.1002/adem.201801215.

ZHANG, X. Y.; FANG, G.; LEEFLANG, S.; ZADPOOR, A. A.; ZHOU, J. Topological design, permeability and mechanical behavior of additively manufactured functionally graded porous metallic biomaterials. **Acta Biomaterialia**, State Key Laboratory of Tribology, Department of Mechanical Engineering, Tsinghua University, Beijing, 100084, China, v. 84, p. 437–452, 2019. DOI: 10.1016/j.actbio.2018.12.013.

ZHANG, Xiaoguang; QIAO, Jiaxin; ZHAO, Hang; HUANG, Zhaohui; LIU, Yangai; FANG, Minghao; WU, Xiaowen; MIN, Xin. Preparation and performance of novel polyvinylpyrrolidone/polyethylene glycol phase change materials composite fibers by centrifugal spinning. **Chemical Physics Letters**, *[S. l.]*, v. 691, p. 314–318, 2018. b. DOI: https://doi.org/10.1016/j.cplett.2017.11.041.

APÊNDICE A

3d printers	166
aluminum alloys	165
angiogenesis	121
antibacterial activity	125
bioactivity	106
biocompatibility	628
biomaterial	279
biomechanics	467
bone	970
bone defect	200
bone density	296
bone development	725
bone graft	147
bone mineralization	156
bone morphogenetic protein 2	141
bone regeneration	439
bone remodeling	317
bone substitutes	128
bone-implant interface	148
calcium	137
calcium phosphate	203
cell adhesion	487
cell culture	475
cell differentiation	490
cell proliferation	573
cell viability	203
clinical article	402
coatings	286
collagen	149
corrosion resistance	103
cortical bone	173
cytotoxicity	104
dental implants	1183
devices	113
diagnostic imaging	276
drug effect	464
durapatite	157
enzyme activity	133
escherichia coli	111
extracellular matrix	117
femur	217
fracture healing	182
gene expression	275
hydrophilicity	194
hydroxyapatite	491
implant	204
in vitro study	454
in vivo study	366
inflammation	104

mandible	233
materials testing	192
maxilla	197
mc3t3-e1 cell line	105
mechanical stress	131
mesenchymal stem cell	237
metabolism	363
metal implants	491
micro-computed tomography	413
morphology	173
morphometry	204
nanotubes	118
osseointegration	3192
ossification	397
osteoblast	498
osteocalcin	183
osteogenesis	623
osteolysis	360
osteoporosis	141
osteotomy	157
pathology	203
periimplantitis	115
phosphatases	141
polyetheretherketone	132
polymer	105
pore size	100
porosity	334
prostheses and implants	330
prosthesis complication	104
protein expression	156
real time polymerase chain reaction	131
scaffolds (biology)	157
staphylococcus aureus	130
stem cells	264
surface modification	102
surface property	895
surface roughness	166
surface treatment	134
surgery	483
survival rate	101
three dimensional printing	188
tibia	191
tissue regeneration	582
titanium	1563
titanium dioxide	294
trabecular bone	192
transcription factor runx2	162
wettability	129
wound healing	158
young modulus	141

APÊNDICE B

Dear Professor Rodrigues,

Thank you for your email.

I understand your concern and can confirm that Theses and dissertations which contain embedded Published Journal Articles as part of the formal submission can be posted publicly by the awarding institution with DOI links back to the formal publications on ScienceDirect(opens in new tab/window)
If you are an author, please share a link to your article rather than the full-text
Millions of researchers have access to the formal publications on ScienceDirect(opens in new tab/window), and those links will help your users to find, access, cite and use the best available version
If you are an author, you may also share your Published Journal Article (PJA) privately with known students or colleagues for their personal use
If you are affiliated with a library that subscribes to ScienceDirect(opens in new tab/window), you have additional private sharing rights for others' research accessed under that agreement — this includes use for classroom teaching and internal training at the institution (including use in course packs and courseware programs), and inclusion of the article for grant funding purposes
Otherwise sharing is by agreement only
The Published Journal Article cannot be shared publicly, for example, on ResearchGate or
Academia.edu(opens in new tab/window), to ensure the sustainability of peer-reviewed research in journal publications
For a more detailed read you may check Journals article sharing | Elsevier policy

Hope this helps, if you have any further questions, please do not hesitate to contact me.

Best regards,
Akshya

Akshya Devi Madhankumar
Journal Manager